A DYNAMIC PHOTOELASTIC INVESTIGATION OF EXPLOSIVE INDUCED FRACTURE

James W. Dally, et al

Maryland University

Prepared for:

Advanced Research Projects Agency
Bureau of Mines

September 1973

UNCLASSIFIED

SECURITY CLASSIFICATION OF THIS PAGE (When Data Entered)

AD-770 545

REPORT DOCUMENTATION PAGE		READ INSTRUCTIONS BEFORE COMPLETING FORM
1. REPORT NUMBER	2. GOVT ACCESSION NO.	3. RECIPIENT'S CATALOG NUMBER
4. TITLE (and Subtitle) A Dynamic Photoelastic Investigation of Explosive Induced Fracture		5. TYPE OF REPORT & PERIOD COVERED Final Report - 8/31/73 6. PERFORMING ORG. REPORT NUMBER
7. AUTHOR(s) James W. Dally William L. Fourney David C. Holloway		8. CONTRACT OR GRANT NUMBER(s) H0220010
9. PERFORMING ORGANIZATION NAME AND ADDRESS University of Maryland College Park, Maryland Mechanical Engineering Department		10. PROGRAM ELEMENT, PROJECT, TASK AREA & WORK UNIT NUMBERS Arpa Order No. 1579, Amend 3, Code Number 2F10
11. CONTROLLING OFFICE NAME AND ADDRESS Advanced Research Projects Agency 1400 Wilson Boulevard Arlington, Virginia 22209		12. REPORT DATE Sept. 1973 13. NUMBER OF PAGES<br~~172~~ 186
14. MONITORING AGENCY NAME & ADDRESS (if different from Controlling Office) U.S. Bureau of Mines Twin Cities Mining Research Center P.O. Box 1660 Twin Cities, Minnesota 55111		15. SECURITY CLASS. (of this report) Unclassified 15a. DECLASSIFICATION/DOWNGRADING SCHEDULE

16. DISTRIBUTION STATEMENT (of this Report)

Distribution of this document is unlimited

17. DISTRIBUTION STATEMENT (of the abstract entered in Block 20, if different from Report)

18. SUPPLEMENTARY NOTES

19. KEY WORDS (Continue on reverse side if necessary and identify by block number)

Mining, Quarrying, Blasting, Stress waves, Model studies, Photoelasticity, Holography, High Speed Photography

20. ABSTRACT (Continue on reverse side if necessary and identify by block number)

Fracture induced by detonating explosive charges was studied by using four different models to examine different aspects of this dynamic process. A photoelastic model of an entire plane with a single explosive charge provided data pertaining to initiation of radial cracks, their propagation and final arrest. Another series of models of half-planes with charges located near the boundary was tested to examine crack re-initiation and propagation due to reflected stress waves. Models of an

DD FORM 1 JAN 73 1473 EDITION OF 1 NOV 68 IS OBSOLETE

UNCLASSIFIED

SECURITY CLASSIFICATION OF THIS PAGE (When Data Entered)

entire plane with two explosive charges were investigated to determine the development of a fracture surface between the two sources. Finally radially expanding dilatational waves were examined photoelastically as they interacted with arrested cracks.

Analysis of the data provided quantitative data on crack initiation times, crack lengths, crack velocities and crack orientations during the dynamic event. Of course the whole field photoelastic records provide a visual display which permits a ready qualitative description of the dynamic process.

Two test series were also conducted with half plane models fabricated from charcoal granite. In the first of these series the dynamic fracture pattern and subsequent fragment motion due to an internal charge located near the boundary was described using results of a high speed framing camera. The second series entailed a feasibility study of stress wave propagation in rock materials using holographic interfermoetry.

Fracture induced by detonating explosive charges was studied utilizying four different photoelastic models to examine different aspects of this dynamic process.

An experimental study was conducted where large plate models were examined in a dynamic polariscope to determine when the cracks were initiated relative to the time of detonation of the explosive. It was observed that the cracks were developed after an initial propagation of a dilatational wave and that the cracks themselves produced a radially outgoing shear wave. As both the dilatational and the distortional wave have much higher velocities than the cracks propagating from the bore holes, the cracks are outdistanced by the stress waves and arrest after a relatively short distance of propagation.

Another series of models of half-planes with charges located near the boundary was tested to examine crack reinitiation and propagation due to reflected stress waves. The P wave from the center of the charge interacts with the boundary of the half-plane producing reflected PP and PS waves. Similarly the S wave interacts with the boundary of the half-plane and generates reflected SP and SS waves. These four reflected waves individually propagate into the fracture zone at four different times in the dynamic event and interact with the existing cracks. This interaction usually results in a reinitiation of an arrested crack and further extension by propagation during the time of passage of each of the reflected waves. The reflecting characteristic of the free boundary of a half-plane provides the means to redirect a significant portion of the energy of the explosive into the fracture zone where it can be effectively employed in extending the cracks to the free boundary and in reducing the

fragment size of the material removed.

Models of an entire plane with two explosive charges were investigated to determine the development of a fracture surface between the two sources. The development of the fracture pattern in the region between the two charges was divided into four phases. The first phase involved the growth of primary radial cracks to a length of about twice the charge radii. The second phase consisted of multiple branching of these primary radial cracks by the P wave originating at the adjacent charge. The longest branches rarely exceeded 1.5 times the radius of the explosive charge. The third phase involves the interaction of the S wave with the arrested branched system and subsequent re-initiation of a few of the large cracks. The final phase occurred after the passage of the S waves and included the time period when the stress state in the region between the two holes decayed to zero. As the stress system decays most of the individual cracks arrest after extensions of less than one radius of the explosive charge.

The final photoelastic models were used to examine expanding dilatational and shear waves as they interacted with arrested cracks. As a crack is acted upon by a propagating P wave, the compressive leading part of the wave was found to have no effect upon the crack. When the wave propagated a little further so that the tensile tail of the wave was over the crack it became active and began to propagate. There is a reorientation of the crack direction such that the maximum principal normal stress acts perpendicular to the crack. The velocity of propagation of the crack drops off as this turning occurs, but picks up again to approach the original crack velocity after the turning is completed. As the S wave passes over the crack it continues to propagate and there is no attempt for the crack to reorient itself with the principal direction.

The total growth during the passage of the P and S waves is small with most of the ultimate crack growth being due to reflected waves from free boundaries.

Two test series were also conducted with half-plane models fabricated from Charcoal granite. In the first of these series the dynamic fracture pattern and subsequent fragment motion due to an internal charge located near a free boundary were observed. A high speed framing camera was utilized to record the event and fragment motions, velocities and accelerations were determined.

The final test series was a feasibility study of stress waves propagation in rock materials using holographic interferometry. The rock sample used did not exhibit flawed or cracked regions and from holographic results appeared to be homogeneous. The fringe patterns obtained for the propagating stress waves were due primarily to the w component of displacement.

The two results from the two series of tests conducted with charcoal granite as the model material showed remarkable similarity to results obtained from similar tests utilizing briefringent polymers as model materials. This permits one to depend upon results obtained photoelastically to predict the behavior of intact homogeneous isentropic rock materials.

Final Report

A Dynamic Photoelastic Investigation of Explosive Induced Fracture

Prepared for

U.S. Department of the Interior
Bureau of Mines
Twin Cities, Minnesota

by

University of Maryland, College Park Campus
Mechanical Engineering Department

Principal Investigator James W. Dally (301) 454-2410
Co-principal Investigator William L. Fourney (301) 454-2411
Co-principal Investigator David C. Holloway (301)454-2411

Sponsored by Advanced Research Project Agency

ARPA Order No. 1579, Amend No. 3
Program Code No. 2F10
Contract No. H0220010

Contract Period Jan. 25, 1972 to Aug. 31, 1973

Total Amount of Contract $30,500

Disclaimer

Table of Contents

List of Illustrations

Abstract

Fracture induced by detonating explosive charges was studied by using four different models to examine different aspects of this dynamic process. A photoelastic model of an entire plane with a single explosive charge provided data pertaining to initiation of radial cracks, their propagation and final arrest. Another series of models of half-planes with charges located near the boundary was tested to examine crack reinitiation and propagation due to reflected stress waves. Models of an entire plane with two explosive charges were investigated to determine the development of a fracture surface between the two sources. Finally radially expanding dilatational waves were examined photoelastically as they interacted with arrested cracks.

Analysis of the data provided quantitative data on crack initiation times, crack lengths, crack velocities and crack orientations during the dynamic event. Of course the whole field photoelastic records provide a visual display which permits a ready qualitative description of the dynamic process.

Two test series were also conducted with half plane models fabricated from charcoal granite. In the first of these series the dynamic fracture pattern and subsequent fragment motion due to an internal charge located near the boundary was described using results of a high speed framing camera. The second series entailed a feasibility study of stress wave propagation in rock materials using holographic interferometry.

1.0 Introduction

In the United States almost all of the metallic ores and rock aggregates are produced in open-pit operations primarily using blasting to remove and fragment the rock. As the size of the mining operation grows the blasting procedures employed become more important. The effectiveness of the blasting has a direct influence on both the economy and the safety of the operation.

Improvement of blasting techniques can result from employment of better drilling tools and equipment, better explosives and better placement and timing of the explosive charges. This particular research study is to provide an understanding of the dynamic processes which are important in selecting an optimum charge pattern and timing sequence. The dynamic processes involve the detonation and subsequent burning of the explosive charge, generation and propagation of the dilatational (P) wave, initiation and growth of the radial cracks at the bore hole, the generation (by the formation of bore hole cracks) of the shear (S) wave and its subsequent propagation, arrest of the radial cracks, reflection of the incident P and S waves producing the PP, PS, SP and SS reflected waves, the interaction of these waves in time sequence with the arrested radial crack pattern and subsequent propagation of these cracks. Dynamic photoelasticity provides an excellent experimental method to study the many different aspects of this problem since whole field fringe patterns representative of the stress wave propagation can be recorded simultaneously with the developing crack patterns.

This report describes the results of four different photoelastic studies on fundamental problems associated with rock removal by blasting

with explosives. Also included are model studies using charcoal granite specimens with either holographic or high speed framing cameras to record the dynamic behavior.

The entire-plane with a single dilatation source (an explosive charge) is described in Chapter 2.0. Of particular importance in this problem was the timing in the initiation of the radial cracks and their propagation until arrest.

The half-plane with a single dilatational source located near the boundary was considered in Chapter 3.0. In this problem, reinitiation of the arrested cracks by reflected PP and PS waves could be examined in detail.

The similarities of the photoelastic results for the half plane model with the failure of a similar model fabricated from charcoal granite is described in Chapter 4.0. In this study a framing camera operating at about 8,000 fps was used to examine the cracks formed and the subsequent development of the "throw" of the fragments.

The problem of the entire-plane with two simultaneously ignited explosive charges is treated in Chapter 5.0. The extension of cracks coming from the left hand source by stress waves generated at the right-hand source is covered in detail. The development of the fracture plane between the two charges is examined.

The reinitiation of stationary cracks by a radially expanding P wave is examined in Chapter 6.0. The orientation of the crack relative to the normal of the stress-wave front is discussed together with the growth rates of the various cracks at different times in the event.

The feasibility of examining wave propagation in dynamic holographic interferometry is treated in Chapter 7.0. Holograms

showing shear and Rayleigh wave propagation are presented.

An overview of the important findings from all these experimental studies is presented under conclusions in Chapter 8.0.

2.0 Fracture Initiation at a Center of Dilatation in an Entire Plane

2.1 Introduction

Perhaps the most fundamental problem associated with the fragmentation process in rock blasting is the initiation of cracks at the bore hole. These cracks are generated by the pressures introduced by a charge detonating in the bore hole; however, the initiation and subsequent propagation of these cracks are independent dynamic processes. An experimental study was conducted where large plate models were examined in a dynamic polariscope to determine when the cracks were initiated relative to the time of detonation of the explosive. It was observed that the cracks were developed after an initial propagation of a dilatational wave and that the cracks themselves produced a radially outgoing shear wave. As both the dilatational and the distortional waves have much higher velocities than the cracks propagating from the bore holes, the cracks are outdistanced by the stress waves and arrest after a relatively short distance of propagation.

2.2 Experimental Procedure

Photoelastic-fracture models representing an entire plane were fabricated from sheets of Homalite 100* either 1/8 or 1/4 inch thick. The sheets were sufficiently large to eliminate the reflected wave from the central region of the model during the crack propagation period. Plate sizes of 12 x 12 and 18 x 18 inches were employed.

Holes were drilled through these Homalite sheets at the center location to contain the explosive charge. These holes ranged in size from 1/4 to 3/4 in. in diameter. The holes were packed with lead azide PbN_6. The amount of lead azide employed varied with the thickness of the sheet and the

*Homalite 100 is a clear polyester type thermosetting polymer available from G-L Industries, Inc., 11-13 Brookside Dr., Wilmington, Delaware.

diameter of the hole. For a 1/4, 1/2 and 3/4 diameter holes in 1/8 in. sheets the charge size was approximately 150, 600 and 1350 milligram respectively. The detonation velocity for the lead azide was about 115,000 in/sec.

The lead azide was detonated with a bridge wire made of one mil constantan wire about 1/8 in. long. The resistance of the wire was in the range of 2 to 3 ohms. The bridge wires were ignited by a 2000 volt firing pulse from a 20 joule source.

Polycarbonate tubes with an O.D. of 1 in. and walls 1/16 in. thick were bonded to each side of the model in an effort to contain the smoke produced by the burning of the lead azide. The shields were generally effective early in the dynamic event so that crack initiation could be observed. However, the shields usually failed prior to crack arrest and it was necessary to repeat the experiment many times in order to examine the crack propagation during the late event.

The stress waves and the cracks produced by the explosive charge were photographed in a light field dynamic polariscope which consisted of two sheets of circular polaroid HNCP-37 commercially available from the Polaroid Corp. A multiple spark gap camera was used to record the dynamic isochromatic fringe patterns and the propagating cracks in the models. This camera was described in detail in a previous report[1] and only a summary description will be presented here. The camera is capable of 16 frames and can be operated at framing rates which can be varied in discrete steps from 30,000 to 800,000 fps. The dynamic resolution of the camera is a function of fringe gradient and fringe velocity. Experiments indicate that gradients of 20 fringes/in with velocities of 75,000 in/sec represent the upper limit of the

(1) Semi-annual Technical Report - "A Dynamic Photoelastic Analysis of Stress Waves from Inclined Line Sources", ARPA Order No. 1579, Amend. No. 3, Program Code 2F10, Contract H0200010, Oct. 15, 1972.

resolution capability.

Because of the difficulties encountered in containing the smoke in the later stages of the dynamic event, it was necessary to conduct a large number of tests to obtain the data on crack initiation, crack propagation and crack arrest. A complete listing of the experiments conducted are shown in Table 2.1. Only tests denoted as H-7, H-11 and H-14 contained data which could be analyzed.

2.3 Experimental Results

The first experimental results which were obtained to provide data for the development of the crack patterns about a center of dilatation in an entire plane are shown in Fig. 2.1. These results correspond to test H-7 with a model 1/8 in. thick containing a 600 milligram charge with a 1/2 in. diameter charge. Five frames have been selected from the sixteen frames to illustrate the essential features of the event.

In the first frame (H-7-1) recorded there is no visible sign of the development of a crack front. The dilatation P wave is expanding radially outward from the source with a velocity of 85,000 in/sec and with a very high amplitude. Indeed, the fringe gradient is so high that the individual fringes cannot be resolved. While cracks have been initiated and the shear wave has been formed they are behind the shield and cannot be observed.

In the fourth frame recorded, (H-7-4) the continued radial expansion of the stress wave in the field is evident. It is also evident that a number of cracks have been initiated and are beginning to propagate. The formation of these cracks produce a shear wave which is just beginning to develop in this frame. While several cracks can be observed in these photographs only cracks labeled D and E were clearly enough defined to be analyzed throughout the event.

Table 2.1

Listing of Experiments Conducted with the Entire Plane

Experiment Number	Model Material	Model Thickness(In.)	Charge Diameter(In.)	Charge Wt(mg)	Recording Period(μsec)
H-1	H-100	1/4	1/4	300	8-30
H-2	CR-39	1/4	1/4	300	8-28
H-3	H-100	1/4	1/4	300	8-28
H-4	H-100	1/8	1/4	150	--
H-5	H-100	1/8	1/4	150	8-30
H-7	H-100	1/8	1/2	600	11-45
H-10	H-100	1/4	3/8	675	92-220
H-11	H-100	1/8	3/4	1350	11-43
H-12	H-100	1/8	3/8	337	56-120
H-13	H-100	1/8	3/4	1350	44-120
H-14	H-100	1/8	3/4	1350	44-111
H-15	H-100	1/8	3/4	1350	--
H-16	H-100	1/8	3/4	1350	--

In the seventh frame, the high velocity dilatational or P wave is beginning to separate. The formation of the shear or S wave is complete and its circular front is clearly evident. There is a marked contrast between the amplitude of the P and S waves and the uniformity of the amplitude. The P wave has an amplitude of at least 7 fringes compared to a maximum amplitude of 3 fringes associated with the S wave. The amplitude of the P wave is essentially a constant independent of angular position in any frame prior to reflection. With the S wave the amplitude depends strongly on angular position. It appears that the amplitude variations in the S wave are dependent upon the initial distortions introduced at the source by the development of the crack pattern.

In the tenth frame, the separation of the P wave from the S wave is nearly complete. There is a low level (corresponding to a fringe order of 0.5 or less) stress field which exists in the tail of the P wave; however, it is extremely small when compared to the amplitude of the original P wave pulse. The separation of the S wave from the crack front is also complete and cracks D and E have arrested. There is again a low level stress field behind the S wave but apparently this stress state does not have sufficient intensity to drive the cracks.

The final fourteenth frame which is shown in Fig. 2.1 indicates the last stage of the dynamic event. Separation of the three processes - - the P wave, the S wave and the crack propagation phase is complete. The cracks have arrested and are obscured by the smoke from the explosive charge. The P wave has begun to interact with the free boundary located about 4 inches from the charge to produce reflected dilatational PP waves and reflected show PS waves. The D & E cracks had propagated outward along nearly radial lines to a distance of 0.83 in. or 3.3 times the radius of the hole containing the charge prior to arrest. A photograph of the crack formation at the

conclusion of the test is presented in Fig. 2.2. These cracks have been re-initiated by the reflecting pulses. For this reason, the positions of the arrested cracks observed in the dynamic test have been marked on the photograph.

The second experiment, with the center of dilatation in the entire plane, which provided data that could be analyzed was test H-11. In this test, a 3/4 in. diameter charge containing 1350 milligram of lead azide was detonated in a 1/8 in. thick plate of Homalite 100. The larger charge produced more extensive cracks which propagated further into the field. Containment of the smoke by the shields was effective and the position of many cracks could be monitored as a function of time.

Four frames of the first seven frames of the event are presented in Fig. 2.3.1. These photographs show the photoelastic fringes corresponding to the P wave propagating radially outward. Next, a crack formation containing a large number of radial cracks is evident. While thirteen different cracks can be observed in frame seven only those cracks labeled A,B,C,D,E and F were monitored throughout the event.

It is unfortunate that some of the light from the lead azide charge persisted after the recording period was complete and produced "ghost" images of the final cracks superimposed on the images of the actual cracks recorded at the framing times. This made the data analysis more difficult but it was possible in most cases to distinguish between the actual image of the crack and the ghost image.

The formation of the S wave can also be observed in Fig. 2.3.1. In this instance, the amplitude of the S wave is relatively large; however, the gradients of both the P and S waves are so high that exact amplitudes cannot be determined. Again the S wave does not exhibit a constant amplitude

with respect to the angular position θ. Instead two nearly diametrically opposed peaks are evident - one near cracks A and B and the other near cracks D, E and F.

The crack propagation period is demonstrated in Fig. 2.3.2 where frames 10, 13 and 16 are reproduced. The continuous radial expansion of the P and S waves is observed with the distance between the two waves increasing with respect to time. In frame 16, the peak fringe order associated with the P wave is about 5.5 and the two S wave peaks correspond to 4.5 fringes.

As both the S and P wave velocities are significantly higher than the crack velocities, the stress waves move away from the crack fronts. The cracks continue to propagate at a constant velocity during the observed period even though the magnitude of the stresses in the region of crack propagation is very small.

During the period of observation the cracks did not arrest even though there was extensive branching and the energy driving the crack front is separated from the shear wave by about 3 pulse widths. The cracks continue to propagate with a constant radial velocity throughout this crack propagation phase.

A photograph of the crack pattern in the H-11 is shown in Fig. 2.4. The very extensive cracking is due primarily to the stress waves reflected from the boundaries of the model. The position of the arrested crack fronts prior to reinitiation by the reflected waves is estimated in this photograph.

The final experiment in the study of the entire plane with a center of dilatation which provided usable data was test H-14. Test H-14 was identical with test H-11 except that the recording time covered a later period - from 44 to 111 μsec. This late event observation permitted a

detailed examination of the arrest phenomena. The six frames which were selected from the sixteen frames recorded during the dynamic event are presented in Figs. 2.5.1, to 2.5.3.

The fringe pattern corresponding to frame H-14-1 in Fig. 2.5.1 shows a large number of cracks. Most of these cracks are still propagating as evidenced by the isochromatic fringe orders showing the position of the active crack tip along the ghost image of the crack. Most of the cracks continue to propagate during the period between frame H-14-1 and H-14-4; however, the intensity of the stresses driving the cracks has dropped sharply as indicated by the isochromatic patterns at the crack tips.

The fringe patterns in Fig. 2.5.2 show that the crack pattern has come to rest with only two exceptions -- cracks D and H continue to propagate. These two cracks continue to propagate throughout the interval from frame H-14-7 to H-14-10 in spite of the fact that the stress field exhibits an extremely low amplitude in the region containing the crack. It is also interesting to note that crack H has turned and is propagating along a line which makes an angle of 65 degrees with a radial line. It is apparent that extremely low stresses, with principal stress directions which differ from those associated with either the P or the S wave, exercise an influence on the final stage of crack propagation prior to arrest.

The final two frames representing the event which are shown in Fig. 2.5.3 are obscured by smoke. Cracks D and H arrest during this period; however, it's evident in frame H-14-16 that crack F will re-initiate within a few microseconds when it becomes engulfed with the reflected PP wave.

2.4 Data Analysis

The data analysis is presented for each of the three models. Although the results obtained for the H-7, H-11 and H-14 models are similar,

individual analysis presents the opportunity to carefully follow the initiation and propagation of the stress waves as a function of position in each model. Since fracture as depicted by crack initiation and crack propagation is not a unique phenomena, data from three models is useful in establishing the general trends of cracks propagating outward from a center of dilatation in an entire plane.

2.4.1 Analysis for Model H-7

The profile of the outgoing dilatational wave is depicted in Fig. 2.6 where the fringe order is shown as a function of radial position. While the fringe pattern inset in this figure is for frame 16, the profile is, nevertheless, typical of the P wave which has propagated away from a center of dilatation. The leading pulse shows a relatively high amplitude (about 4 fringes) which is due to a biaxial state of stress where both the radial and circumferential stresses are compressive. This is followed by a series of peaks which exhibit a much smaller amplitude. The second of three peaks is due to a biaxial state of stress of which both components are tensile.

This outgoing dilatational wave has propagated away from the fracture region near the center of dilatation. In the entire plane, no further fracture is produced and the energy contained in the P wave is dissipated and lost as the wave propagates into the outer regions of the body at a velocity c_p = 85,600 in/sec.

The profile of the outgoing shear wave is shown in Fig. 2.7 for two different angular positions. In both instances, a leading pulse with a fringe order of about 2 is propagating away from the source. This S pulse is propagating with a velocity of 52,300 in/sec. As the S wave has,

at this time (frame H-7, t = 39 μsec), moved into regions well removed from the crack front, the energy associated with the S wave is dissipated as it propagates into the outer regions of the body.

The cracks propagating radially outward from the explosive charge were measured to determine the distance from the center of dilatation to the crack tip. Smoke from the explosive charge and ghost images of the arrested crack pattern on the working prints made this observation difficult. Nevertheless it was possible to observe cracks D and E over a relatively long part of the dynamic event. The radial position of crack D is shown in Fig. 2.8 for the H-7 model. In this instance the crack appears to propagate with a constant component of velocity in the radial direction $\dot{u}_r$ of 13,300 ips. The crack propagates to a position r of 0.82 in. before it arrests. Since the radius of the hole containing the charge was 0.25 in. the ratio of the arrest radius r_a to the charge radius r_c is $r_a/r_c = 3.3$. Of course many cracks were produced by the pressure created by the explosive; however, most of these cracks arrest with values of r_a/r_c less than 2. Only a few cracks are propagated to distances which give values of r_a/r_c which exceed 3.

The front of the P and the S waves are also defined in Fig. 2.8 by showing the radial position of the fronts as a function of time. It is evident from these results that the fronts of the P and S waves are propagating with constant velocities. It is also clear that from Fig. 2.8 that the P and S waves out distance the crack fronts except for a very short interval of time at the beginning of the dynamic event. It is possible to estimate the general features of the initial fracture process by extrapolating the lines identifying the P and S and crack fronts back toward the origin.

An expanded view of the early time region of the dynamic event is illustrated in Fig. 2.9. The event begins with the ignition of the lead azide charge at t = 0. Since the explosive exhibits a detonation velocity of about 115,000 in/sec, the high pressure pulse reaches the boundary of the charge at position r_c = 0.25 in about 2 μsec. When the pressure wave reaches the boundary of the model, the dilatation wave is generated; however, fracture is delayed by about 3.5 μsec. Fracture does not occur immediately since the leading pulse of the P wave is compressive. However, at t = 5.5 μsec, it appears that the second pulse associated with the P wave (see Fig. 2.6) which contains a circumferential tensile stress has propagated into the model. The cracks initiate at this time at many radial locations and as these crack segments join to produce a single crack it appears that the crack has a very high velocity during this initiation phase.

As the cracks are produced, the symmetry of the displacement field is lost and distortions are produced. These distortions produce a shear or S wave which propagates radially outward from the position $r = r_c$. Since the crack tips initially extend into the model beyond the S wave, there is a period of time between 5.5 and 10.5 μsec when the S wave overtakes the expanding crack front. For time t > 10.5 μsec, the shear wave moves away from the radially expanding crack front. However, at least some of the cracks continue to propagate and arrest of the longest crack does not occur until t = 32 μsec. The crack velocity is maintained in this propagation period between t = 10.5 and 32 μsec by very low level transient stress fields associated with oscillations which trail the primary P and S pulses.

2.4.2 Analysis for H-11 Model

The radial positions of the front of the cracks and the fronts of the P and S waves are shown in Fig. 2.10 for the H-11 model. Reference

to Table 2.1 shows that the H-11 model is identical to the H-7 model except for the charge size. For the H-11 model, the charge was increased in size from 1/4 in. radius to 3/8 in. and in weight from about 0.6 grams to 1.35 grams. The results obtained are similiar in that the initiation of the crack front was delayed by 2 to 3 μsec after the P wave began to propagate. During initiation the crack velocity $\dot{u}_r$ is very high. The S wave is initiated at about 5.5 μsec after detonation, and initially the S front is located inside the crack front. Because of the higher velocity of the S wave relative to the crack velocity, the S wave overtakes the crack front at 12.5 μsec. As the S wave propagates away from the crack front, the cracks continue to propagate at a constant velocity. With this H-11 model, the observation time was limited to 48 μsec and the F crack had not arrested. The value of $r_a/r_c > 3.5$, which is consistent with the fact that the charge size and weight was increased.

Considering the experimental difficulties encountered in obtaining the data from the H-7 and H-11 models and the fact that the fracture process is not unique the results obtained from these two models was in excellent agreement.

2.4.3 Analysis of the H-14 Model

The interval of observation for the H-14 model was much later in the dynamic event than was the case with the H-11 model. For this reason, no attempt has been made to analyze the crack initiation mechanism associated with the early time period. However, the results presented in Fig. 2.11 showing the crack front and the fronts of the P and S waves are consistent with the early time findings given in Figs. 2.09 and 2.10.

The important aspect of the results from the H-14 model is the arrest of the crack front. Examination of Fig. 2.11 shows that the largest

crack propagated with a velocity component in the radial direction which appears to be constant until arrest occurred at 76 μsec at a radial position of 1.58 in. The corresponding ratio of the crack length to charge radius $r_a/r_c = 4.2$ is much larger than the value of $r_a/r_c = 3.3$ obtained for the largest crack which arrested in the H-7 model.

It appears that r_a/r_c is dependent upon the weight of the explosive charge W_e. Taking $W_e = 0.6$ grams and 1.35 grams for the H-7 and H-11 models, it is possible to confirm the fact that the value of r_a/r_c is a function of the cube root of W_e as indicated below:

$$r_a/r_c = k \left[W_e\right]^{1/3}$$

where k is 3.8 when W_e is expressed in grams. This constant k is a function of the material and is valid only for Homalite 100.

The crack propagation phase in the H-14 model is initiated at $t = 7$ μsec. The S wave outdistances the crack front at 17 μsec; however, the crack front continues to propagate until $t = 76$ μsec before the crack arrests. At this time the S wave front is about 2.5 inches in advance of the crack front. The energy to drive the crack is extremely low and is derived from the low level oscillations which exist in the tail of the P and S pulses.

2.5 Conclusions

The results from this series of experiments provided the information necessary to characterize the mechanism of fracture about a center of dilatation in an entire plane. When the center of dilatation is produced by an explosive charge, the dynamic event associated with fracture can be divided into seven phases each of which are described below:

(1) Explosive detonation occurs over a time interval ranging from 2 to 3 μsec and produces a high pressure wave which impinges on the walls of the cylindrical cavity containing the charge.

(2) A dilatational or P wave is initiated which propagates radially outward into the entire plane with a velocity of 85 to 92 $\times 10^3$ in/sec. The initiation of fracture is delayed because the primary P pulse is biaxial compression. Fracture appears to initiate after a delay of about 3 μsec.

(3) The apparent crack velocity at initiation is very high because the crack is probably initiated at a number of different sites. These individual cracks grow and coalesce into a single crack within a few μsec and give the effect of a very high crack initiation velocity.

(4) The initiation of cracks destroys the rotational symmetry of the displacement field associated with the P wave and the S wave is generated. This S wave propagates radially outward at a velocity of 50 to 53 $\times 10^3$ in/sec and provides much of the energy necessary to drive the cracks during the period from $6 < t < 12$ μsec.

(5) The S front outdistances the crack front and many cracks arrest since the energy remaining in the area of the crack fronts is small. A few cracks continue to propagate.

(6) This period of propagation for the last crack is relatively long covering the interval from $12 < t < 76$ μsec. The energy required to maintain a constant velocity $\dot{u}_r$ of 12 to 15 $\times 10^3$ in/sec was quite low.

(7) The cracks arrested with the maximum ratios of the arrest radius to charge radius r_a/r_c ranging from 3.3 to 4.2. The maximum value of r_a/r_c was a function of the cube root of the weight of the charge.

3.0 Fracture Propagation by a Center of Dilatation in a Half-Plane

3.1 Introduction

The fracture pattern produced by a dynamic center of dilatation is in the form of a large number of radial cracks. Most of these cracks arrest early in the dynamic event with $r_a/r_c \leq 2$. A few of the cracks do extend further during the propagation phase and reach lengths which exceed 4 times the radius of the charge before they too arrest. Most of the energy of the charge which was transformed into the stress wave is dissipated by the P and S stress waves which propagate into the unbounded media.

In the case of the half-plane, the mechanism of fracture is markedly different from that observed with the entire plane. The P wave from the center of dilatation interacts with the boundary of the half-plane producing reflected PP and PS waves. Similarly the S wave interacts with the boundary of the half-plane and generates reflected SP and SS waves. These four reflected waves individually propagate into the fracture zone at four different times in the dynamic event and interact with the existing cracks. This interaction usually results in a reinitiation of an arrested crack and further extension by propagation during the time of passage of each of the reflected waves.

The reflecting characteristic of the free boundary of a half-plane provides the means to redirect a significant portion of the energy of the explosive into the fracture zone where it can be effectively employed in extending the cracks to the free boundary and in reducing the fragment size of the material removed.

Since this reflection process and its influence on fracture is fundamental to improving the efficiency of the excavation process, a series

of experiments was conducted to closely examine each phase of the process. These experiments are described in the next sub-section.

3.2 Description of Experiments

Models of a half-plane were fabricated from large sheets of Homalite 100 with a thickness t of 1/8 in. or 1/4 in. as illustrated in Fi . 3.1. A hole of diameter, d ,was drilled through the sheet a depth, h, below the free boundary, to contain the explosive charge. The free boundary of the model was finished with a high speed router.

An explosive charge of lead azide was packed into the cavity together with a bridge wire detonator. Tubes of Lexan were cemented to the model about the explosive charge in order to contain both the light and the smoke emitted during the detonation of the explosive charge.

The dimensions of seven different half-plane models which were tested in this series of experiments are presented in Table 3.1. The models were tested by detonating the explosive charge and then recording the propagating stress waves and cracks with a multiple spark gap camera. Since this equipment has been described in Section 2.2 the description will not be repeated here.

3.3 Experimental Results

The general features of stress wave propagation in a half-plane model are illustrated by select results from the H-6 model shown in Figs. 3.2.1 and 3.2.2 In frame 6-1, which is shown in Fig. 3.2.1, the isochromatic fringe pattern associated with the P wave front has expanded radially until it is tangent to the free boundary of the half-plane. The S wave is also propagating radially outward. In frame 6-4, the P wave has interacted with the boundary and has generated the PP and PS waves in the reflection

Table 3.1

Description of Half-Plane Models Charge Characteristics

Model No.	Depth h(in.)	Diameter d(in.)	Weight W_e(grams)	Model Thickness t(in.)
H-6	1.5	1/4	0.15	1/8
H-8	2.0	1/2	0.60	1/8
H-9	2.0	1/2	0.60	1/8
H-19	1.5	3/8	0.675	1/4
H-20	2.0	3/8	0.675	1/4
H-21	2.0	1/2	1.20	1/4
H-22	1.5	1/2	1.20	1/4

All models were fabricated from Homalite 100

process. The incident shear wave is expanding radially and is tangent to the half-plane at the boundary. The reflected PP wave has propagated into the fracture region; however, the shield which serves to contain the light and the smoke from the explosive masks the fracture zone. In frame 6-7, the reflection process with the P wave continues as the PP wave extends below the fracture zone and PS wave is about to interact at the fracture zone. The S wave has begun to interact with the boundary and is generating a SP wave and a SS wave.

Further development of the reflection process is presented in Fig. 3.2.2 where the isochromatic fringe pattern for frames 6-10, 6-13 and 6-16 are illustrated. In all three of these frames, the PP wave is well below the fracture region about the explosive charge and is no longer contributing to the fracture process. The PS wave is sweeping through the fracture zone in frame 6-10 and propagates below the fracture zone by the time t = 72 μsec when frame 6-13 was recorded.

The SP wave is a dilatation wave generated when the S wave reflects from the free boundary. Since it propagates with the P wave velocity c_p = 89,000 in/sec it overtakes the slower PS wave which is propagating with S wave velocity, c_s = 48,000 in/sec. The SP wave has caught-up with the PS wave in frame 6-13 and actually preceeds the PS wave in frame 6-16.

The SS wave is the last of the four reflected waves which propagates from the boundary to the fracture zone. It passes through the fracture zone by frame 6-13 and is below the zone in frame 6-16.

It is also important to note the complex fringe pattern which remains in the region between the explosive charge and the free boundary after the passage of the final reflected wave (SS). These fringes are of relatively low value (usually 0.5 or 1.5 order) and are due to the reflections of the

much smaller magnitude pulses which exist in the tail following both the P and S waves. These lower level stresses are important in the propagation of the cracks which extend from the explosive charge to the free boundary for two reasons. First, they occur for a relatively long period of time and second, the cracks do not require high stress levels to maintain their velocity once they have been initiated.

The development of a fracture pattern by the stress waves reflected from the boundary of a half-plane was demonstrated with model H-9. The four frame sequence presented in Fig. 3.3.1 depicts the general characteristics of the stress wave crack interaction as observed in a dynamic polariscope. In frame 9-1, cracks labeled A through F can be observed in the region of the explosive charge. These cracks were developed at the boundary of the explosive charge by the incident P and S waves in the manner described in Sections 2.4 and 2.5. At the time frame 9-1 was recorded all of the cracks, with the possible exception of crack E, had arrested and were stationary.

The first reflected stress wave to interact in the fracture zone is the PP wave. This wave reinitiates, first, the E crack in frame 9-2 as evidenced by the characteristic isochromatic fringe pattern which has formed at the crack tip. The B and F cracks are reinitiated by the PP wave in frame 9-3. Smoke obscures observation of crack A, C and F even in the very early frames.

The second reflected wave (the PS wave) reaches the fracture zone interacting with crack E in both frame 9-3 and 9-4. Reference to Fig. 3.3.2 indicates that the PS wave propagates through the fracture zone in frames 9-5 and 9-6 and interacts with cracks B and F during this period.

After passage of the PS wave both B and E cracks arrest. The arrest of crack B is final as it remains stationary throughout the remainder of the dynamic event.

The reflected SP and SS waves are not evident from the photoelastic fringe pattern because the amplitude of the incident S wave was too small. However, in the period between frame 7 and 10, the E crack was reinitiated for a brief period by the SP wave. Following frame 10 the E crack becomes stationary. The breakout of the section between the charge hole and the free boundary of the half-plane was not completed during the dynamic event because all of the cracks arrested short of reaching the boundary.

One other interesting characteristic of the fracture pattern was observed during the H-9 experiment. A spall type fracture was observed in the form of a crack approximately 1/2 in. long and 1/2 in. below and parallel to the free boundary. This crack was evident in frame 1 and was probably due to the tensile stress field produced by the super position of the reflected PP wave with the tail of the incident P wave. The spall type crack was stable during the passage of the other reflected waves PS, SP and SS.

The third half-plane experiment described here involves model H-21 and illustrates some of the characteristics of fracture when both spall and breakout occurs. The dynamic isochromatic fringe patterns and the crack array representing the early portion of the event is presented in Fig. 3.4.1. In frame 21-1, the P wave has propagated to the boundary and has reflected generating the PP and PS waves. An internal fracture in the form of a double spall has been developed. Unfortunately the ghost image recorded with the real image of the crack makes the pattern difficult to distinguish. For this reason, the location of the crack is shown with white ink lines. It is evident that the two spall type cracks are connected with a perpendicular crack to form a pattern which resembles an I.

In frame 21-2, fracture is occurring in three different regions. Cracks oriented in the vertical directions are growing from the four end points on the I spall pattern. Next, a large horizontal crack has been produced along the scribe line above the charge by the reflected PP wave. Finally, the cracks which were initiated at the boundary of the explosive charge have propagated into the region outside the smoke shield. Cracks labeled A through E can be observed interacting with either the reflected PP wave or the incident shear wave.

In frame 21-3, crack propagation has continued. A crack normal to the free boundary connects with the double spall and propagates in the direction of the explosive charge. This crack is driven by the reflected SS wave. The PP wave has propagated into a region below the fracture zone and is no longer a factor in the fracture process. The PS and SP waves are interacting with most of the cracks on the top side of the explosive charge.

In frame 21-4, the vertical crack continues to propagate from the boundary to the explosive charge. This crack is behind the SS wave which is the last of the reflected waves; however, the stress level associated with secondary reflections from the tail of the incident P and S waves is sufficient to maintain the velocity of this crack. The PS wave has propagated through the upper portion of the fracture zone.

Five additional frames which depict the final phase of the fracture process are presented in Fig. 3.4.2. Frame 21-5 shows the PS wave propagating into the region below the fracture zone. The SS wave is still in the fracture area and is influencing the propagation of the cracks in the area above the explosive charge. Branching and sharp turns are evident with most of the extended cracks. It is also interesting to note that much

of the energy associated with the PS wave has propagated laterally out of the field and while it remains near the bench face it will be dissipated unless it interacts with the fracture zone of an adjacent charge.

Crack propagation continues in frame 21-6 in spite of the fact that all of the primary reflected waves have propagated into regions below or to the sides of the fracture zone. The stress level in the area of crack propagation remains relatively high (fringe orders of 4 or 5 are common) due to the combined stresses of the incident and reflected waves resulting from the tail of the P and S waves.

The fringe patterns presented in frames 21-8 and 21-10 show the decay of the stress field in the region between the free boundary and the explosive charge. Many of the cracks arrest during this decay period, but others remain active and continue their propagation. For instance in frame 21-8, the vertical crack has junctioned with the spall formed on the scribe line to provide a breakout (a continuous crack from the explosive to the free boundary). Crack B continues to propagate even in frame 21-10 when the stress level is very low.

Final arrest of all the cracks was recorded in frame 21-12. The stresses in the area of interest are extremely low and crack velocities have gone to zero. A PS wave reflected from one of the side boundaries of the model has entered the field of view. This wave should be disregarded since it was due to finite model size.

3.4 Data Analysis

The general features of stress wave induced fracture from a center of dilatation in a half-plane have been illustrated in the previous section. The fracture process is extremely complicated. It consists of a minimum of twelve phases as listed in chronological order below:

1. Crack initiation at the center of dilatation
2. Radial crack propagation away from the center of dilatation
3. Crack arrest as stress waves outrun the crack front
4. Reflection of the P wave from the free boundary
5. Single or multiple spall produced by the reflecting PP wave
6. Crack propagation normal to spall plane in both directions
7. Reinitiation of radial cracks on the top side of the explosive charge by the reflected PP wave
8. Maintainence of crack propagation by the subsequent passage of the PS wave
9. Reflection of the S wave from the free boundary
10. Maintainence of crack propagation by secondary reflections of pulses in the tail of the incident P and S waves
11. Breakout when cracks extend from the explosive charge to the free boundary
12. Final crack arrest.

The first three phases have been covered in detail in Section 2 and no further analysis will be presented here. Each of the other phases will be considered individually in subsequent paragraphs.

The reflection of the dilatational wave from the free boundary is well understood. The incident P wave interacts with the free boundary to produce a reflected dilatational wave (PP) and a reflected shear wave (PS) as illustrated in Fig. 3.5.1. The relation between the reflection angle β for the PS wave and the angle of incidence α for the P wave is given

by

$$\text{Sin } \alpha/\text{Sin } \beta = c_p/c_s$$

where c_p and c_s are the wave velocities for the dilatational and shear waves respectively. Typical values c_p and c_s are 89,000 and 48,000 in/sec respectively; thus, Sin α/Sin β = 1.85. Typical fronts associated with the PP and PS waves are presented in Fig. 3.6 and show the relative position of four waves at an early time in the reflection process.

A spall type fracture can be produced by the reflected PP wave provided the material is sufficiently brittle. A spall type fracture illustrated in Fig. 3.7 is produced by the dynamic state of tensile stress associated with the reflected PP wave.

The development of the tensile pulse by the reflection process is illustrated in Fig. 3.8. The leading pulse in the incident wave is compressive and as such it propagates through the model material without producing failure. It is followed by a small tensile pulse which is not of sufficient magnitude to produce failure. As the incident P wave interacts with the free boundary, the reflected PP wave propagates back into the model with its sign reversed. This PP wave is superimposed on the tension tail in the incident P wave to produce a very large tensile peak about 0.2 inches from the free boundary. This distance corresponds closely with the location of the spalls shown in Figs. 3.9, 3.10 and 3.11 for models H-19, H-21 and H-22.

In addition to the spall adjacent to the boundary all three of the fractures shown in Fig. 3.9 to 3.11 exhibit other spalls located between the first spall and the explosive charge. Multiple spalling occurs whenever the maximum stress due to the incident and reflected waves is more than twice the normal stress required to produce a tensile failure

in the material or when the material contains flaws which tend to reduce the fracture stress.

Spalls also occurred on some of the scribe lines drawn on the model. These scribe lines served as stress raisers and acted to induce spalling type of fracture. In future work care will be exercised to place the scribe lines in regions removed from the fracture zone.

In these experiments, the horizontal propagation of the cracks forming the spall planes was limited. Reference to Fig. 3.4.2 and Fig. 3.10 shows that the first spall was 1/8 in. long and the second 9/16 in. long. Instead of continuing to propagate horizontally, the spall cracks branch and then often turn to propagate normal to the free boundary. These cracks shown schematically in Fig. 3.12 run from the spall to the boundary and also from the spall in toward the explosive charge. This set of vertical cracks is important since it provides a mechanism for breakout. The system of vertical cracks connect with spalls or radial cracks originating at the explosive charge to provide a breakage path between the charge and the free boundary. It appears that this breakage path forms before any of the radial cracks which initiate at the explosive charge can reach the free boundary.

The PP wave also plays an important role in the reinitiation of the arrested cracks in the immediate vicinity of the explosive charge. The interaction of the stress waves with these arrested cracks is clearly demonstrated in frame 9-2 of Fig. 3.3.1. A line drawing showing a typical crack at the instant of reinitiation is presented in Fig. 3.13 and shows the relative positions of the four waves. While exact data on crack growth and crack velocities can not be established, because of the difficulties in establishing the location of the crack tips in the photographs, estimates are possible. The main pulse in the PP wave is relatively short about 0.6 in.,

and the wave is propagating at 89,000 in/sec. Thus, the PP wave exerts its influence on a typical crack for about 6.7 μsec. The growth of the crack during this period is approximately 0.1 in. assuming a crack velocity of 15,000 in/sec. In dimensionless form, the ratio of the radial crack length to the charge radius increases by about 0.5 (from about 4 to 4.5) due to the PP wave.

Inspection of Fig. 3.13 shows that the PS wave closely follows the PP wave and within a few μsec after the passage of the PP wave the crack is under the influence of the PS wave. This development of the wave fronts relati to the position of a typical crack is shown in Fig. 3.14. Reference to frame 0-3 of Fig. 3.3.2 shows the envelopment of the crack by the PS wave. Again the resolution of the crack tip was not adequate to provide precise data regarding crack growth due to the action of the PS wave but it is evident that the growth was small. The main pulse in the PS wave is only 0.3 in. long and since it travels with a velocity of 48,000 in/sec it interacts with the crack for only 6.3 μsec. As the directions of the principal stresses in the PS wave differ appreciably from the directions of the stresses in the PP wave the effect is to turn the crack as shown in Fig. 3.14. Again the growth of the crack will be limited to less than 0.1 inch due to the short interaction time and the relatively low crack velocity.

Fracture at the boundary of the circular cavity destroys the symmetry of the displacement field and the resulting dynamic distortion produces a shear wave. This shear wave is of relatively low magnitude in comparison with the incident P wave, nevertheless it can be distinguished in frame 6-7 of Fig. 3.2.1 and frame 9-2 of Fig. 3.3.1. When a plane incident S wave interacts with a free boundary, it produces reflected shear SS and dilatational SP waves as illustrated in Fig. 3.5.2. The relation

between the reflected angle β for the SP wave and the angle of incidence α for the S wave is given by:

$$\text{Sin } \alpha / \text{Sin } \beta = c_s / c_p$$

The positions of the wave fronts associated with the SS and SP waves are shown in Fig. 3.14 with respect to the positions of the other four waves. An example of the reflected SS wave is presented in Fig. 3.15. Unfortunately the stress difference associated with the SP wave is not sufficiently large to produce a photoelastic response.

The individual effect of the SS and SP waves on the propagation of the cracks can not be established. These waves are superimposed on the reflections of the secondary pulses which exist in the tail of the incident P wave. The net result is the complex fringe pattern best depicted in frame 21-5 presented in Fig. 3.16. This dynamic state of stress is important in the development of the crack pattern because it is sustained at a high enough stress level to maintain crack propagation for an extremely long period of time. Inspection of Fig. 3.4.2 indicates that the crack marked by the symbol A grows progressively over an 83 μsec period. The radial component of the crack extention during this period was 0.6 in. which is much more significant than the growth of about 0.1 in. recorded during the passage of the higher amplitude PP and PS waves. Average crack velocity achieved during this period was about 7000 in/sec.

In spite of the extended growth of the crack labeled A in the post reflection period this crack did not extend to the boundary. Breakout is defined here as the extension of a crack between the explosive charge and the free boundary. Breakout occurred in the H-21 model by the juncture of a radial crack from the explosive with a horizontal spall crack and finally

the connection of an in-running crack with the spall fracture. This involved crack development was completed in frame 21- 7 and is shown in Fig. 3.17. Inspection of the final fracture patterns in Fig. 3.9 for model H-19 and Fig. 3.11 for model H-21 show that a similar type of breakout occurred.

The final phase of the event is crack arrest which occurs after the decay of the stress field in the post reflection period. An excellent example of crack arrest is presented in frame 21-12 of Fig. 3.4.2 where cracks labeled A and B have stopped before intersecting the boundary. It is important to note that the time of crack arrest in this instance was about 200 μsec after the initiation of the explosive charge. This very short time is indicative of the dynamic nature of the fracture process associated with bench blasting.

3.5 Conclusions

Fracture propagation by a center of dilatation in a half-plane is enhanced due to the reflection process which takes place at the free boundary of a half-plane. The reflection process is important since it redirects the stress waves generated by the explosive charge back into the fracture zone and because it converts compressive states of stress into tensile stresses which are capable of producing fracture in brittle materials.

A detailed examination showed that spalling was produced by the reflected PP wave and that cracks were initiated at these spalls which tended to bridge the gap between the explosive charge and the free boundary.

The reflected PP and PS waves restarted the arrested radial cracks which had been initiated by the explosive charge; however, the period of interaction of these reflected waves with the crack pattern was so short that crack growth was quite small.

While radial crack growth due to a sustained dynamic state of stress in the post reflect period was significant, breakout occurred due to the intersection of radial cracks, spalls, and spall induced cracks near the center line of the models.

Event times were extremely short. The time to arrest cracks originating from the explosive charge was about 40 μsec; the time to breakout was about 130 μsec and the time to final crack arrest was usually less than 200 μsec. While these short times are related to the model size, they nevertheless indicate that the fracture process is totally dynamic and related directly to stress wave propagation and the interaction of the stress waves with the crack tips.

4.0 Rock Fracture in Close Proximity to a Free Boundary

4.1 Introduction

In brittle materials such as rock, glass and some plastics the compressive strength is much greater than the tensile strenyth. When an explosive charge is set off in the interior of a body a compressive stress wave propagates outward until it reaches a free surface. Upon reaching a free surface the wave is reflected back with a change in sign from compression to tensile. (As explained in earlier sections other types of waves are also generated upon reflection.) If the energy released during the explosion is sufficient the stress level in the wave will be high enough that upon changing to tensile in sign the ultimate strength of the material will be exceeded and a fracture parallel to the boundary will be produced.

In previous tests utilizing CR-39 and Homalite 100 (birefringent polymers as model materials , we have observed on occasion spall type fractures. Most of these however, were found to occur where a scribe mark had produced stress concentrations which initiated the fracture.

We were interested in observing the possibility of producing a spall in unmarked specimens and chose to investigate the behavior of actual rock samples when an explosive was set off in the vicinity of a free boundary. The decision to use rock as the model material was based upon two factors. The first was that the ratio of tensile ultimate to compressive ultimate as well as the tensile strength of rock is much smaller than in the plastics previously used and this should make the production of spall type fracture easier to obtain. Secondly, it was felt that the crack pattern obtained in this task could be compared to the crack pattern in the preceding task on half-plane behavior of plastic materials.

This would indicate if the results obtained in plastics are indicative of the response one could expect to see from a rock material.

High speed photography was used to record the fracture of the rock due to the detonation of lead azide. 208 frames were obtained which covered a time span of 25.5 milliseconds.

4.2 Experimental Procedure

The rock used in the experiment was a 12 in x 12 in x 1 1/4" thick slab of charcoal granite provided by the Bureau of Mines. A 3/8" diameter hole 7/8" deep was drilled with a masonry bit into the back of the rock, 1 1/2" from the top boundary 6 inches in from either side. The hole was not drilled completely through the rock in an effort to prevent the smoke from the burning lead azide from obscuring the fragment motion. The hole was lightly packed with dry lead azide and a bridge wire similar to those described in previous sections was placed in the $Pb(N_3)_2$ filled hole.

A Beckman & Whitley model 350 high speed camera capable of taking up to 35,000 frames per second was utilized to record the event. For the experiment the speed was 8150 frames per second and a shutter speed of 1/50 of a second was used. Fig. 4.1 shows a close up of the camera.

The rock sample was placed in a fiberglass lined plywood box that was nominally 3 ft deep by 2 ft high by 2 ft wide to contain the rock fragments. There was a 13" by 13" hole in the front to permit viewing by the camera. Nine, type FF-26 Sylvania flashbulbs, were equally spaced around the hole in the front panel to illuminate the event. These bulbs produce 20,500 lumen seconds each and have a broad plateau wnich lasts for approximately 25 milliseconds, with a rise time of 11 milliseconds. Fig. 4.2 shows a view of the rock specimen in the protective box.

The timing of the various events was accomplished by using a combination of a falling weight and an oscilliscope. The schematic diagram of the events and the equipment used in the experiment is shown in Fig. 4.3. A falling weight closed a switch which initiated flashbulb burn. The flashbulbs took approximately 11 milliseconds to produce maximum output. 3.8 milliseconds later the same weight upon falling further closed a second switch which operated a solenoid activated camera shutter and at the same instant triggered an oscilliscope. The camera shutter took 9.8 milliseconds to open after the switch was closed. 9 milliseconds after the scope was triggered a pulse was sent from the oscilliscope to a 15 KV 10 joule detonator which was used to ignite the explosive. The light output from the flashbulbs was monitored by a model 560B EG & G lite-mike and was displayed on the oscilliscope screen. The flashbulb circuit was powered by two 22.5 volt batteries wired in a parallel circuit. The camera shutter was powered by a 120 D.C. Trygron Model HR60-5B power supply. Fig. 4.4 shows the physical arrangement of the equipment used to conduct the experiment.

4.3 Results

The data taken consists of 208 frames covering a time span of 25.5 milliseconds. The event can logically be broken up into the following segments:

1. The initiation and growth of radial cracks from the passage of the P and S waves as they propagate from the borehole immediately following the explosion.
2. The arrest of these cracks as the P and S waves outrun them.
3. The reinitiation and turning of the radial cracks and their propagation to the boundary by the reflected waves from free surfaces.

4. At the same time as the radial crack initiation and growth is occurring the initiation and growth in a similar fashion of cracks from the bottom of the borehole to the front surface of the rock sample is occurring.

5. The widening of the cracks cause the unkeying of the smaller rock fragments on the front face of the sample at the bottom of the borehole. That is the cratering of the area immediately below the borehole in the undrilled area.

6. The movement of the various smaller rock fragments from the cratered region as rigid bodies.

7. The widening of the radial cracks to unkey the various larger rock fragments.

8. Finally, the motion of these larger rock fragments as rigid bodies

Table 4.1 gives the chronological history of the events that occurred with an indication of the times involved between events. Recall that 208 frames were recorded during the lapsed time of 25.5 milliseconds at a speed of 8150 frames per second. This results in the time between frames as 123 μseconds or .123 milliseconds. The first two frames were under-exposed which was probably due to the flashbulbs taking longer than 11 milliseconds to come up to full light output. This was indicated in the time recorded on the oscilliscope screen. That is to say that the light intensity was still increasing at the time of shutter opening.

The growth and propagation of cracks (both radially and in the cratered region) as indicated in earlier sections of this report occur very quickly - on the order of a few hundred microseconds. The first frame occurs at least 800 μseconds after detonation and these events

Table 4.1

Time (Milliseconds)	Event
-12.8	Flashbulbs activated
-9.0	Scope triggered and switch to open camera shutter closed
-1.8	Flashbulbs have reached plateau in output
0	Detonation of $pb(N_3)_2$
+0.8	Shutter opened
+23.2	End of plateau in flashbulb output reached and intensity begins to fall off
+26.3	Camera shutter closed after 208 frames

were therefore already over before the first frame was recorded. This is evident from looking at Fig. 4.5 which shows frames number 3 and 6 which occur 1.046 and 1.415 milliseconds after detonation. Frame 3 although still slightly underexposed shows a radial crack extending to the free boundary and smoke beginning to be emitted through the cratered area cracks. This is more evident in frame 6 since the exposure is much better as the flashbulbs are by this time apparently operating at peak output. The cratering is a three dimensional effect and occurred due to terminating the drill hole in an effort to prevent the smoke from the explosive from obscuring the rock fragments.

The unkeying of the larger rock fragments formed by the radial crack is illustrated in Fig. 4.6 which depict the cracks beginning to widen. There is still contact between fragments at this time (1.661 and 1.907 milliseconds after detonation). Irregularities of the fracture surfaces result in interfragment forces which restrain free rigid body motion of the individual particles.

Fig. 4.7 shows selected later frames in which the fragments are unkeyed and moving as rigid bodies fairly much independent of one another. The times associated with each frame are indicated in the figure.

Fig. 4.8 shows the reconstructed rock after the explosion. It should be noted that the lower left hand corner was chipped before the test as a result of shipping and is not a result of the detonation. Certain fragments are labeled in 4.7 and 4.8 identification purposes in the next section.

4.4 Data Analysis

The fragments in the cratered region were very much smaller than those produced by the radial cracks which were propagated to the free surface. The size of those larger fragments as seen from figure 4.8 ranges from the smallest (labeled fragment D) weighing 108 gms to the largest (labeled fragment C) weighing 669 gms. These larger fragments were given both a rotational and translational velocity by the explosive. The crater region particles on the other hand were small-ranging from dust fragments to flake like particles less than 1/3 of an inch in diameter. The two crater region particles marked A and B in Fig. 4.7 were identified and their motion tracked in the majority of the frames.

Keep in mind that in reality the particles A and B are moving towards the camera lens as well as in the radial direction. Fig. 4.9 is a plot of radial displacement versus time for particle A while Fig. 4.10 presents the same information for particle B. Both of these particles were small enough that their rotational aspect can be ignored. The slope of the straight lines passing through the data points in Fig. 4.9 and 4.10 yield values for the radial components of the velocities of particles A and B. The values are $v_{Arad} = 30.2$ ips and the $v_{Brad} = 150.8$ ips. Unfortunately neither particle A nor B could be identified after the test was complete in order to obtain a value for the masses of the particles. Hence, since the mass and the component of velocities in the direction of the camera is unknown, no information on the kinetic energy of these particles will be attempted.

The large fragment labeled C in Fig. 4.8 has its lower right hand corner in contact with the parent piece of rock in every frame. This piece can be assumed to be undergoing rigid body rotation about this contact point

in the original plane of the sample. Fig. 4.11 gives the y component (see Fig. 4.8 for coordinate system) of displacement versus time for point C_1. Point C_1 is the point labeled 1 on fragment C and its position is indicated in Fig. 4.8. This data can be approximated fairly well with the straight line shown on the figure.

If the motion is rotational, then the speed of any point (such as C_1) can be found from

$$v = r\omega \tag{4.1}$$

where

v - speed of particle

r - straight line distance of point from rotation center

ω - angular speed of rotation of fragment.

The slope of the line in Fig. 4.11 gives the y component of the velocity of the point

$$\frac{dy}{dt} = v_y = v \cos\theta \tag{4.2}$$

where v_y is the component of velocity in the y direction and θ is the angular orientation of the position vector from the point of rotation to the point at any instant of time.

$$v \cos\theta = v_y = r\omega \cos\theta \tag{4.3}$$

or $$\omega = v_y / r \cos\theta$$

This equation results from multiplying Eqn (4.1) by Cos θ.

The angular velocity of the fragment can therefore be obtained by dividing the y component of velocity by r Cos θ.

From Fig. 4.11 the y component of velocity for point C_1 is a constant and is equal to 33.1 ips.

Fig. 4.12 is the angular velocity of fragment C versus time and can once again be approximated by the straight line shown. The slope of this line is the angular acceleration of the rotating rock fragment.

This number from Fig. 4.12 is found to be 404 rad/sec^2. Fragment C had a weight of 668.97 grams. As can be observed from Fig. 4.12, the angular velocity of the fragment ranged from 11 rad/sec to 19 radians per second during the lapsed time of the test.

The final fragment that was identified and tracked during the test is labeled as fragment D in Fig. 4.8. It is located directly above and to the right of the borehole and upon becoming unkeyed from the rest of the sample undergoes a combination of rotation and translation. This motion once again is assumed to take place in the plane of the original rock sample. The trajectories of the two points D_1 and D_2 as identified in Fig. 4.8 were obtained from the pictures taken during the experiment. These two points were 1 inch apart and moved as shown in Fig. 4.13.

The first point plotted corresponds to frame 10 and the last to frame 200 and therefore shows the position of the fragment from 2.02 milliseconds after detonation to 25.2 milliseconds. The smoothed trajectory curves shown in Fig. 4.13 were used to determine angular velocity for the fragment utilizing the instantaneous center method. The speed of point D_1 in frame 10(.923 milliseconds after detonation) was found to be 118 ips. Point D_2 was found to be moving with a speed of 102. ips at the same instant yielding a rotational velocity of approximately 50 rad/sec.

In frame 200 (25.4 milliseconds after detonation) the speed of D_1 was 122. ips that of D_2 was 87 ips and the angular velocity of the

fragment was found to be about 7 rad/sec. The calculations involved in determining the angular velocity for the fragment were graphical and time consuming. For that reason no attempt was made to determine intermediate values of angular velocity. The fragment weighed 107.76 grms.

4.5 Conclusions

The conclusions to be drawn in addition to the information that was presented in the last section are three.

First, there was no indication of the production of a spall type fracture other than possibly some of the flake-like particles found at the bottom of the borehole. These were results of a three-dimensional nature and whether any of these were spalls or no cannot be inferred here. This was in spite of the fact that one would expect it would be easier to produce spall in rock than in other materials used earlier. This was only one test with a fixed distance between the charge and the free surface. It is very likely that varying this distance as well as the charge volume would result in combinations that would produce spalling. This would be in accord with experience from prior tests utilizying birefringent polymers where only certain spacings of the charge with respect to the free boundary were advantageous and even then spalls were not produced in every test.

Secondly, the crack pattern produced in the rock sample was very similar to the patterns that have been obtained in earlier research with plastics as the model material. The similiarity of the final rock patterns in rock and plastics tends to lend credulence to predicting the response of rock materials to explosive loadings from results obtained from photoelastic polymers.

Finally, as was found earlier, the events of interest - namely crack initiation, growth, arrest, and reinitiation - are very short in duration. In order to capture these events on film requires the use of a much faster framing camera than used here. It is felt that sufficient resolution was present in the system to see these occur if the filming speed had been on the order of 10 times as fast.

5.0 Fracture Produced by Two Dilatational Sources in an Entire Plane

5.1 Introduction

The entire plane with two explosive charges to serve as dilatation sources a distance s apart represents a third fundamental problem associated with dynamic fracture. The problem may be examined with the charges detonated simultaneously or in a time controlled sequence with variable delay between the firing of the first and second charges. In this investigation, only the simultaneous firing of the two charges is considered.

This problem is important since a line of boreholes are often drilled, loaded and fired to pre-split a specific shape associated with a tunnel opening or a cut through a rock formation for a road or canal. The process involves explosively induced P and S waves identical to those described in Chapter 2 for a single dilatational source in an entire plane. Initially, the propagation of the radial outgoing crack is the same; however, after a time $t < s/c_p$ the P wave from say the right hand source interacts with the cracks propagating radially outward from the left hand source. As the cracks are extended and the S waves interact with the fracture surfaces a small amount of energy remains trapped in the region between the explosive charges. This energy is important since low level stresses are capable of maintaining crack extensions for considerable distances.

Another factor to be considered in this problem is the interaction of the waves from the two sources along the center-line of the model. It may be possible that the superimposed stress waves produce internal fractures which promote the rupture of the material between the two sources.

A preliminary investigation of this problem was conducted by testing three different two source models. While the data obtained was not extensive enough to be statistically extensive, the primary characteristics of the fracture process were established. The experiments, procedure, results, data analysis and conclusions are covered in detail in subsequent subsections.

5.2 Experimental Procedure

Several models of an entire plane with two explosive charges in close proximity were tested. The geometric parameters associated with these models are illustrated in Fig. 5.1 and include s the distance between the charges, d the diameter of the charges, w the weight of the lead azide used in each charge and model thickness h. All models were fabricated from Homalite 100 sheets which were large enough to preclude the possibility of reflected stress waves in the neighborhood of the two charges during the observation period.

Obstruction of the field of view by smoke was a serious problem in this series of tests; however, it was possible to obtain data for three different models. The geometric parameters for these three models are shown in Table 5.1. The explosive charge was lead azide(PbN_6) which was packed into the holes while wet and then permitted to dry. The charges were detonated with two matched resistance bridge wires that were activated with a 2000 volt pulse from a 10 μfd. capacitor. Smoke shielding was provided by Lexan tubes 1 in. OD with a 1/16 in. wall bonded to both surfaces of the model with silicon rubber adhesive.

Photoelastic fringe patterns were recorded together with the moving crack fronts by photographing the dynamic event in the multiple spark camera at a framing rate of 120,000 frames/sec.

Table 5.1

Description of Models with Two Centers of Dilatation Charge

Model No.	Spacing s (in.)	Diameter d (in.)	Weight w (grams)	Model Thickness h (in.)
H-23	3	0.5	1.0	1/4
H-27	4	0.5	0.9	3/16
H-28	3	0.5*	0.6	3/16

*Hole containing the charge was lined with a brass insert 0.5 OD and 0.020 in. wall thickness.

5.3 Experimental Results

Model H-27

Of the three experiments described in Section 5.2, model H-27 provided the best defined fringe pattern and very clear indications of the crack fronts. For this reason, it will be the first test described. Model H-27 contained two charges each 1/2 in. in diameter located 4 in. apart. Detonation of the two matched bridge wires was simultaneous as indicated by the photoelastic fringe pattern shown in frame 27-1 of Fig. 5.2.1. Inspection of frame 27-1 shows that the radially expanding P fronts have overlapped and that the two waves are reinforcing each other along the center line connecting the two holes. The shear wave has been formed and is propagating radially outward. Cracks originating at the boundaries of the holes are just extending beyond the shields.

In frame 27-3, also depicted in Fig. 5.2.1, three different important events are occurring simultaneously. First, at point X an interior fracture is evident. While the definition of this fracture is obscured by the ghost image, it is believed that this fracture is produced by the P wave originating at the left-hand source. Second, the P wave originating at the right-hand source is interacting with the radial cracks extending beyond the smoke shields on the left-hand charge and vice-versa. As will be established later, this interaction of the P wave with the radial cracks produced extensive branching but only modest crack extension. The third event illustrated in frame 27-3 is the beginning of the over-lap of the two S waves on the center line between the two charges

The development of the dynamic fracture pattern is illustrated in Fig. 5.2.2 where frames 27-4 and 27-5 are presented. The interaction of the P wave with the radial cracks extending into the region between the two

explosive charges is complete in frame 27-4. Its effect has been to produce extensive branching of the cracks but only modest extensions. The interactions of the two shear waves is complete and no fracture has been produced. The interior fracture at point X begins to extend in a crack pattern which resembles a Y. The stresses acting on these cracks as well as the radial cracks extending into the region between the two holes is associated with the second and third pulses in the tail of the P wave.

The form of the P wave is evident in frame 27-5 of Fig. 5.2.2 where the photoelastic pattern can be observed with excellent definition. The profile of both the P and the S waves along a radial line through this fringe pattern is shown in Fig. 5.3. It is this tensile region behind the compressive front of the P wave which is important in producing the crack extensions during this phase of the event. Inspection of the radial cracks extending from the charges and the Y shaped crack at the interior fracture show that significant crack growth does occur during this between wave (between the primary P and S waves) phase.

The interaction of the S wave with the cracks is depicted in both frames 27-6 and 27-7 presented in Fig. 5.2.3. In frame 27-6, the incident S wave from the left-hand source is reflecting from two branches of the Y type crack. It is also evident that the incident S waves from both sources are interacting with the radial cracks extending into the region between the two charges. Reference to frame 27-7 shows that the S wave interaction in the region between the holes is essentially complete and that crack extensions were modest during this period.

The arrest phase of the fracture process is illustrated in Fig. 5.2.4 where frames 27-8, 27-12 and 27-15 are shown. The two incident P and the

two incident S waves have all propagated through the region between the two explosive charges. Relatively low level stresses remain in the region due to the stresses in the tails of the incident waves or due to reflections of waves from the crack boundaries. These stresses decay slowly with respect to time as indicated in Fig. 5.2.4 where the period of observation between frame 27-8 and 27-15 is 87 to 157 μsec for a total of 70 μsec. Almost all of the cracks arrest during this period; however, the crack growth for a few cracks is significant since the time available for growth even at relatively low velocities is relatively long.

The final crack pattern is shown in Fig. 5.4. This photograph was taken after the test was complete and the cracks have been extended much further than indicated by the arrest pattern shown in frame 27-15 of Fig. 5.2.4. After the dynamic observation period, reflected stress waves from the boundary of the model propagated into the region between the two explosive charges and produced further extension of many of the cracks. In spite of these crack extensions many features of the dynamic crack extension process can be observed on this static photograph. These include the many short radial cracks due to the P and S waves from the same source, the multiple branching due to the P wave from the other source, the internal fracture, and arrest of the cracks at markedly different lengths.

The test of model H-27 did produce internal fracture but the cracks did not extend from one hole to the next so as to result in a continuous fracture plane between the two sources.

Model H-23

The loading of one gram of lead azide in each of the 0.5 in. holes placed on three in. centers provided relatively intense stress waves and resulted in both internal fracture and a crack path between the two sources. The details of the dynamic stress and fracture process are pre-

sented in Fig. 5.5.

The early phase of the event is represented in frame 23-2 in Fig. 5.5.1. The stress waves are so intense that the resulting photoelastic fringe pattern cannot be resolved except for the location of the front of the waves. The symmetry of the pattern indicates that the two charges were detonated simultaneously. The P waves have already interacted and there is a ghost image indicating an internal fracture near the center line. The P waves from both sources are interacting with the cracks extending from the opposite charges; however, the details of this interaction are obscure because of the high intensity of the stress wave and because of the fact that the radial cracks have not extended beyond the shields.

Reference to frame 23-4 shows more detail of the fracture process. The size and shape of the internal fracture can be noted. The radial cracks have also extended beyond the shields and the locations of the crack tips are evident. It is also clear that many of these radial cracks have undergone extensive branching. The incident P waves have propagated through the adjacent charges and they are no longer a factor in producing crack propagation in the region between the two charges. The incident S waves from both sources are beginning to interact with the radial cracks extending from the opposite explosive charge, although the details of this interaction is still obscured by the lack of resolution.

Better detail of the dynamic fracture patterns are evident in Fig. 5.5.2 where frames 23-5 and 23-6 are depicted. In frame 23-5 the heavy branching which occurred at all of the cracks clearly indicates that the effect of very intense stress fields is not to rapidly propagate the crack but to expend its energy by creating new branches.

As the incident S waves interacts with the radial and branched cracks,one of the branches becomes predominate and begins to propagate. This fact is demonstrated by the crack labeled B in frame 23-6. Smoke escaping from the shields is beginning to obscure the radial cracks near the boundaries but enough visibility remains to indicate that with only a few exceptions the multiply branched cracks are stable.

The final phase of the crack propagation is presented in Fig. 5.5.3 where frame 23-7, 23-9 and 23-14 are shown. The effects of the two incident P and the two incident S waves is past. The stresses presented in the region between the two explosive charges are due to the pulses in the tail of the P and S waves and due to waves reflected from the fracture surfaces. During this period from 68 to 114 μsec a few cracks from the many branch cracks reinitiate and begin to propagate. The cracks labeled E in all three frames are indicative of cracks which have reinitiated and propagated an appreciable distance during this final part of the event.

The final crack pattern presented in Fig. 5.6 indicates that juncture of the cracks from the explosive charges with the cracks originating from the internal source occurred. This photograph again shows short radial cracks beginning at the boundary of the explosive charge arrested after extensive branching with a few branches reactivated to propagate relatively long distances in the final phase. The junction of these different cracks provides for breakage of the material between these two holes.

Model H-28

The holes containing the explosive charges in model H-28 were lined with thin walled brass inserts. Unfortunately these brass inserts

ruptured at a location near the surface of the model and the smoke and light which was not properly contained degraded the contrast observed in the first four frames. For this reason the early portion of the event can not be described. The first distinguishable frame (28-5) is presented in Fig. 5.7.1 and indicates that the loading is symmetric. The P and S waves have already propagated out of the center region between the two holes. While some ghost images of the cracks are present, it is possible to identify the same characteristic results namely initiation, branching, arrest and reinitation. No internal fractures were produced and breakage of the region between the two holes, must be accomplished by extending the cracks through larger distances.

The crack extension in the final phase of the dynamic process illustrated in Figs. 5.7.2 and 5.7.3. Frames 28-9, 28-10 and 28-12 show growth of several cracks at relatively high velocities; however as these cracks extend further into the region (see Fig. 5.7.3.) the cracks labeled A, B, C and E arrest. Propagation of D, F and the branch crack G continues until a breakage path between the two explosive charges is formed.

A photograph of the final static crack pattern presented in Fig. 5.8 shows more extensive cracking than that shown in frame 28-16 in Fig. 5.7.3. It is believed that these cracks were reinitiated by stress waves reflecting from the boundary.

While these results are preliminary it appears that the insert was of benefit in producing extended cracks in the final phase of crack propagation.

5.4 Analysis of Data

A quantative analysis of the data obtained is difficult for several reasons. First, the amount of data gathered was limited in view of the very complex behavior of the crack and stress wave interaction. Second, it was often difficult to precisely locate the crack tips due either to smoke obscuring the model or the ghost image recorded by the system. Third, it should be realized that fracture is a statistical phenomenon and reproducibility of each phase of the event has not been established with any quantative measure. In spite of these difficulties it was possible to make some measurements and to provide some numerical data describing the event.

As described in Section 5.3 the dynamic event could be divided into four phases 1) growth of the primary radial cracks, 2) multiple branching and arrest, 3) growth of a few branches and 4) final propagation and arrest. This sequence of events is illustrated schematically in Fig. 5.9 where the geometry followed by the development of a typical crack is given.

Model H-27

Measurements made on model H-27 indicated that the longer of the primary radial cracks extended beyond the boundary of the hole 0.45 to 0.55 in. These cracks were formed during the first 30 μsec of the event; thus, the average crack velocity $\dot{U}_r$ was approximately 16,000 in/sec.

The opposite P wave arrived at these crack tips at a time of 30 to 35 μsec after detonation and greatly increased the stress level. This systematically produced multiple branching with the primary radial crack dividing into several branches. The branches grow progressively during the passage of the main pulse of the opposite P wave and the subsequent

secondary pulses in the tail of the wave. During this time interval from 30 to 65 μsec the branches grow to 0.3 to 0.4 in. long which corresponds to an average velocity of about 10,000 in/sec. After achieving this length most of the branches arrest.

The opposite S wave arrives at the location of the branches cracks at about t = 65 μsec and sweeps through the crack tips in about 15 μsec. A few of the branches of the cracks are reinitiated and short extensions 0.15 to 0.20 in. take place with relatively high crack velocities (20,000 in/sec). Growth of the C and G cracks in Fig. 5.2.3 demonstrate the rapid growth of a few cracks due to the influence of the S wave.

During the final period from t = 80 to 160 μsec most of the cracks arrest; however, a few do continue to propagate such as B and C in Fig. 5.2.4. Crack C extends 0.66 in. in a 81 μsec interval with an average crack velocity of 8000 in/sec and crack B extends 0.24 in. in 70 μsec for an average velocity of 3000 in/sec.

The arrested crack pattern for model H-27 is shown in Fig.504 Measurements of 10 of these cracks showed that the ratio r_a/r_c varied from 4 to 7.6 with an average of 5.3.

The interior fracture which developed at a flaw location in the model propagated early in the event with two branches marked M and K in Fig. 5.2.3. These two branches grew from a combined length of 0.25 in. at 55 μsec to 0.70 in. at 71 μsec with an average velocity of 14,000 in/sec for each branch.

Model H-23

The data obtained from the H-23 model was similar to that obtained from the H-27 model except that the explosive charges were more closely spaced and the loading slightly higher. Measurements indicate that several of the

primary radial cracks extended 0.55 in. beyond the boundary of the hole during the 25 μsec period before the arrival of the opposite P wave. The average crack velocity during this period was about 22,00 in/sec.

Branching was extensive with a very large number of branches being produced by the passage of the opposite P wave. The branches were of course of different length; however, some of the longer branches were in the range of 0.33 to 0.35 in. As these branches developed during the period from 20 to 50 μsec after the detonation, the average crack velocity of the longest branches was 13,000 in/sec. It is believed that the crack velocity of many of the branches was higher than this average value at certain times during in the development of the branch pattern.

The arrival of the opposite S wave resulted in an extension of a few branches in the branched systems. These extensions may be noted as cracks labeled B and C in frame 23-6 of Fig. 5.5.2. These extentions were about 0.1 to 0.15 in. over a 7 μsec interval at a velocity of about 18,000 in/sec. Further extentions of crack B were observed in the final period of crack propagation after the passage of the S wave.

During this final period, the B crack extended a distance of 0.25 over the 22 μsec interval between frame 23-5 and 23-8 at an average velocity of 11,000 in/sec. Two cracks associated with the branched system labeled E were reactivated very late in the dynamic event. This system was stable in from 23-8 (t = 75 μsec) and was reactivated before frame 23-9 at 83 μsec. It is estimated that the longest of the two cracks propagating out of the E system extended a distance of 0.43 in. in 44 μsec between re-initiation in frame 23-13. This corresponds to a velocity of about 10,000 in/sec. Crack D also exhibited a growth of 0.40 in. over the 30 μsec period between frame 23-5 and 23-9 at a velocity of 13,000 in/sec. It appears then

that a few random cracks propagate relatively long distance (0.4 to 0.5 in.) at velocities of 10 to 13 x 10^3 in/sec during the final phase as the dynamic state of stress diminshes toward zero.

Model H-28

Due to resolution difficulties in the early phase of the experiment, the dynamic photoelastic fringe and crack patterns could not be analyzed. Nevertheless, the crack pattern shown in Fig. 5.7.1 does provide some measurements related to this early period. First, the primary radial cracks extend beyond the boundary of the holes containing the charge by a distance of 0.55 which is identical to that measured for the H-23 model. Multiple branching of these primary radial cracks took place but it was less extensive than that noted with the more highly loaded H-23 model. Branch lengths of 0.3 in. were common.

The final phase of the dynamic event shows several different characteristics. The branched system of cracks labeled C remained arrested while a similar system labeled F on the opposite side was reactivated with major extensions of the primary radial crack and the branch identified by G. Cracks A and B reinitiated and propagated a short distance 0.15 in. and then arrested. Average velocity during the period of propagation (22 μsec) was about 7000 in/sec.

Large extensions of crack D and branch G occurred which permitted breakage across the section. Crack D extended 0.85 in. after reinitiating one of the branches in the D system. The last 0.45 in. of this extension took place over a period of 30 μsec; thus, the average velocity was 15,000 in/sec during the final phase of crack propagation.

Branch G which reinitiated between frame 28-9 and 28-10 extended by 0.55 in. during a 54 μsec time period at an average velocity of about 10,000 in/sec.

5.5 Conclusions

The development of the fracture pattern in the region between two explosive charges was divided into four phases. The first phase involved the growth of primary radial cracks with a velocity $\dot{U}_r$ of 16 to 22 x 10^3 in/sec to a length of about twice the charge radii. The second phase consisted of multiple branching of these primary radial cracks by the P wave originating at the adjacent charge. The number of branches depended on the intensity of the P wave with only a few branches for the smaller charges to perhaps 50 branches for the larger charges. The longest branches rarely exceed 1.5 times the radius of the explosive charge. Velocity of the branches was difficult to estimate; however, it is believed that they propagated at a relatively low velocity of about 10,000 in/sec. Most of the branched systems of cracks arrested prior to the arrival of the S wave.

The third phase involves the interaction of the S wave with the arrested branched systems. A few of the larger cracks in the branched systems are reinitiated. These crack extensions are usually short and rarely exceed the radius of the hole. In spite of their shortness, the extensions occur with relatively high velocity of 18 to 20 x 10^3 in/sec. The relatively short pulse length of the S wave limits the time available for this wave to extend the crack.

The final phase of the event occurred after the passage of the S waves and included the time period where the stress state in the region between the two holes decayed to zero. This time period was relatively large as the decay of the stress state required 80 to 100 μsec. At the beginning of this period several cracks (5 or 6) would usually be propagating and occasionally a branch of an arrested system will reinitiate an add another propagating crack. As the stress system decays, most of the individual cracks arrest after extentions of less than one radii of the explosive charge. Usually one or two cracks continue to propagate and can

achieve extensions of about 2 radii. The crack velocity in these cracks with long extensions was variable and ranged from 8 to 15 x 10^{-6}. It appears there is some minimum value of $\dot{U}_r$; however, it was not possible to determine it in this test sequence. Only in one instance did the crack extensions beyond the branch locations exceed 2 radii. This occurred in model H-28 where crack D extended 3.4 times the charge radii. This large extension may have been due to the influence of the brass liner used between the charge and the boundary of the hole in the model.

Internal fractures occurred but their locations were random. Thus they were produced by the presence of flaws rather than reinforcement of two waves from the left and right hand sources. Branching always occurred with the internal fractures which limited their growth. Typical branch lengths were about 1.5 times the radii. The internal fracture arrested after the passage of the P wave; however it can be reinitiated by the S wave and can contribute in a random way to fracture of the region between the explosive charges.

6.0 Interaction of P and S Waves With Arrested Cracks

6.1 Introduction

It has been observed that the sequence of events for early times after detonation consists of crack initiation and propagation due to the passage of the P and S waves with crack arrest with the further propagation of these waves. Subsequent turning and reinitiation has been found to occur as waves created by the reflections of the P and S waves from free surfaces once again pass over the arrested cracks. Some information on crack stress wave interaction has already been presented in Section 5, but for the most part this information pertains to cracks that have recently stopped or are still growing from one detonation when the stress waves from another detonation pass over them.

In this section investigations are described where pre-existing arrested cracks are observed as only P and S waves pass over them. It differs from data presented earlier in that the cracks were formed by razor blades or detonations which occurred hours before the P and S waves interact with the cracks. Only the passage of P and S waves are discussed since data from passage of PP, PS, SS, and SP waves are contained in earlier sections which deal with reflection from free boundaries.

6.2 Experimental Procedure

The interaction of the P and S waves with arrested crack were investigated using two different types of models. The first series of tests involved using cracks that had been formed from previous detonations while the second involved cracks which were created by a razor blade extension of a saw cut. In all, five different experiments were conducted under this task. Table 6.1 gives the geometric data on the models utilized.

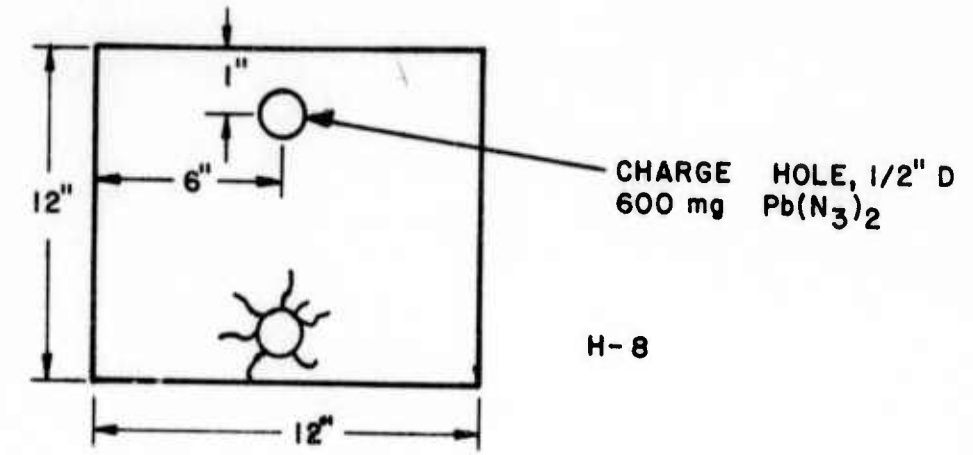

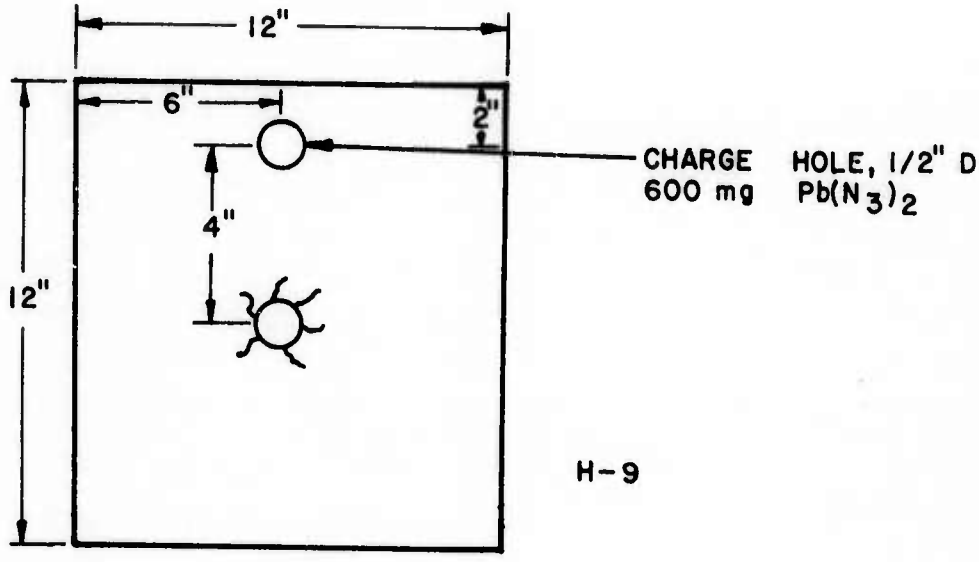

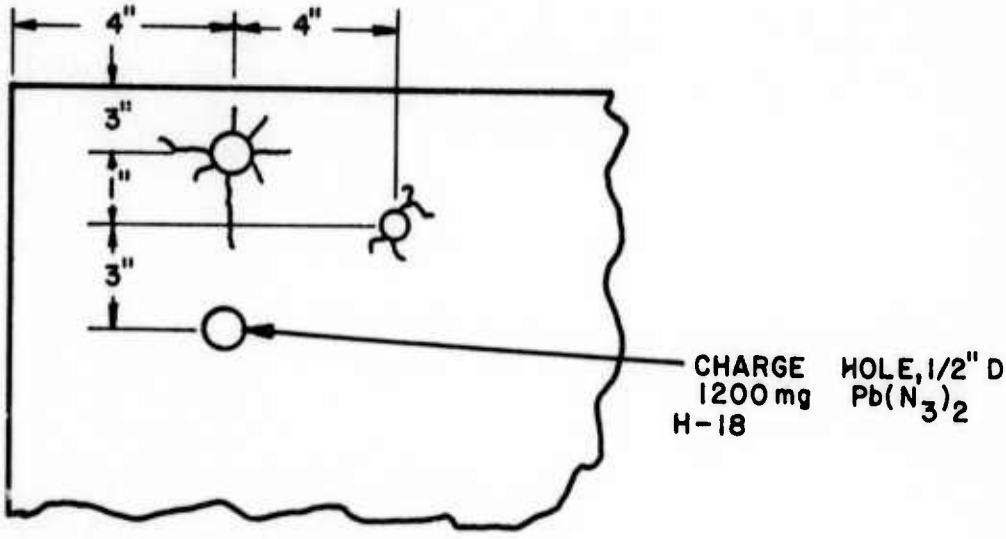

Table 6.1 Geometry of Models Used to Investigate P and S Wave Crack Interaction

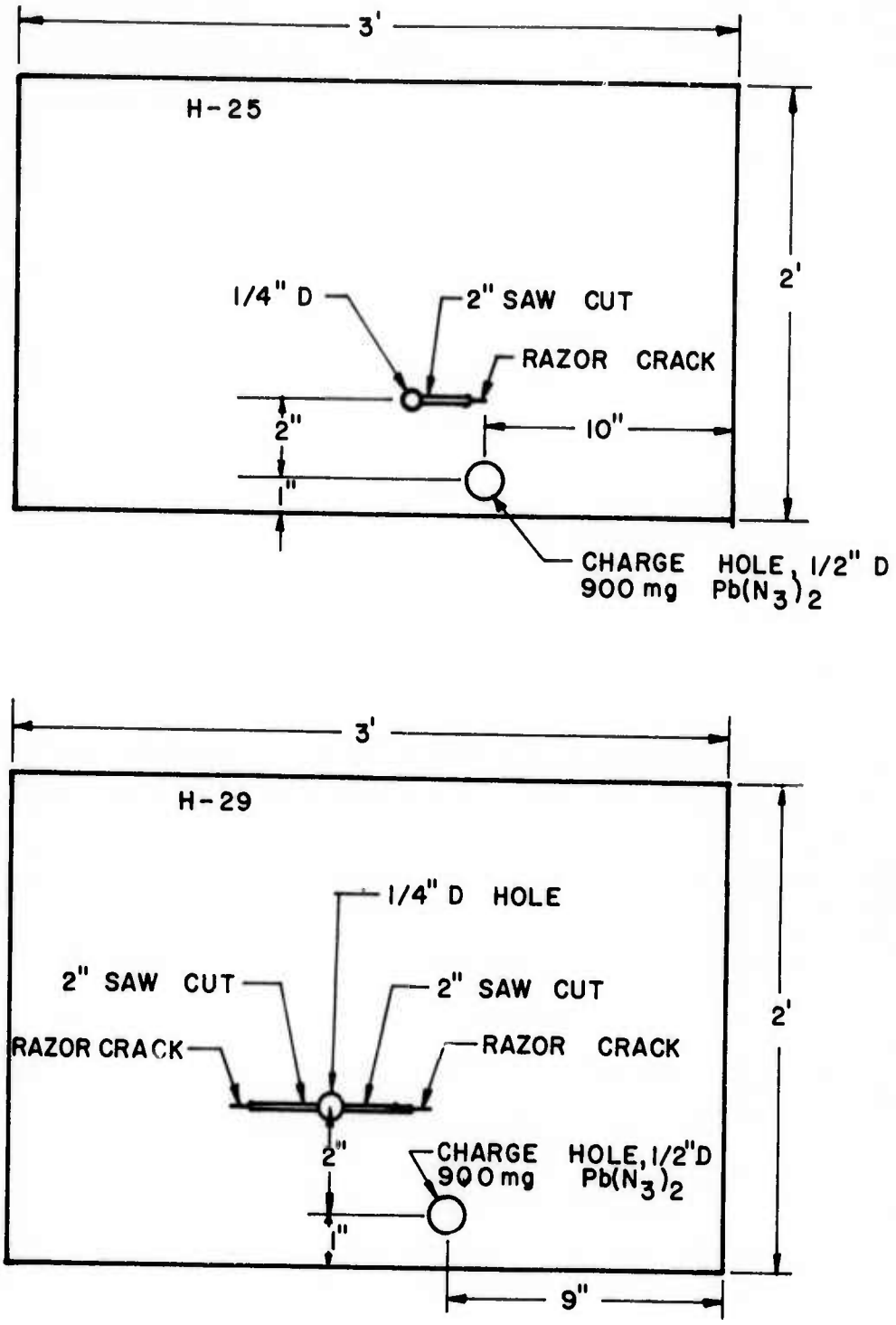

Table 6.1 (cont'd) Geometry of models Used to Investigate P and S Wave Crack Interaction

In the first series of tests (H-8, H-9 and H-18) sheets of Homolite 100 which had been used in previous research and resulted in favorable crack patterns were selected for additional testing. Models were 1/8" thick for H-8 and H-9 while a 1/4" thick sheet was selected for H-18. As has been pointed out, the initial crack patterns were the result of earlier detonations. The crack patterns are not at all similar since not only sheet thickness varied but the size of hole charge as well as volume of charge was different for the original detonations. Fig. 6.1 shows the crack patterns that existed for tests H-8, H-9 and H-18.

Models for tests H-25 and H-29 were 3' x 2' sheets of Homolite 100 (birefringent polymer) 3/16" thick. A 1/4" diameter hole was first drilled in the sheet and a coping saw blade was used to cut a slit 2 inches long according to the geometry shown in Table 6.1. Note that there was only one razor crack present in H-25 while H-29 had two razor cracks present.

Charge holes as indicated in Table 6.1 were drilled and filled with $P6(N_3)_2$. Bridge wires were used to ignite the lead azide and a multiple spark gap camera was used to record the passage of the P and S waves over the pre-existing cracks. As before lexan tubes were cemented to the sheets to keep the smoke from the explosive from obscuring the fringe patterns. The camera has been described in earlier sections and its description will not be repeated here. Sixteen frames were obtained from each test.

6.3 Results

Fig. 6.2 shows the 3rd, 6th, and 12th frame from test H-18. The times represent 43, 49.5 and 62.5 μsec after detonation. The leading edge of the crack labeled F is about three inches from the charge center (distance

between grids is one inch). Fig. 6.2a) shows the leading edge of the P wave enveloping the tip of the crack and about the first inch that is nearest the charge center. Notice from the fringe pattern that the crack is still arrested. This can be determined by noting that the overall fringe pattern is not affected by the presence of the crack. In Fig. 6.2b) the P wave has propagated further, and by counting fringes it can be determined that the tip of the crack is in the trailing portion of the P wave. This portion is tensile whereas the leading part of the wave was compressive. Note, the disturbance shown by the fringe pattern at the crack tip, indicates that the crack is active and has begun to grow in length. Fig. 6.2c) shows the crack just prior to the arrival of the shear wave and the crack seems to have stopped being active once again.

Fig. 6.3 represents frames 14 and 16 from the same test. These frames correspond to times of 67 and 72 μ seconds after detonation. In frame 14 the shear wave has enveloped the crack tip and it appears more active than it did in frame 12. This activity continues as the shear wave continues to propagate.

This activity is still evident in frame 16 presented as Fig. 6.3b). The overall pattern as described here is typical from observations of the data obtained in all of the tests conducted under this task.

Dally and Riley[1] have characterized quite completely the P wave created by a $Pb(N_3)_2$ detonation in CR-39 (another birefringent polymer). CR-39 and Homolite 100 are quite similar with the main difference being that Homolite 100 tends to exhibit more cracking and hence a better defined shear wave in the vicinity of a detonation. The description of the P wave in both materials is expected to be quite similar with the possible exception that

the tail of the P wave would be expected to be stronger in CR-39 than in Homolite 100.

Upon detonation of an explosion they found a biaxial compression state of stress in the leading edge. They were able to separate the two stresses in the wave by a numerical integration technique and found the radial stress component to be roughly three times as large as the tangential component. As this compressive leading edge propagates outward from the source of dilation it was found to be followed by a trailing biaxial tensile pulse. Although there is no experimental evidence to justify the relative magnitudes of the tensile stresses to the compressive stresses, it is felt that they are roughly equal.

The birefringent polymer is a brittle material (as is rock) and hence its tensile ultimate is much smaller than its compressing ultimate. The material then, on feeling this tensile tail, begins to crack - possibly from multiple source locations. This absorbs energy from the tensile tail and the stress level is reduced. The presence of the cracks create an unsymmetric condition which results in shear wave formation. The P and S wave propagate from the source outrunning the propagating cracks and the cracks subsequently arrest. As the P and S waves propagate outward in the media their amplitude is diminished according to some inverse law with respect to r (e.g. K/r).

As stated earlier the ratio of the compressive radial stress to the compressive tangential stress was found to be roughly 3 by Dally and Riley. In the tensile tail the radial stress was found once again to be larger than the tangential stress with a ratio of σ_r/σ_{tang} of roughly 1.4. The stress state in the propagating P wave is as depicted in Fig. 6.4.

When the P wave first envelops a crack tip a biaxial compressive state of stress is present, and the crack tends to close and remains inactive. As the wave propagates further the crack is subjected to a biaxial tensile state of stress and opens up and begins to propagate.

The passage of the shear wave is completely different from the P wave. In a shear wave the material elements undergo no change in volume. The principal normal stresses are equal to each other but opposite in magnitude. As a shear stress wave passes over a crack it could either be activated or be forced to close depending upon the orientation of the crack with respect to the principal stress directions in the wave.

6.4 Data Analysis

Six frames from test H-8 are shown in Fig. 6.5. Of particular interest are the two cracks labeled B and D. Both of these cracks are subjected only to the passage of the P wave during the duration of the test. In the first frame presented the compressive leading portion of the P wave has just passed over the tip of crack B - having already cleared the tip of crack D. It is a lower order P wave possessing only 1 fringe order.

The tensile tail has activated crack B whereas crack D also being subjected to a biaxial state of tensile stress is still inactive.

Fig. 6.6 exhibits Mohr's circle for the P wave tensile tail and the states of stress present for both cracks. (Mohr's circle represents the state of stress in any direction at a given point in a body.) Here it has been assumed that the radial stress is equal to $2.6x$ (where x can be any value depending upon the relative position of the point in question and the peak of the propagating P wave). The tangential stress is assumed to be $1.9x$.

The orientation of crack B is observed to be 47 degrees clockwise from the tangential direction. Crack D is 36 degrees counter-clockwise from the tangential direction. Using the Mohr's circle shown as being valid for both points B and D yields the states of stress shown in Fig. 6.6 for the crack orientations of B and D. Crack D at the tip is subject to a $2.226x$ normal stress in a direction perpendicular to it and a $2.264x$ normal stress in a direction along the crack with both faces being subject to a shear stress of $.348x$. Crack D has normal stresses of $2.36x$ psi perpendicular to the crack and $2.14x$ psi along the crack with a shear stress of $0.33x$ on both faces. The states of stress on both cracks are very similar. From Fig. 6.5a) crack B is active while crack D is not. In the next frame crack D is active as well and both remain active throughout the test as can be observed from Fig. 6.5f) which was the last photograph taken at 187 μsec after detonation.

The lens of the multiple spark gap camera remains open for the entire time of the test and images on the film are obtained when the spark gap that is aligned with a particular lens breaks down and focuses an image on the large sheet of film located in the camera back. The camera being utilized produces what has been referred to earlier as ghost images. These are in general the final crack pattern which are superposed on the test data and are the result of stray light being picked up within the optics after the test is complete. These ghost images are unwanted from the standpoint that it requires closer examination and a disturbance in the fringe pattern to determine where the crack tips are located at the particular time that the spark gaps break down. These same ghost images are useful from the standpoint that in each frame in which they appear it is possible to determine the direction the crack will ultimately take and how

far it will propagate during the entire test.

By close observation of Fig. 6.5b) one can see the ghost images of both crack B and D. These ghost images show that the cracks turn and tend to align themselves in the tangential directions. This is logical since the maximum principal stress occurs in the radial direction and one would expect there would be a tendency towards the crack favoring the tangential direction. How much of this turning action is due to the P wave passage and how much is due to the S waves and the reflected waves cannot be ascertained for certain. Close examination of 6.5f), however, shows that at this point in time (before the shear wave or reflected waves have arrived) that some turning has occurred and that the cracks have already begun their reorientation due to the radial stress being the maximum.

The turning of the cracks can also be observed from 6.7 showing crack growth as a function of time. The crack velocity tends to fall off as it turns but then increases afterwards to approach the same velocity as it had before. The two cracks are propagating at different velocities with the velocity of crack D larger than crack B.

The lengths of the cracks B and D do not increase appreciably due to the passage of the tensile tail of the P wave. This is also shown in Fig. 6.7 where the maximum crack growth which occurs for crack D is less than .4 inches.

The same turning characteristic is evident from Fig. 6.8 which exhibits four frames from test H-9. Note crack A as the P wave tensile tail passes over it. Its direction is originally approximately 45° from the tangential. In Fig. 6.8d) just prior to the arrival of the shear wave it has turned and is now oriented in a tangential direction. There is also more growth present in this test since there appears to be more muscle in the P wave. Fig. 6.9 shows radial crack growth as a function of time for

cracks A and D shown in Fig. 6.8 for test H-9. At the same time that crack A has turned to the tangential direction crack E appears to be turning first toward the tangential direction and then to hook toward the radial orientation. This crack, however, is being acted upon at the instant of the radial turn not only by the P wave but also by a wave that is reflecting off the free surface of the hole in which the initial detonation was placed.

Fig. 6.10 shows the sequence of photographs of cracks A and E from test H-9 as the shear wave envelops them. The cracks are kept active during the shear wave passage but there is no apparent turning of the cracks. Keep in mind that in the shear wave the maximum normal stresses occur are equal in magnitude and opposite in sign, and one would expect the cracks to reorient themselves to coincide with the direction of the tensile principal stress. There are two reasons why it is possible that this isn't seen in the passage of the shear wave. The first is that in addition to the stress distribution in the shear wave being non-symmetrical that there is much lower stress levels present. This can be determined by counting the fringe order in the P wave and comparing it with the fringe order present in the shear wave. For the case depicted in Fig. 6.10 the ratio of the fringe order in the P wave to the S wave is about 3 to 2. Secondly, according to the Mohr's circle representation of stress for the two waves the following should be noted. Even for the same fringe order the photoelastic data is proportional to the difference in principle stresses $\sigma_1 - \sigma_2$. The Mohr's circle for the shear wave is centered at the origin of the σ - τ axes while in the P wave the center of the circle has been shifted to the right by $(\sigma_1 + \sigma_2)/2$. The values of the individual normal stresses are always higher in the P wave than in the shear wave. The conclusion is therefore that there is enough normal tensile stress available in the shear wave to keep

the cracks propagating but not a high enough level to cause a reorientation of the cracks in the direction of the maximum normal stress.

From Fig. 6.9 it is evident that although crack A continues to propagate while under the influence of the S wave there appears to be a lowering of the propagation velocity. In fact, crack D appears to stop growing as is evident from Fig. 6.9 as well as Fig. 6.11a) which shows the frame taken at 144 μsec after detonation. It begins to propagate once again in Fig. 6.12b) when it is subjected to the passage of a reflected wave (PP) from the left side of the model. Recall that this same crack (E) also was affected earlier by reflection from the borehole of the original detonation.

The tests which were conducted with razor blade - induced cracks (H-25 and H-29) resulted in fringe patterns which were too complicated to shed much light on the interaction of P and S waves with arrested cracks. Fig. 6.12 shows four frames from the H-29 tests representing times of 36, 58, 80 and 117 μsec after detonation.

There is a generation of reflected waves from the surface of the saw cut directly above the detonation as is evident from viewing the first frame in Fig. 6.12a). As this wave propagates along the saw cut to the right it does not pass over the razor cut on the left side of the saw cut. The crack marked I on the right end is, however, acted upon by the reflected wave. Note from 6.12b) the high fringe order in this wave as it reaches the right end of the saw cut. Note also that due to the relative location of the razor crack on the left end of the saw cut with respect to the detonation location that waves reflected from the free boundary do not pass over this crack (PS and SS waves are not created upon normal incidence to a boundary). There is no perceptable growth of the razor crack on the left

side of the saw cut. The crack I on the right side turns upward almost perpendicular to the original direction and grows by a considerable amount during the test. This radial crack growth is shown in Fig. 6.13 as a function of time after detonation.

Even though there was no extension of the razor crack directly above the charge hole two cracks were started from stress raises left by the coping saw blade in the vicinity of the left side of the saw cut. These cracks labeled E and F in Fig. 6.12 moved from the saw cut in toward the detonation center during the time of data gathering. The growth of crack E as a function of time is shown in Fig. 6.13. Remember, however, that all cracks in this test with the exception of A and B (which were due to an earlier detonation) were acted upon by reflected waves at practically the same time that the P and S waves passed over them. The results shown for this test are therefore mainly due to these reflected waves and not to the P and S waves. The comparison between the razor crack at the left side of the saw cut and the crack labeled I is a dramatic indication of what was stressed earlier in the report. That is, that there is very little benefit to be derived from the P and S waves alone, and without free surfaces to redirect the energy back into the fracture zone the blasting of material with explosives is very inefficient.

6.5 Conclusions

The interaction of propagating P and S waves from a center of detonation with arrested cracks was examined under this task.

It was observed that the "muscle" of the P and S waves was much smaller than the energy that is available in waves that are reflected from free surfaces.

In general the S wave possessed smaller amounts of energy than the P wave and it was noted that the magnitudes of the maximum normal stresses were in general much higher in a P wave than the maximum normal stresses in an S wave.

As a crack is acted upon by a propagating P wave, the compressive leading part of the wave was found to have no effect upon the crack. When the wave propagated a little further so that the tensile tail of the wave was over the crack it became active and began to propagate with a fixed velocity. There is a reorientation of the crack direction such that the maximum principal normal stress acts perpendicular to the crack. The velocity of propagation of the crack drops off as this turning occurs, but the velocity seems to pick up again and approach the original crack velocity after the turning is completed.

As the S wave passes over the crack it continues to propagate in some cases with a declining velocity. There is apparently no effort at this time for the crack to reorient itself with the principal directions.

The total crack growth during the passage of the P and S waves is not very much, with most of the ultimate crack growth being due to reflected waves from free boundaries.

The velocity of crack propagation due to the passage of P and S waves does not seem to be unique. Different cracks propagate with different velocities due to the influence of the same P and S waves.

7.0 Feasibility Study on the Application of Holographic Recording of Stress Waves in Rocks

7.1 Introduction

Task 7 is a feasibility study of the application of holography to rock mechanics. The project was limited to the study of stress waves induced in a rock sample by an explosive load in a half plane. The use of holography in model studies has one very important advantage over other methods usually employed, and that is that the actual rock material may be used. Thus it was hoped that pictures of a stress wave propagating through the rock would show regions of cracks and flaws in the rock specimen, and by analysis lead to a better understanding of wave propagation through and around these flaws. It should be mentioned that while one would like to study fragmentation and comminution in the rock, it is not possible to do this with holography due to the magnitude of the specimen displacements during these fracturing processes.

7.2 Review of the Holographic Method

Consider the arrangement as shown in Fig. 7.1. A pulsed ruby laser, to be described later, emits light at 6943A^{o} which is split into two components by a beam splitter. One portion, now known as the object beam, strikes the rock specimen and a portion of this light is reflected from the diffuse surface of the rock onto a photographic emulsion called a holographic plate. While all this is happening the other portion of the light from the laser, known as the reference beam, reflects from several mirrors and strikes the holographic film at the same time as the light from the surface of the rock. Because the light from the laser is both spatially and temporarlly coherent an interference pattern is

formed in the holographic film. The film is then processed by normal techniques, allowed to dry and then replaced in the same position used during the exposure. The processed film is called a hologram and is illuminated by just the reference beam. The hologram behaves as a diffraction grating and if an observer would place his eye as shown in the figure he would see a three-dimensional image of the rock that is indistinguishable from the rock itself.

Now suppose that the laser is pulsed twice, but between the two exposures the rock model is loaded and thus undergoes some type of deformation. If the film is processed as before and illuminated with the reference beam, fringes that are related to the deformation of the model appear in the image near or on the surface of the rock. The light intensity of the image is written as

$$I = 1 + \cos \frac{2\pi}{\lambda} \left[(\hat{r}_s + \hat{r}_h) \cdot \bar{d} \right] \tag{7.1}$$

where $\bar{d}$ is the vector displacement at a point on the surface of the specimen, and $\hat{r}_s$ and $\hat{r}_h$ are unit vectors in the direction of the source and holographic film respectively. These vectors are illustrated in Fig. 7.2, and are referenced to a cartesian coordinate system located on the surface of the model.

The usual experimental placement of the optical elements in holography is such that $\hat{r}_s$ and $\hat{r}_h$ are co-planar and lie in the x-z plane. If this is the case, then these vectors may be written as

$$\begin{aligned} \hat{r}_s &= -\sin \beta \, \hat{i} + \cos \beta \, \hat{k} \\ \hat{r}_h &= \sin \alpha \, \hat{i} + \cos \alpha \, \hat{k} \end{aligned} \tag{7.2}$$

as shown in Fig. 7.3. These vectors are known quantities and are

determined by measurement before the experiment.

The unknown surface displacement is written as

$$\bar{d} = u\hat{i} + v\hat{j} + w\hat{k} \tag{7.3}$$

Performing the indicated dot product in Eq (7.1) yields

$$(\hat{r}_s + \hat{r}_h) \cdot \bar{d} = (-\sin\beta + \sin\alpha)\, u + (\cos\beta + \cos\alpha)w \tag{7.4}$$

Thus the arguement of the cosine function describing the intensity of the reconstructed image contains only the x and z components of the surface displacement. It appears that there are two unknowns and only one equation to find u and w. However, several cases arise that permit a solution to the above. The first is when the angle α equals the angle β; then u drops out and w may be solved for directly. Also, if α and β are small or zero then just w remains. If the specimen is large then it is not possible for α to equal β or both to be zero everywhere and so another method must be used. This entails viewing the image through the hologram from two different angles. As the observer does this (or a camera) the fringe pattern shifts and hence another intensity is obtained for a point on the surface of the specimen. This information along with the angles α and α' (the other viewing position) allow for the solution of u and w. If the fringe shift is not appreciable then multiple holograms with considerably different viewing angles must be used.

7.3 Experimental Apparatus

A pulsed ruby laser, built in part with contract funds, was used in this study. It was specifically constructed for use in holography, and emits single or multiple light pulses of 40 nanosecond duration with an energy of 10 micro joules per pulse. A temperature tuned Fabry-Perot etalon controls the longitudinal mode structure of the laser,

and a 2 mm diaphragm controls the transverse mode structure. The laser is shown in Fig. 7.4.

The lenses and mirrors were of average optical quality. It is to be noted that a spatial filter used in most static holography arrangements to remove unwanted diffraction effects from dust and imperfections on the optical components may not be used with a ruby laser due to the very high energy levels. The film was Agfa-Gevaert 10E75 and was processed in Kokak's D-19 for eight minutes at 70°F.

A normal time sequence for an event is as follows. The flash lamps, which are used to provide the energy to invert the population of ruby, were triggered from a 2.0 KV, 1200 joule capaciter bank. One millisecond later, the laser was Q-spoiled by an electro-optic Q-switch and the first no load exposure of the rock was made. One hundred microseconds afterwards a bridge wire imbedded in the lead azide explosive on top of the rock was vaporized by a 15 KV, 10 joule power supply. The laser was then Q-switched again with a variable delay to make the second exposure of the stress wave propagating in the rock. The time between exposures was variable from 100 to 400 microseconds and thus the entire photographic process was completed in that time. During this period the optical components do not have an opportunity to vibrate and hence vibration isolation systems are not needed.

The specimen was 12 in. x 12 in. x 1 1/4 in. from charcoal granite as furnished in the standard rock sample package provided by the Bureau of Mines. To improve its reflectivity it had been sprayed with a flat white paint. The angle β was 18° and α was 0°.

7.4 Discussion of the Results

Fig. 7.5 shows a picture of the rock taken 24 microseconds after the detonation of the explosive. The first observation is that

the fringe pattern is quite continuous and is nearly symmetric. It had been anticipated that there would be flawed regions in the sample, but such was not the case as evidenced by the smooth fringe pattern. In fact, this picture is quite similar to others taken with a homogeneous isotropic aluminum plate as the specimen. Thus one can conclude that it is quite appropriate to model certain types of rock with photoelastic materials when only the elastic wave propagation is to be studied.

Before the next observation can be made some review of the wave propagation phenomena is necessary. It is well known that two types of waves may propagate in the interior of a specimen. The plane dilatational wave (also known as the longitudinal or ^{p} wave) displays a particle motion that is in the plane of the specimen and in the direction of the wave. The other wave is the distortional one (also known as the transverse and S) and for the plane case the particle motion is perpendicular to wavefront and lies in the plane of the specimen. If there is a free edge then a Rayleigh wave is present near the edge. Also additional reflected waves are produced due to the grazing incidence of the primary P and S waves. The relative wave velocities for this material are $C_p = 2.34 \times 10^5$ in/sec, $C_s = 1.242 \times 10^5$ in/sec, and $C_r = .927\ c_s$.

Superimposed in Fig. 7.5 are the theoretical positions of the P and S waves at this instant of time. It is immediately apparent that holographic fringes result primarily from something that travels with or near an S wave velocity. The lack of response of the hologram to the P wave can be explained by magnitude of the explosive (200 mg of lead azide). If there is a low stress level in the rock then there will be very little particle displacement in both the direction of the wave propagation and perpendicular to it (out of plane). For example, con-

sider a point somewhere on the negative y axis just as the P wave passes. At this instant of time there exist two compressive stresses σ_x and σ_y, with the magnitude of σ_x approximately one third that of σ_y.

If a point in the trailing portion of the P wave is considered then the stresses are tensile and σ_x is approximately three quarters that of σ_y. Since the specimen is assumed to be under a condition of plane stress ($\sigma_z = 0$), then the w surface displacement of the specimen may be found from the stress-strain relationships

$$w = -\frac{vt}{E}\left[\sigma_x + \sigma_y\right] \tag{7.5}$$

where t is the thickness and E is the dynamic value of Youngs modulus. After substituting in the properties of charcoal granite Eq (7.5) becomes

$$w = 5.5 \times 10^{-8}\ \sigma_y \text{ in/psi} \quad \text{(leading)} \tag{7.6a}$$

$$w = -7.4 \times 10^{-8}\ \sigma_y \text{ in/psi} \quad \text{(trailing)} \tag{7.6b}$$

Consider now Eq (7.1) after substitution of Eq (7.4) where $\alpha = 0^\circ$ and $\beta = 18^\circ$.

$$I = 1 + \cos\frac{2\pi}{\lambda}\left[-.3\ u + 1.945\ w\right] \tag{7.7}$$

A dark fringe will appear in the image when

$$\frac{\pi}{\lambda}\left[-.3\ u + 1.945\ w\right] = N\pi \qquad N = 1/2,\ 3/2,\ 5/2 \tag{7.8}$$

or

$$-.3\ u + 1.945\ w = N\lambda \tag{7.9}$$

Strictly speaking, the waves are not quite plane at this early time. However, this assumption will be used.

Along the y axis, the u displacement in the P wave is zero because the particle motion is always in the direction of propagation. Thus Eq (7.9) becomes

$$1.945\, w = N\lambda \tag{7.10}$$

Combining Eqs (7.10) and (7.6a) and (7.6b) yields

$$\sigma_y = N\,(2.56 \times 10^2)\ \frac{\text{psi}}{\text{fringe}}\ (C)\quad \text{(leading)} \tag{7.11a}$$

$$\sigma_y = N\,(1.88 \times 10^2)\ \frac{\text{psi}}{\text{fringe}}\ (T)\quad \text{(trailing)} \tag{7.11b}$$

This shows that the hologram is more responsive to the stresses in the trailing portion of the wave than in the head and thus this is where the fringes will show up first. There is approximately a one-half order fringe in the tail and thus

$$\sigma_y = 94 \text{ psi } (T) \tag{7.12}$$

$$\sigma_x = 70 \text{ psi } (T)$$

If with a fixed radial distance in the P wave the θ position is varied contributions due to the a component of the radial displacement are introduced into Eq(7.9) and the analysis becomes much more complex. It was not possible in this series of tests to alter the viewing angle to obtain two different fringe patterns in order to separate out the u and w components of displacement. There simply was not enough change in the fringe pattern to perform even an approximate analysis. This problem could have been overcome by taking two doubley exposed holograms at widely separated positions and then following the process outlined above. However, some

qualitative statements can be made concerning the pattern resulting from the P wave. As the effect of the u component of the radial displacement increases the shape and form of the fringe pattern changes. The slight asymmetry to the photograph results from the fact that u is added to w on one side of the y axis and subtracted from w on the other side; the resulting net effect is to change the symmetry of the pattern.

The above explanation is further corroborated by an examination of Fig. 7.6. The model is Homolite 100 that was roughened on one side, and the viewing and illumination directions were reversed from that of Fig. 7.5. This reversal accounts for the shift to the right of the fringe pattern. Also shown are the theoretical positions for the P and S waves. The specimen was 1/4" thick and its dynamic modulus was 1/20 of that of the rock thus explaining the increase in the number of fringes in the P wave. It is also seen that there are many more fringes in the S wave than in the P wave.

It now remains to provide some explanation to the fringes shown in the S wave. First, the particle motion in a plane S wave is transverse to the direction of propagation. Thus along the y axis, the hologram would be sensitive to this displacement since it is totally in the $\pm$x direction. As the θ position is changed with r constant the particle displacement approaches total movement in the y direction as θ approaches 90^{o}, and the hologram is not sensitive to any motion in the y direction. If the wave is truly a shear wave then there is no w displacement and this can be explained as follows. By definition a shear wave is equivoluminal and this means that both the first invariants of stress I_1 and strain J_1 are zero, or

$$\sigma_x + \sigma_y + \sigma_z = 0$$
$$\epsilon_x + \epsilon_y + \epsilon_z = 0 \qquad (7.13)$$

For plane stress $\sigma_z = 0$ and thus

$$\sigma_x = -\sigma_y \tag{7.14}$$

Then from the stress-strain relationship

$$\epsilon_z = \frac{\sigma_z}{E} - \frac{\nu}{E}(\sigma_x + \sigma_y) \tag{7.15}$$

it is found that $\epsilon_z = 0$ thus

$$\epsilon_x = -\epsilon_y \tag{7.16}$$

Since $\epsilon_z = 0$ there can be no w displacement associated with the S wave. Therefore, the fringe pattern associated with a P and S wave is only a function of the u displacement. By plotting the u displacement as a function of x it is possible to find ϵ_x by differentiating the curve since

$$\epsilon_x = \frac{\partial u}{\partial x} \tag{7.17}$$

then from

$$\epsilon_x = \frac{\sigma_x}{E} - \frac{\nu\sigma_y}{E} \tag{7.18}$$

and Eq (7.14) σ_x becomes.

$$\sigma_x = \frac{\epsilon_x E}{(1+\nu)} \tag{7.19}$$

It is also possible to find $\frac{\partial u}{\partial y}$ which is only a portion of the shearing strain

$$\gamma_{xy} = \frac{\partial u}{\partial y} + \frac{\partial y}{\partial x} \tag{7.20}$$

The v displacement field cannot be found directly from the photograph because of the experimental set-up. It can be obtained indirectly from the fact that since the displacement in the plane S wave is always in the θ direction then the u and v components are related by

$$v = u\tan\theta \tag{7.21}$$

An alternative to this rather laborious task would have been to take another hologram positioned above or below the xz plane. This hologram would be sensitive to the v displacement. Once v is found by either means it must be differentiated with respect to x to complete the other portion of the shearing strain. After the three strain components are found at a point then the principal strains and stresses can be determined.

The above analysis for the plane shear wave depends on the fact that no normal displacement occurs (w), and hence is valid in only those regions where the P and S waves have separated and where there are no reflected waves.

Since this part of the program is only a feasibility study of the application of holography to the study of stress waves in rocks a complete analysis as outlined above will not be undertaken. Instead, the patterns of fringes in the S wave will be qualitatively discussed. Shown in Fig. 7.1 is a picture of the rock taken 60 μsec after detonation. The shear wave at this time is better defined than in Fig. 7.5, and some portions of the wave can be approximated as plane. The leading edge of the S wave has been drawn in and the P wave is out of the picture. Near the edges of the rock numerous reflections have taken place; resulting in

a very complex fringe pattern. As such, the description that follows will be restricted to the region near the y axis. Fig. 7.8 shows the fringe order N, which should be proportional to the u displacement, as of function of x for y = 6.00" and y = 6.58" below the top face of the rock. Since the shape of these curves is proportional to ϵ_x some conclusions regarding the behavior of ϵ_x can be made. Everywhere along the y axis $\partial u/\partial x = 0 = \epsilon_x = \epsilon_y$ and this agrees with the theory. For the shearing strain, the $\frac{\partial u}{\partial y}$ has a value everywhere except ahead of the wave, at the wave peak and behind the wave. This is one portion of the shearing strain; the other part $\frac{\partial v}{\partial x}$ is 0 because there is no component to the displacement along y. Therefore, there appears to a shearing stress along the y axis and this contradicts the theory. One is forced to conclude that this wave is not a pure distortional wave and thus there is a part if not all of fringe pattern produced by the w displacement of the surface.

The possible explanation of this large w displacement traveling with approximately the S wave velocity is that the hologram has recorded the effects of a surface wave. The thickness of the rock was approximately the same as the wavelengths, and this would lead to the generation of surface waves which have a high degree of w displacement.

7.5 Conclusions and Recommendations

There are several conclusions one can draw concerning this feasibility study on the application of holography to the study of stress waves in rocks.

(1) With the present state of the art in holographic interferometry it is not possible to examine fragmentation and comminution due to the large displacement involved. However, if just a single exposure were taken during fragmentation then it would be possible to record in three dimensions the rock fragments. This would be very similar to the work done in two dimensions in Section 6. (2) The rock samples used did not exhibit flawed or cracked regions, and appeared to be homogeneous. Thus if the elastic waves are to be studied then it is appropriate to use birefringent polymers in modeling the rock material. (3) The fringe patterns obtained in this study displayed primarily the w component of displacement. A greater load magnitude and a thinner specimen would have increased the sensitivity of the fringes to the P wave. The fringes in the S wave are believed to have been generated by a surface wave traveling slightly slower than the S wave. (4) In order to determine the stresses in the rock, multiple holograms at widely different positions should be taken.

8.0 Conclusions

Fracture due to an explosive charge is in the form of radial cracks which are produced by the biaxial tensile stresses in the tail of the dilatational wave. The fracture is delayed about three microseconds after initiation of the P wave. Due to multisource initiation the initial crack velocity appears very high; however, when the many small cracks coalesce the radial crack shows only small variations and ranges from 12 to 15 x 10^3 in/sec. The cracks about the center of dilatation produce a relatively low amplitude shear wave. The velocities of the P and S wave of 85 and 50 x 10^3 in/sec respectively are much larger than the crack velocity and thus the energy contained in these stress waves quickly out-distances the cracks. The longer cracks arrested with arrest to charge radii of r_a/r_c = 3.3 - 4.2. It appears that r_a/r_c is a function of the cube root of the explosive charge.

When the charge is placed near the bounding surface of a half-plane the boundary serves as a reflector and enhances the fracturing and fragmentation which occurs. The reflection process is important since it redirects the stress wave back into the fracture zone and because it converts compressive stresses into tensile stresses. Upon reflection the PP wave produces a spall near the free boundary. Depending upon the intensity of the stress wave the spall is either single or multiple and in both cases the length of the spall is usually in the range of 1 to 2 charge diameters. Radial cracks are initiated at the ends of the spall surfaces which propagate toward the free boundary and the charge. These spall induced radial cracks are important in providing a complete path for a fracture surface to

extend from the hole containing the charge to the free boundary. The reflected PP and PS waves reinitiate arrested radial cracks in the local neighborhood of the charge; however, the time period over which these stress wave interact with the crack is so short that crack growth due to the reflected waves is small. Crack propagation also occurs in the post-reflection period as the energy associated with the stress waves gradually decays to the minimum value required to drive the cracks.

Tests with charcoal granite specimens appear to conform many of the results obtained in the photoelastic tests. Spall fracture is also difficult to obtain in the rock material and fracture is obtained in rock by the prolonged extension of a few long cracks as was the case for the polymeric models used in photoelasticity. As the framing camera was too slow to record the cracks propagating in the rock, the data collected pertained to the fragmentation process. Fragment velocities varied widely with values ranging from 30 to 150 in/sec being recorded.

The analysis of two explosive charges in an entire plane indicated that the fracture process involved four different phases. First primary radial cracks were propagated outward to a length about twice the charge radii at a velocity of 16 to 22 x 10^3 in/sec. Next the P wave from the adjacent source produced extensive branching which caused arrest. The S wave from the adjacent source reinitiated one or more branches. The final phase occurred after the passage of the S wave and covered the same period where the stresses in the region between the two holes decayed to zero. Crack growth in this final period occurred at velocities of 8 to 15 x 10^3 in/sec; however due to the relatively large decay time,

the larger crack extensions were significant ranging up to 3.4 times the charge radius.

When an arrested crack is acted upon by a radially expanding P wave, the crack will not reinitiate until the leading compressive pulse in the wave has passed. The cracks are reinitiated by the tensile pulse in the tail of the P wave and propagate at nearly a constant velocity. A re-orientation of the crack direction occurs so that the crack is perpendicular to the maximum tensile stress in the P wave. Crack propagation continues under the action of the S wave. Crack velocity is relatively constant for any given crack; however, crack velocity does vary significantly from crack to crack.

The feasibilities studies in holography indicated that wave propagation in rock materials was continuous and that the charcoal granite material acted as if it were a homogeneous material. The holographic data taken indicated the presence of both an S wave and a Rayleigh wave. Data analysis was involved since a large w component (out of plane displacement) occurred from surface waves generated on the parallel faces of the rock specimen.

Holographic interferometry can be accomplished with rock materials but it appears that the models will have to be thinner than those used here and also the loading will have to be increased significantly to obtain sufficient response to record the dilatational wave.

Bibliography

1. "Stress Wave Propagation in a Half Plane Due to Transient Point Load," by J. W. Dally and W. F. Riley, Developments in Theoretical and Applied Mechanics, Vol. 3, Pergamon Press, New York, 1967, pp. 357-377.

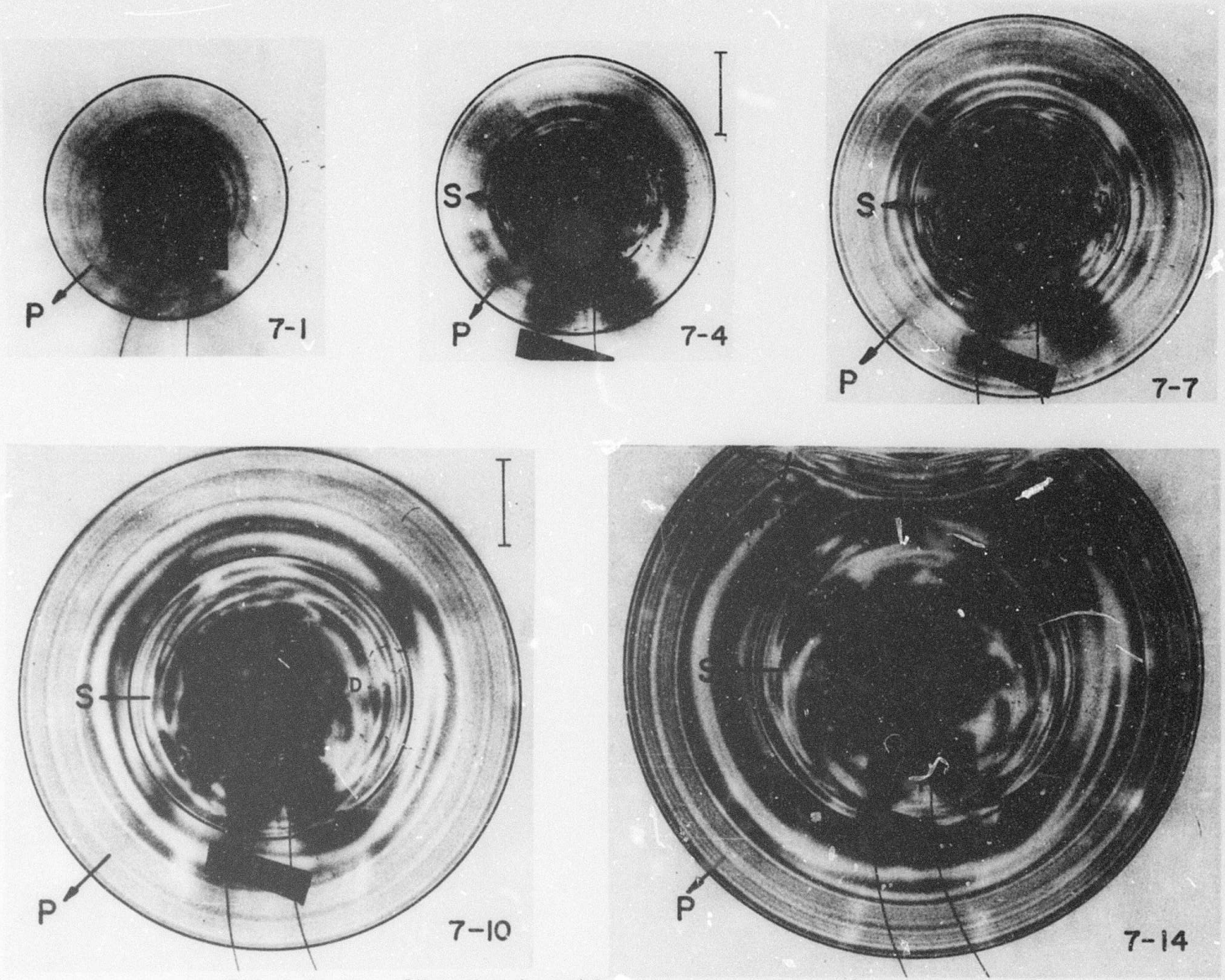

Fig. 2.1 Photoelastic and Dynamic Crack Patterns Due to a Center of Dilatation in an Entire Plane

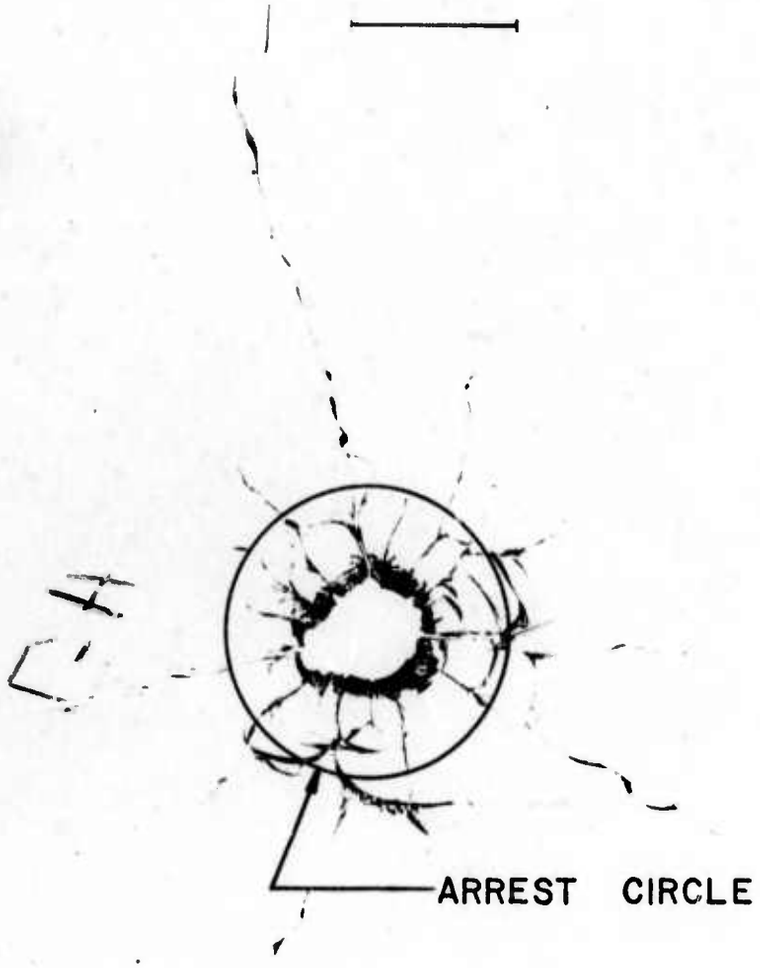

Fig. 2.2 Photograph of the Final Crack Pattern Produced by a Center of Dilatation in an Entire Plane

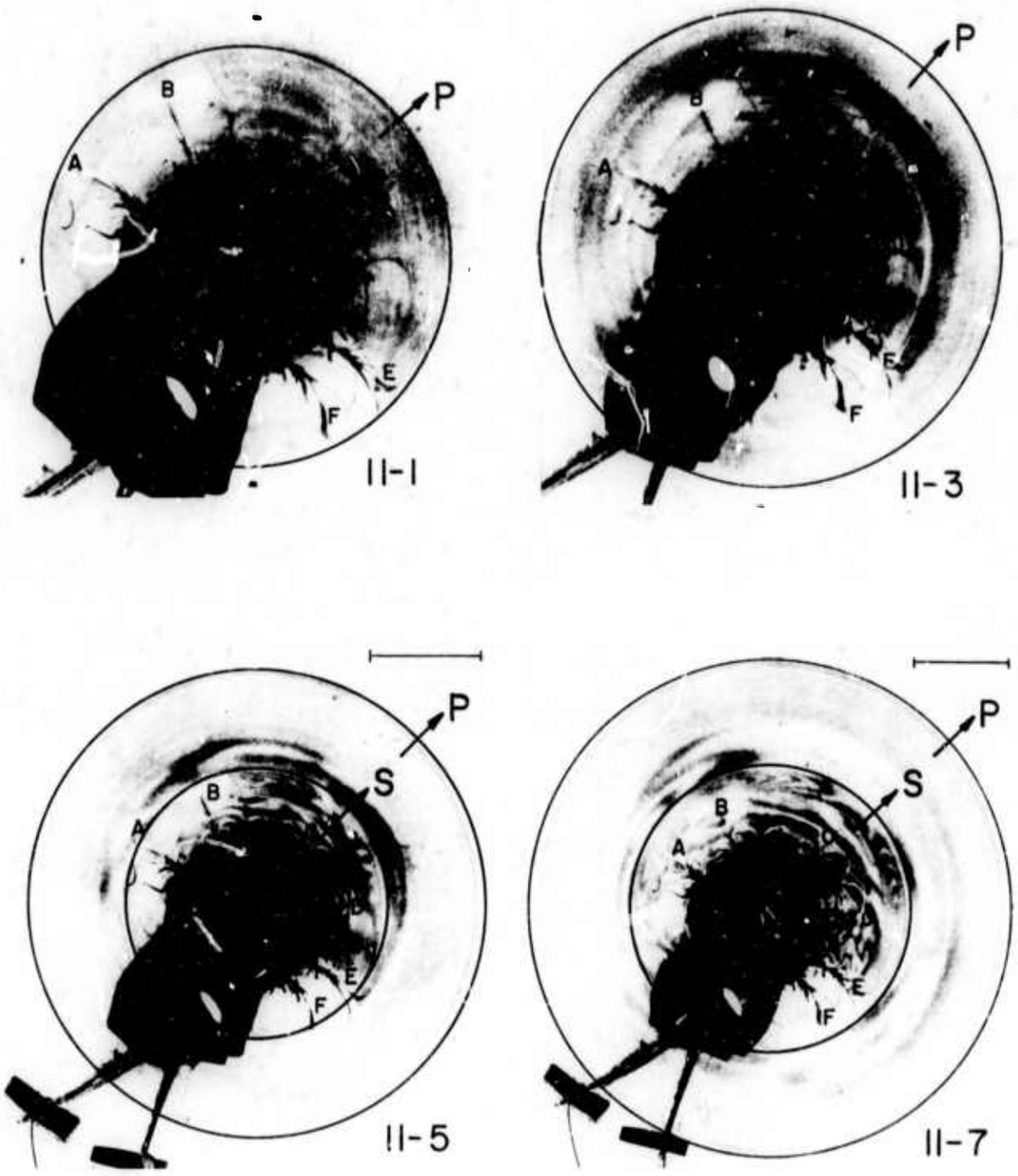

Fig. 2.3.1 Early Event Stress Wave and Crack Initiation

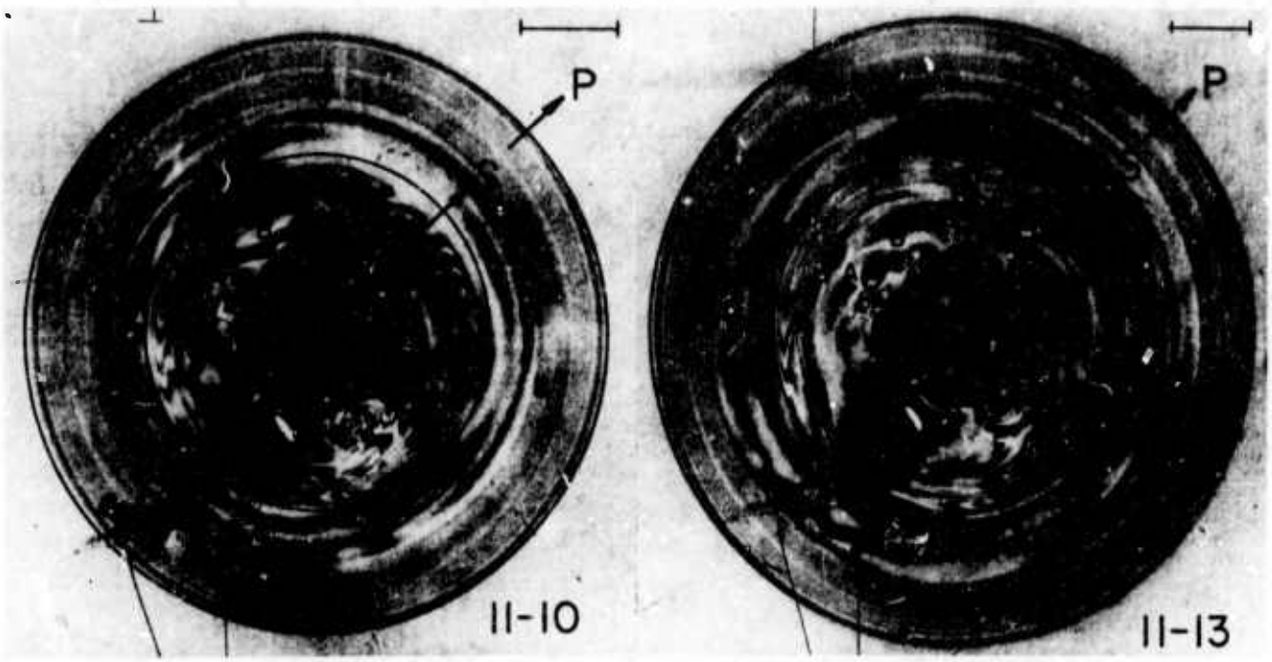

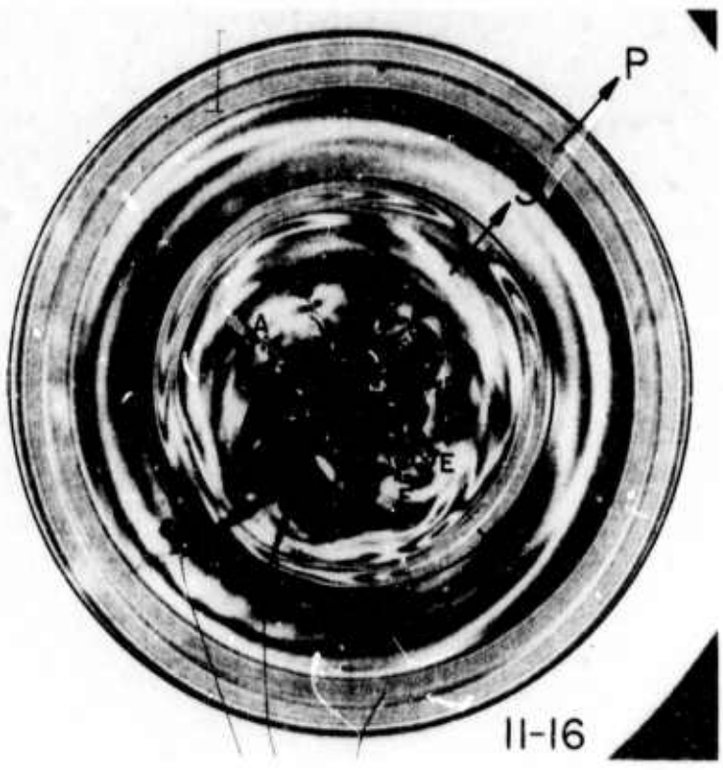

Fig. 2.3.2 Crack Propagation in the Entire Plane

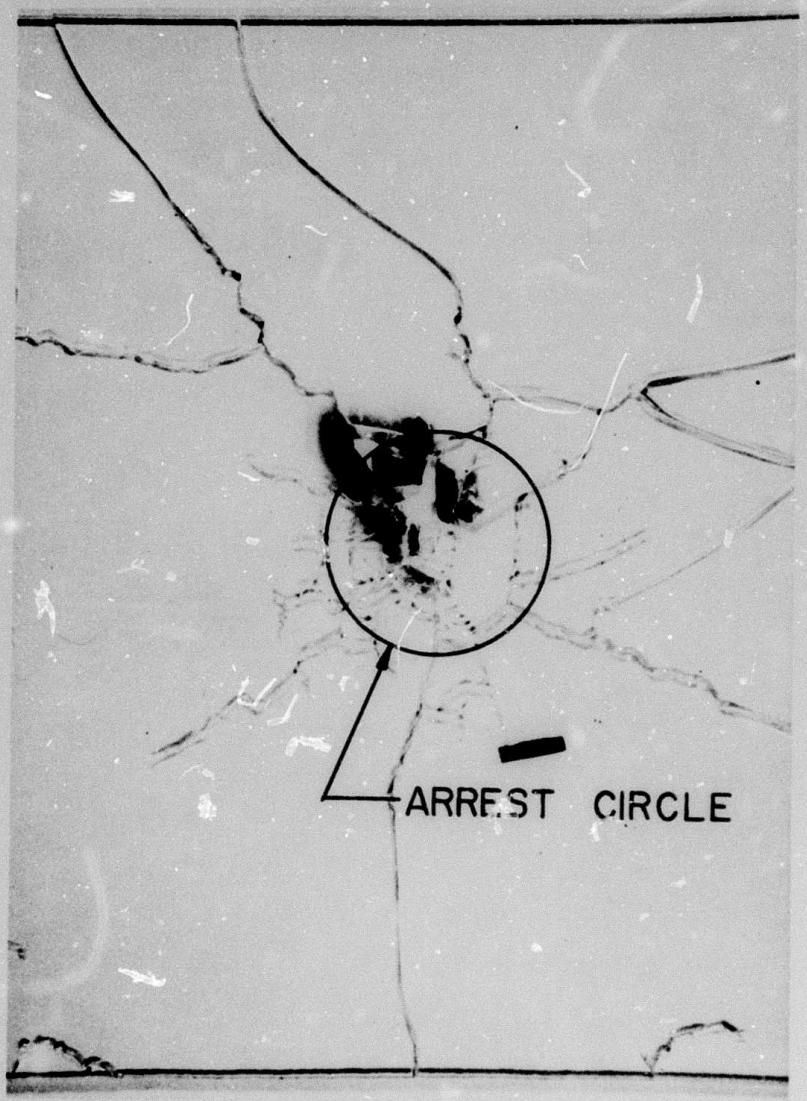

Fig. 2.4 Photograph at the Final Crack Pattern in Model H-11

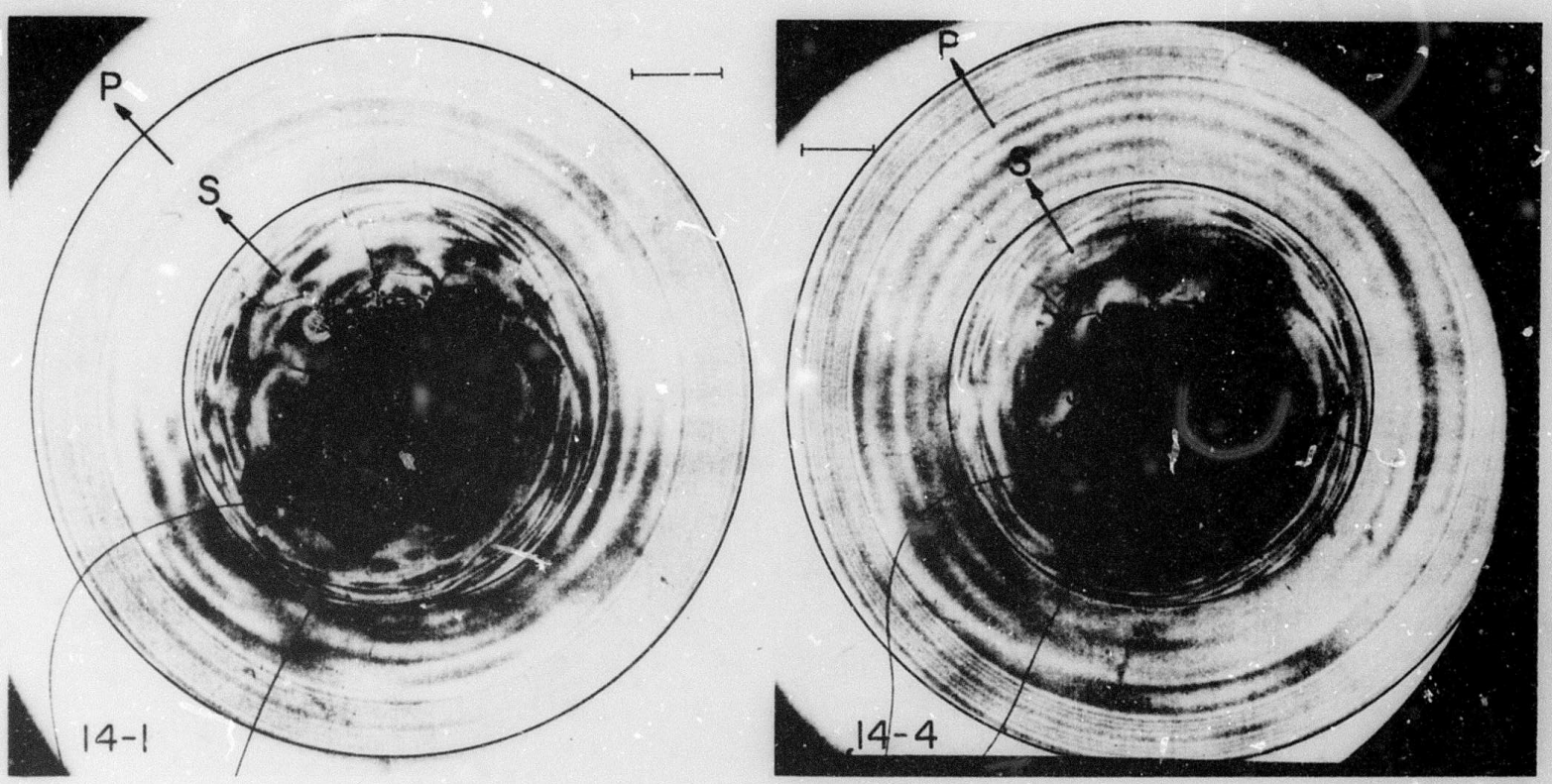

Fig. 2.5.1 Photoelastic and Dynamic Crack Patterns in an Entire Plane (Early Event)

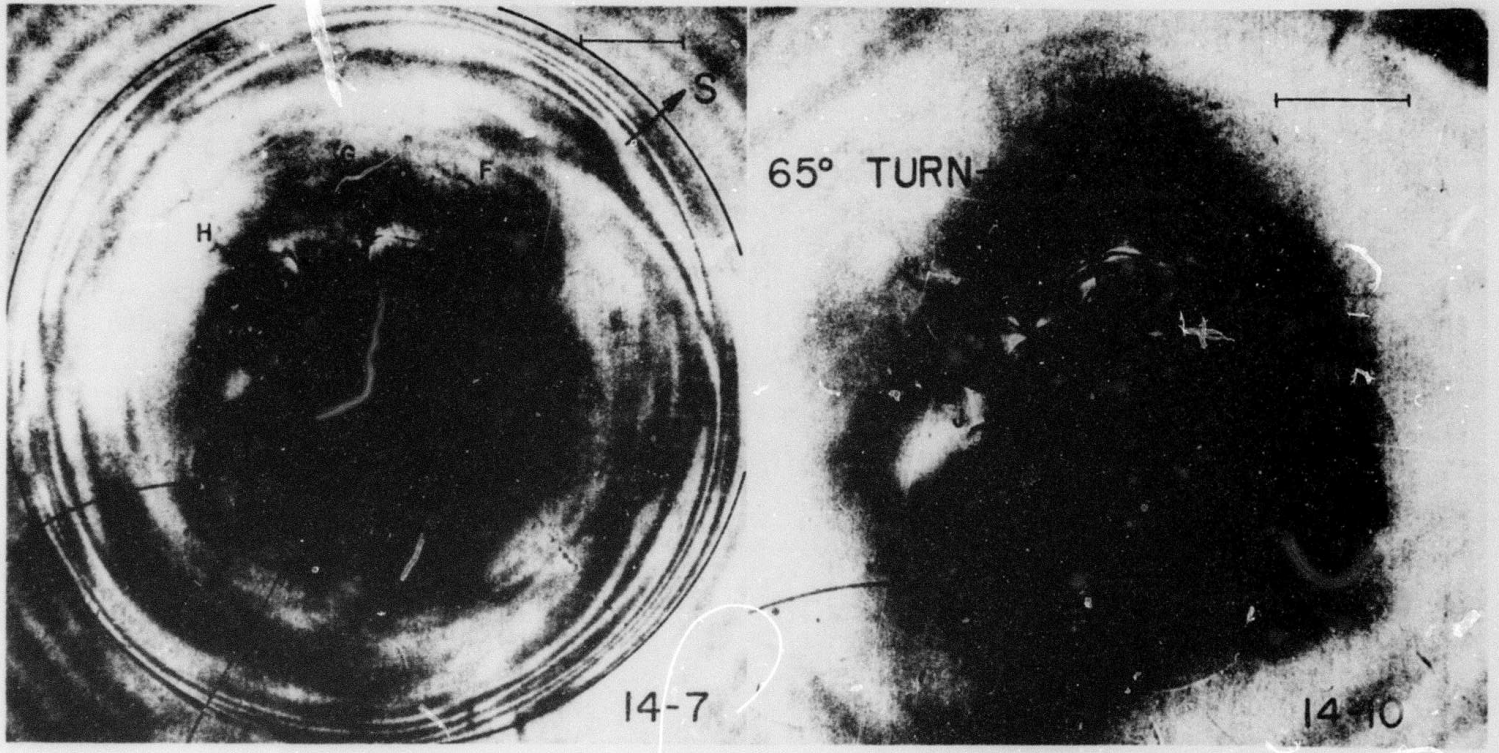

Fig. 2.5.2 Photoelastic and Dynamic Crack Patterns in an Entire Plane (Long Crack Development)

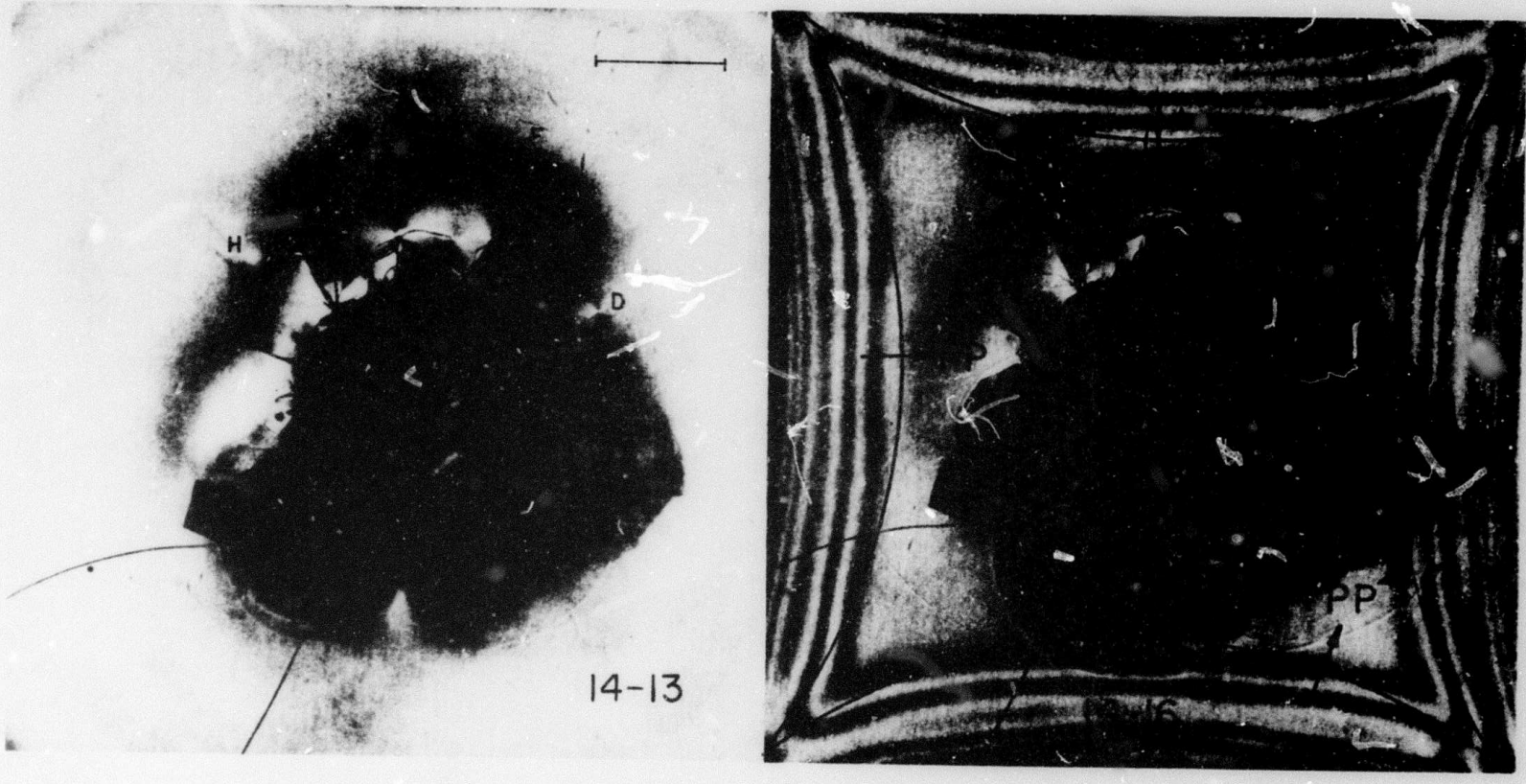

Fig. 2.5.3 Photoelastic and Dynamic Crack Patterns in an Entire Plane (Crack Arrest)

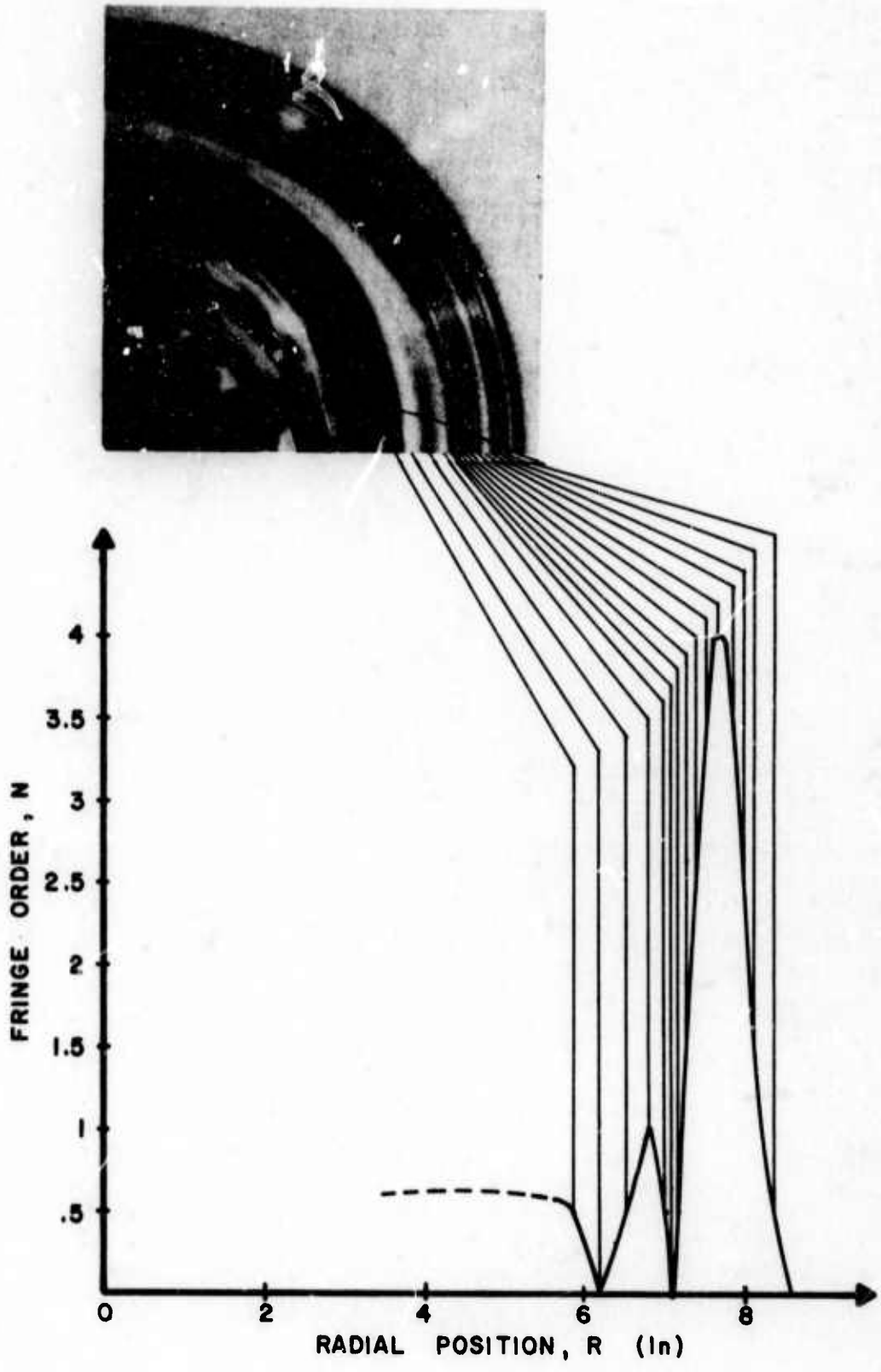

Fig. 2.6 Profile of the Outgoing Dilatational Wave

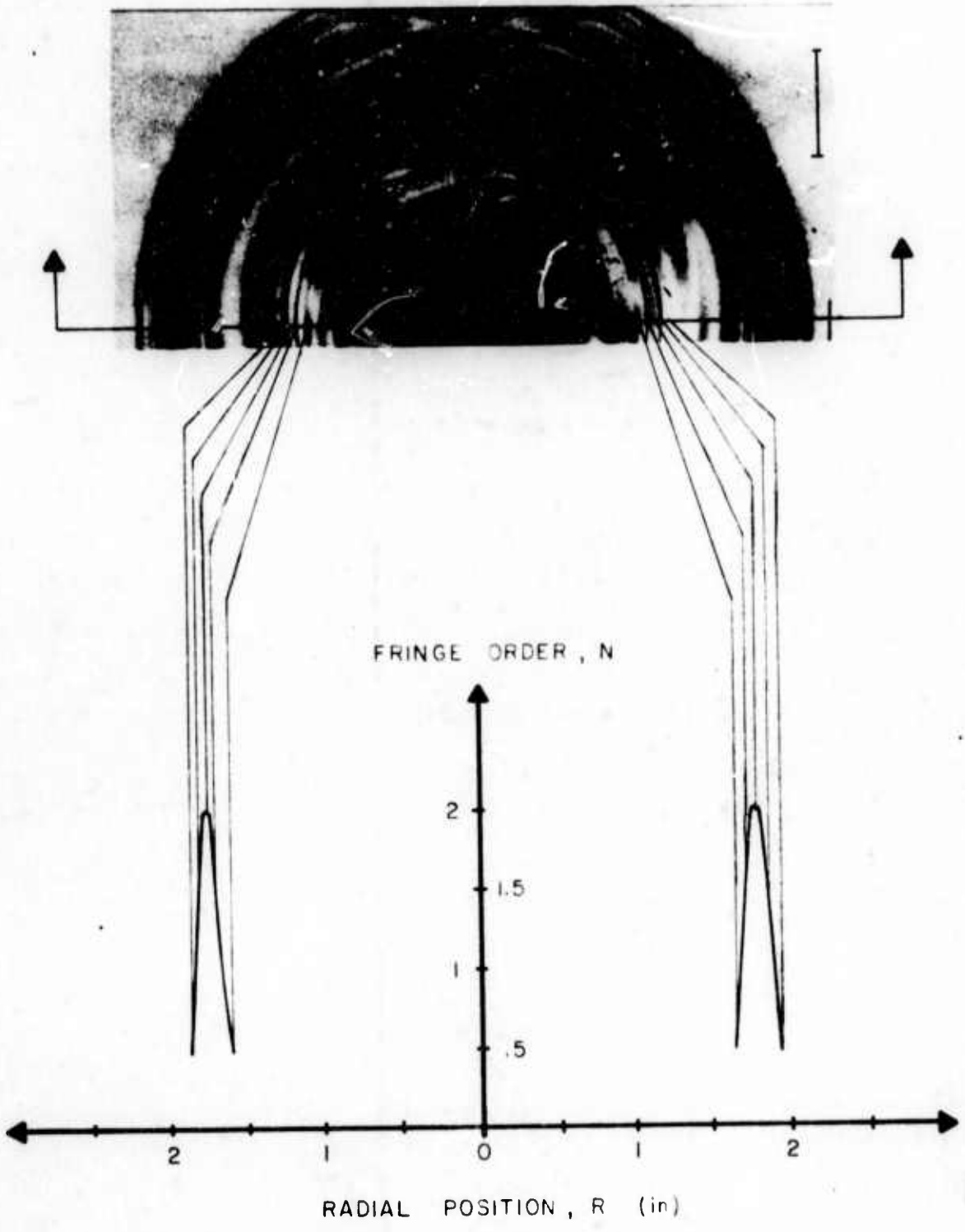

Fig. 2.7 Profile of the Outgoing Shear Wave

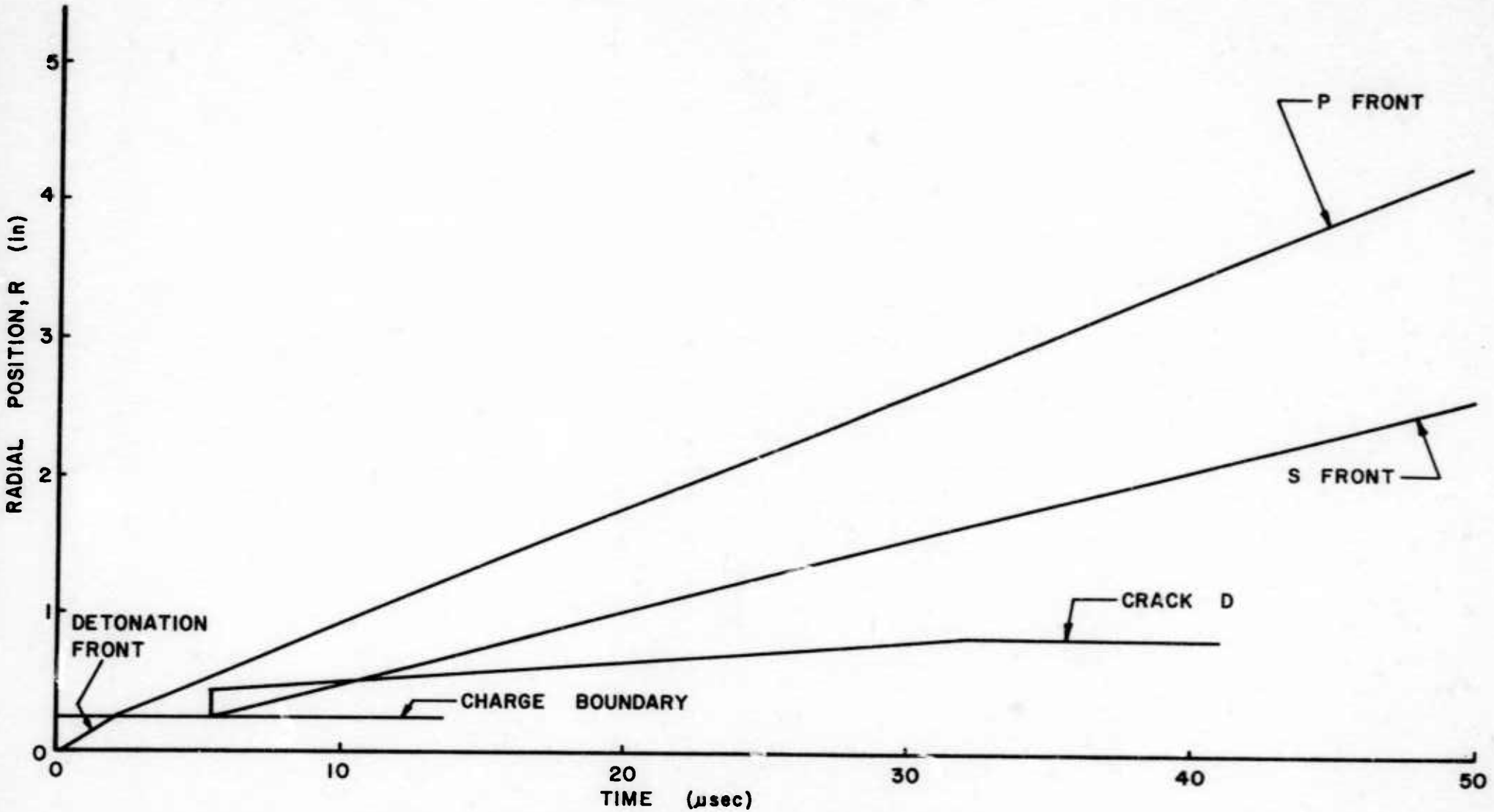

Fig. 2.8 Radial Position of the Crack Fronts, P Wave and S Wave Fronts as a Function of Time. H-7 Model

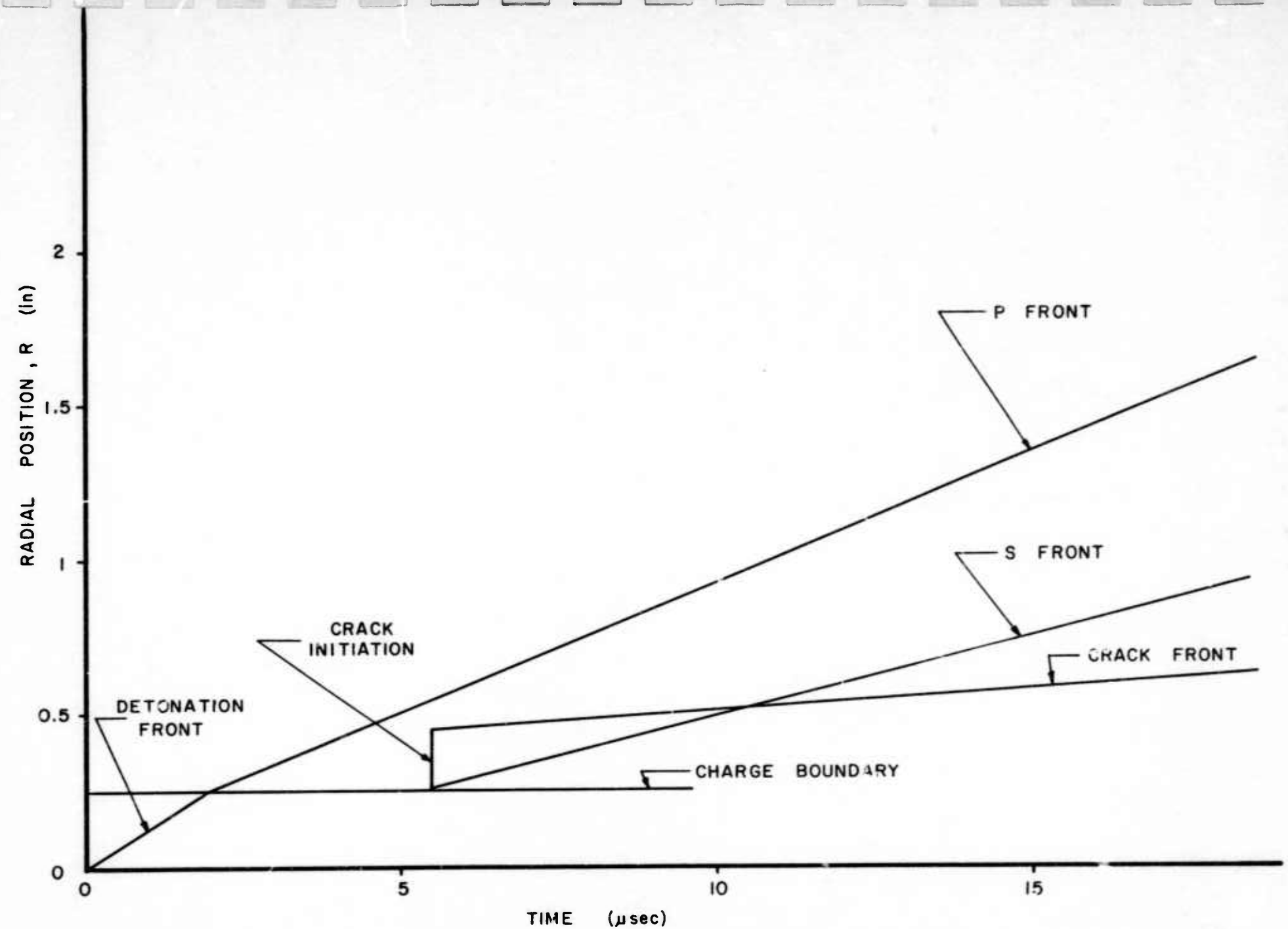

Fig. 2.9 Expanded View of the Radial Positions of the Crack Fronts and the P and S Fronts During the Early Event

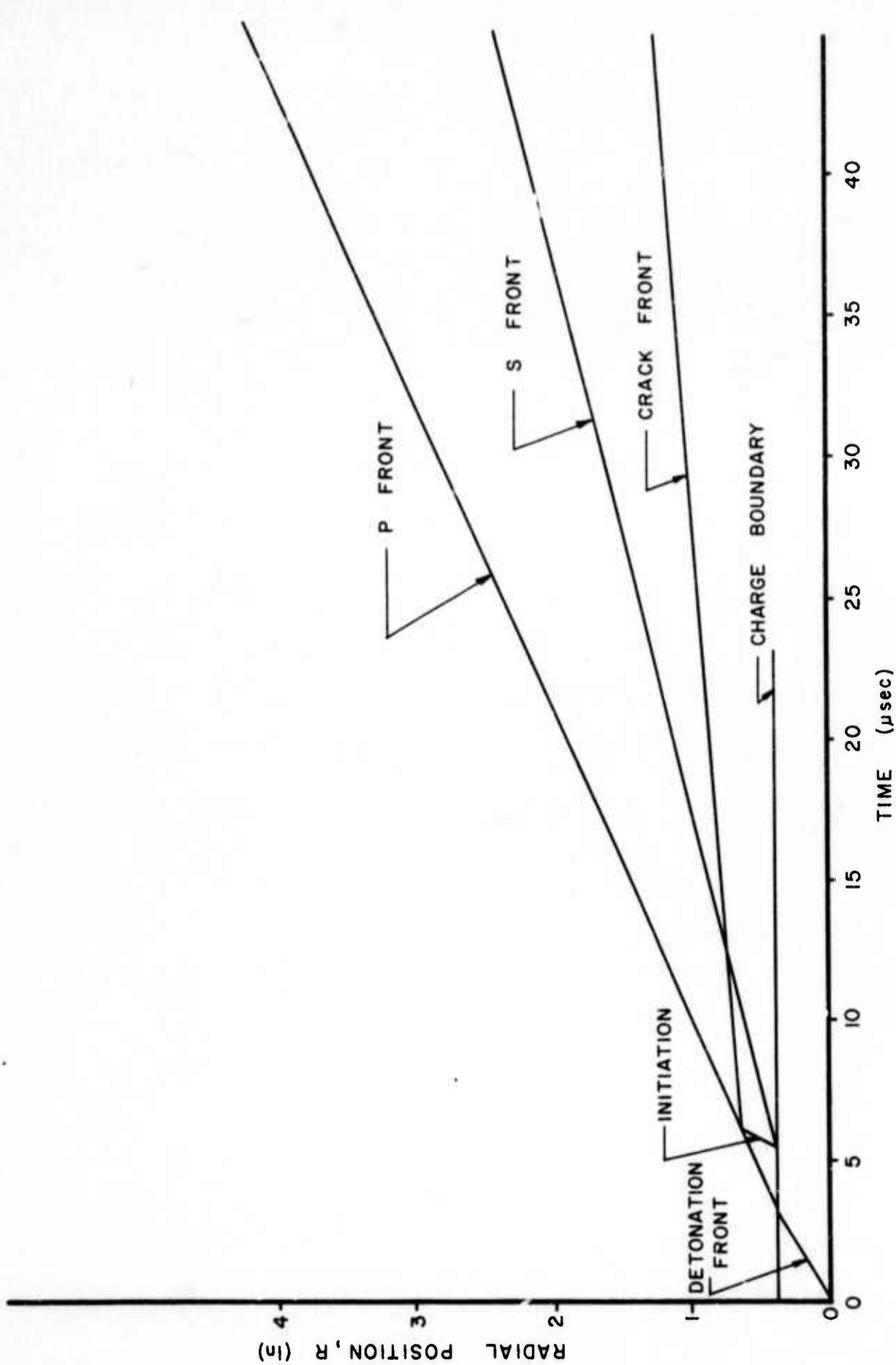

Fig. 2.10 Radial Position of the Crack Fronts, P Wave and S Wave Fronts as a Function of Time. H-11 Model

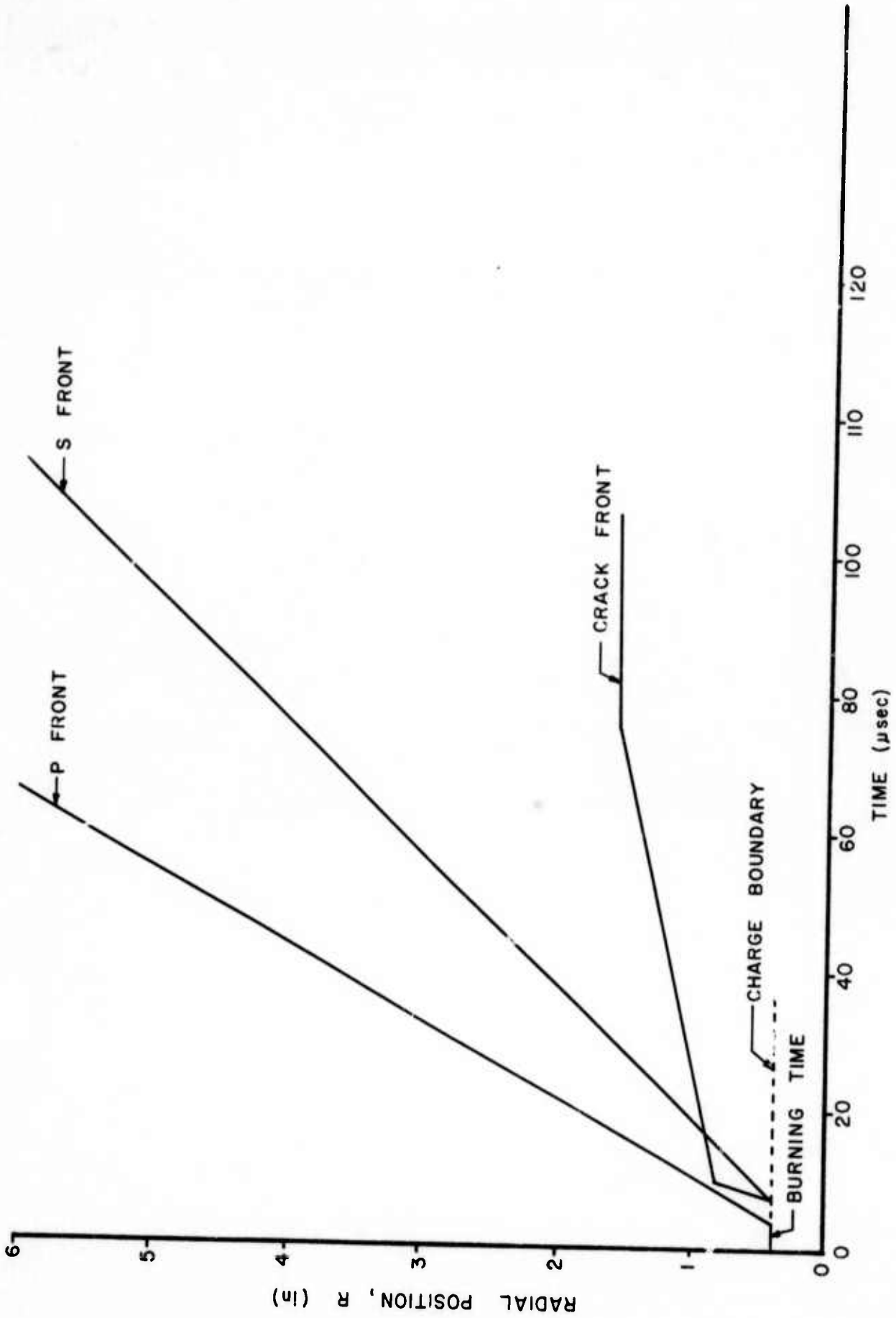

Fig. 2.11 Radial Position of the Crack Fronts, P Wave and S Wave Fronts as a Function of Time. H-14 Model

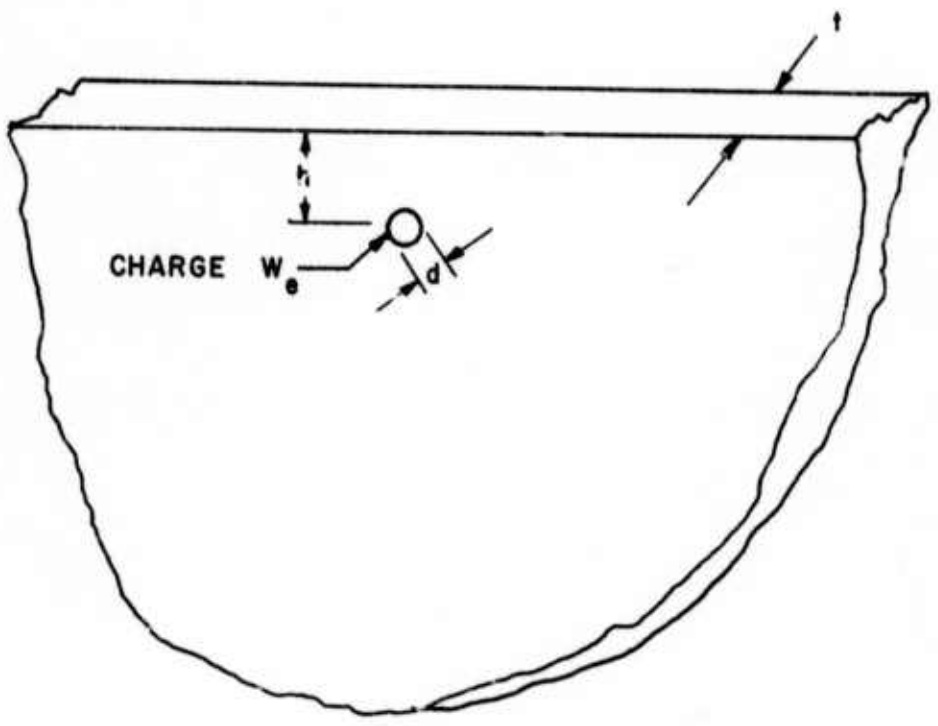

Fig. 3.1 Half Plane Model With Lead Azide Charge

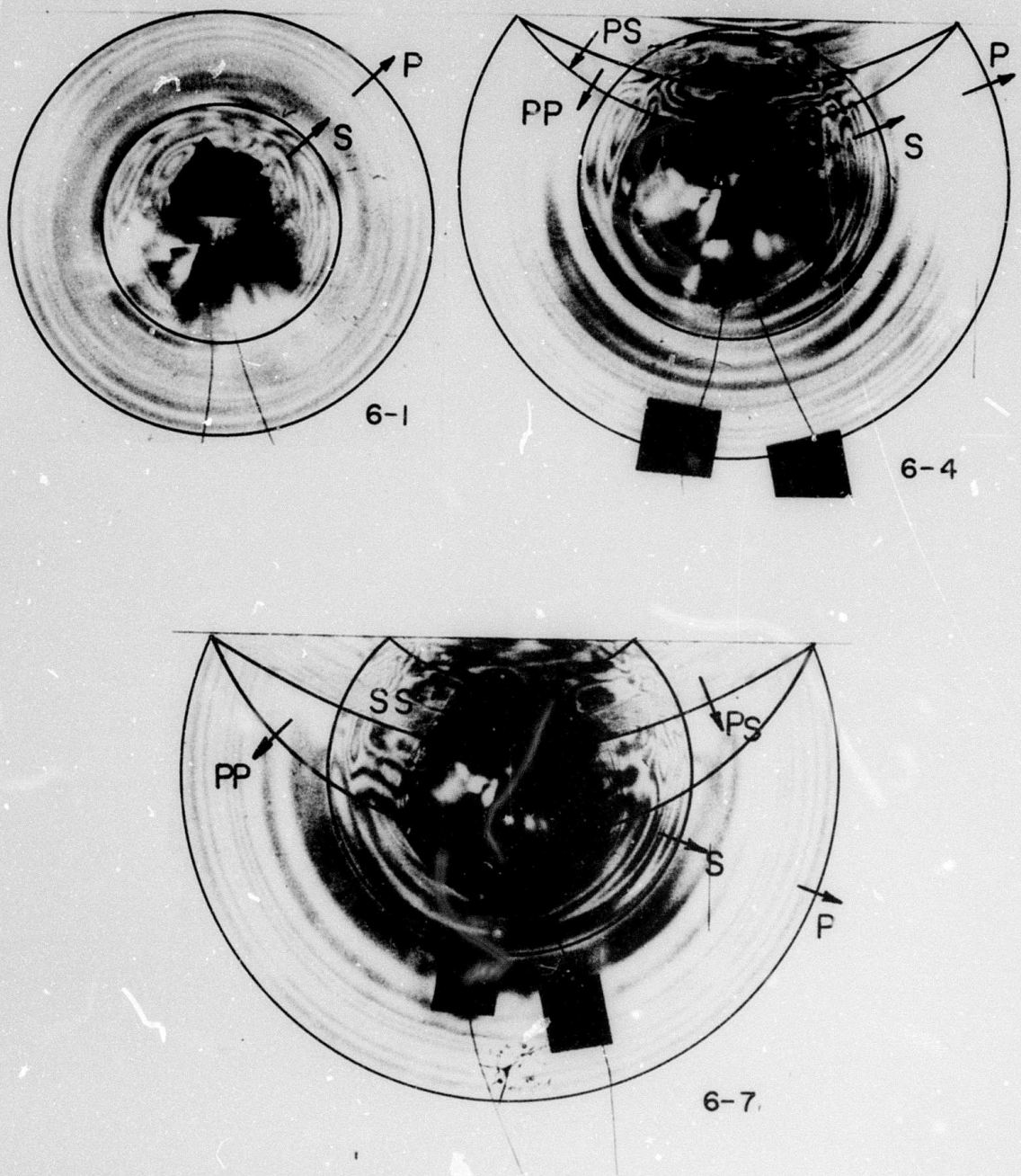

Fig. 3.2.1 Stress Wave Reflections From a Dilatational Source in a Half Plane. Model H-6

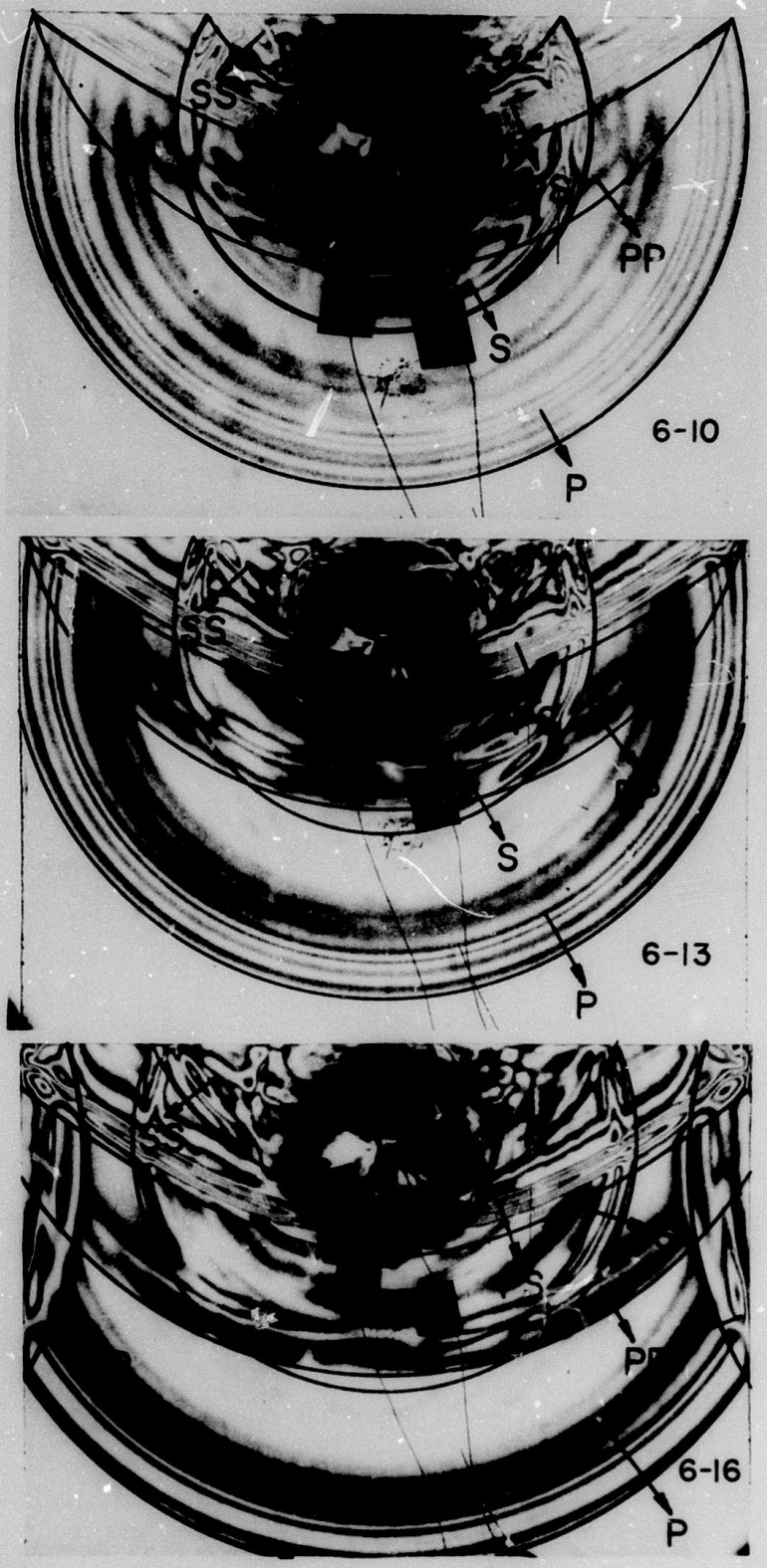

Fig. 3.2.2 Stress Wave Reflections From a Dilatational Source in a Half Plane. Model H-6

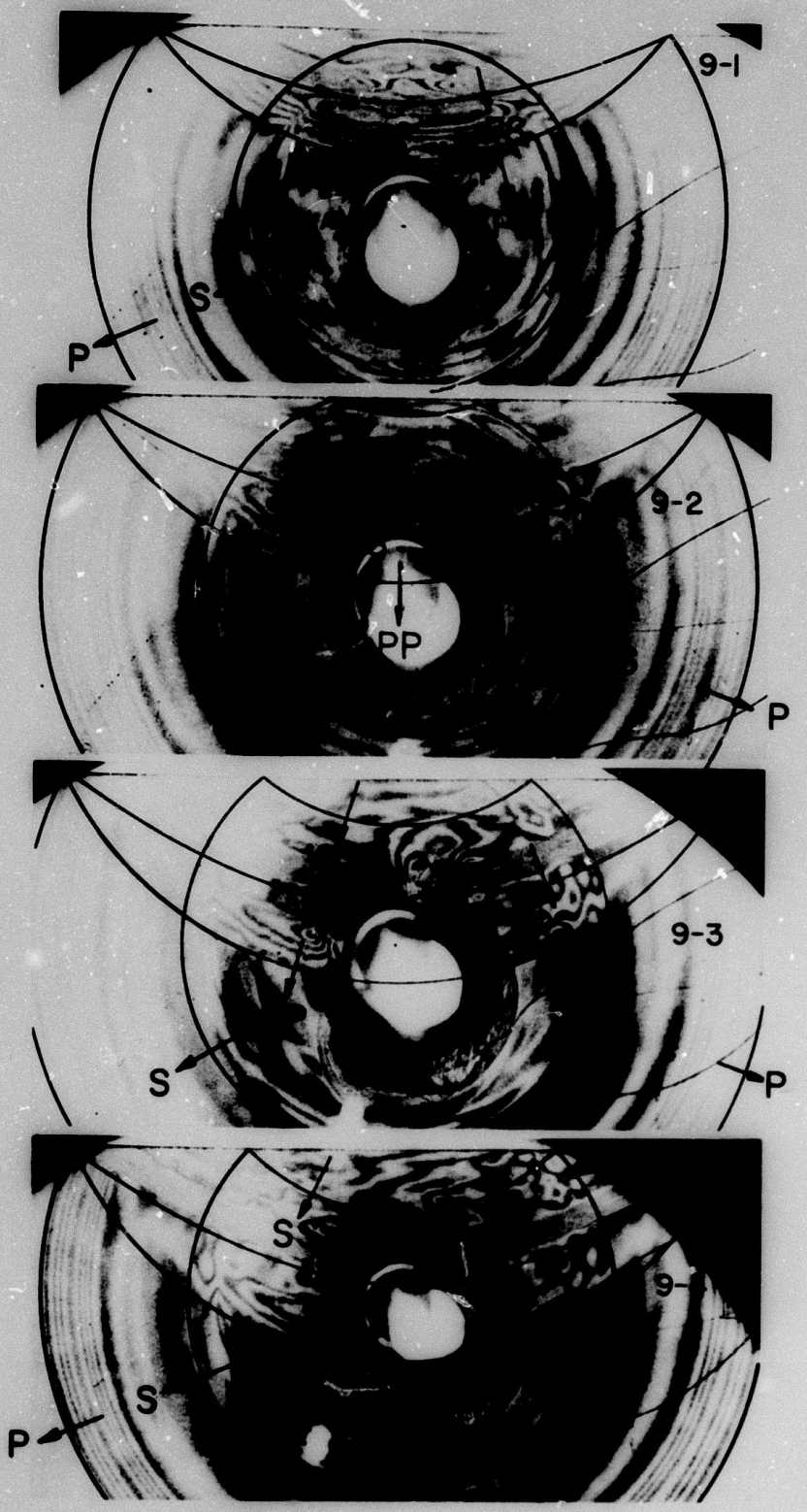

Fig. 3.3.1 Stress Wave Reflections From a Dilatational Source in a Half Plane. Model H-9

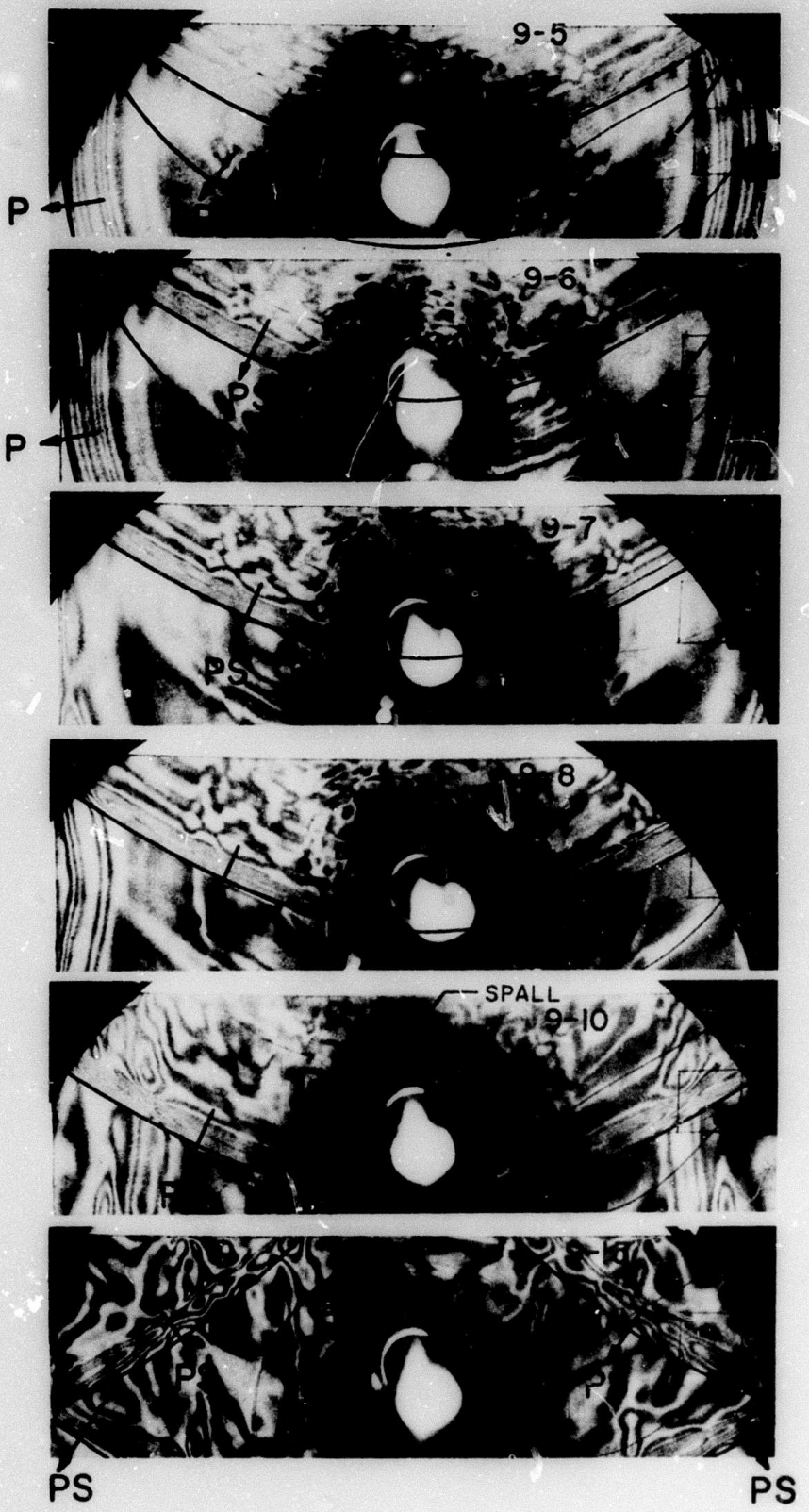

Fig. 3.3.2 Stress Wave Reflections From a Dilatational Source in a Half Plane. Model H-9

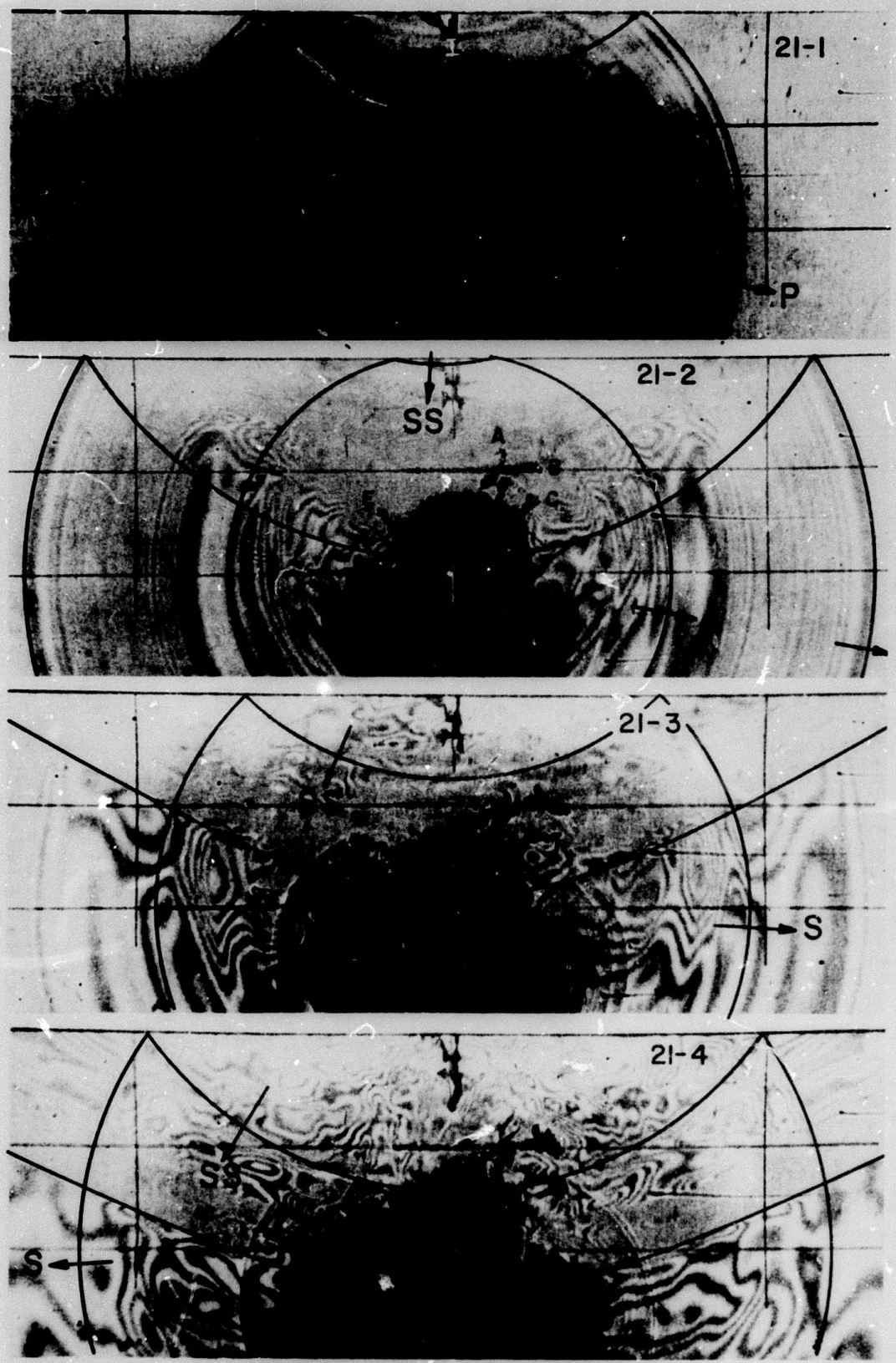

Fig. 3.4.1 Stress Wave Reflections From a Dilatational Source in a Half Plane. Model H-21

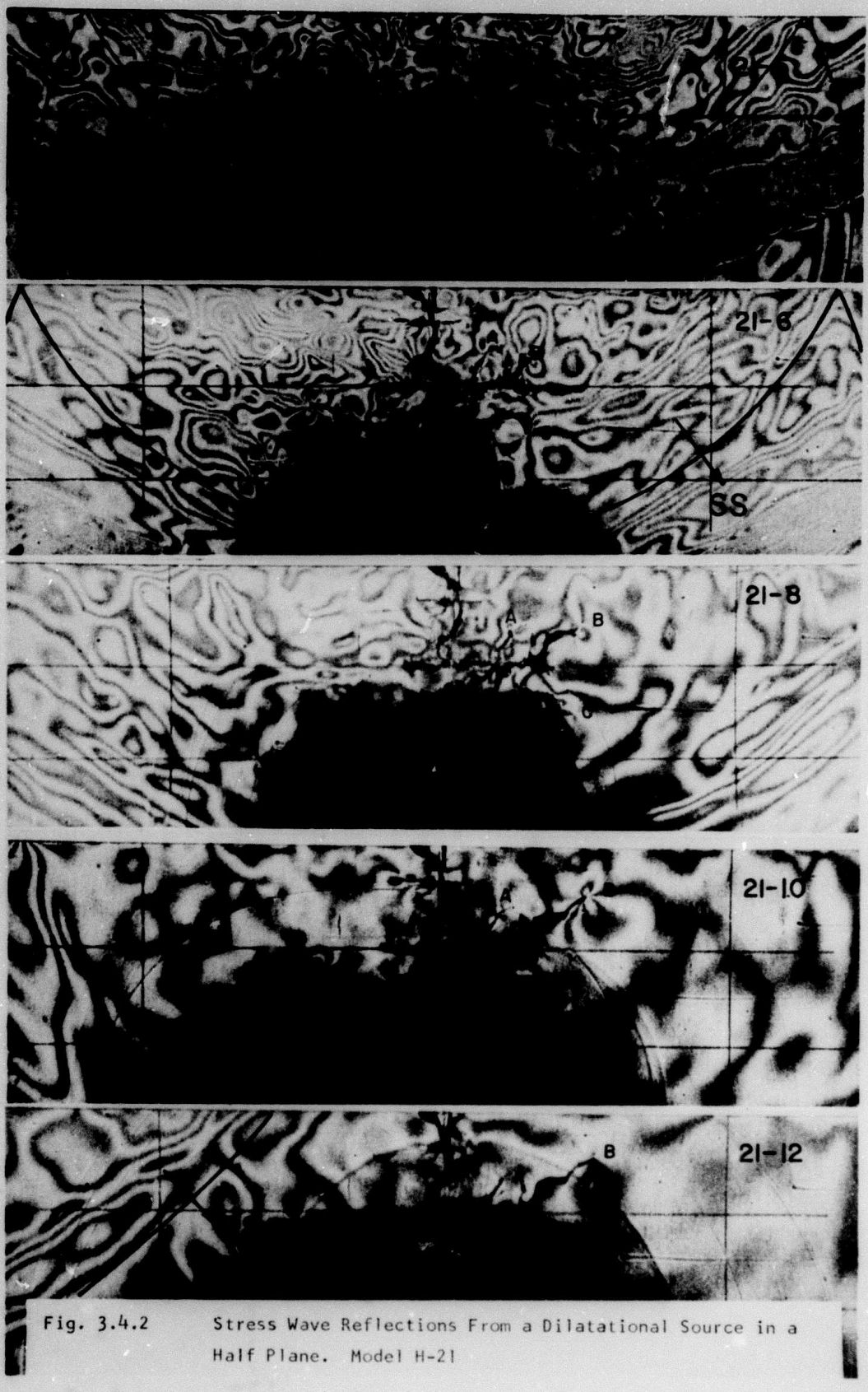

Fig. 3.4.2 Stress Wave Reflections From a Dilatational Source in a Half Plane. Model H-21

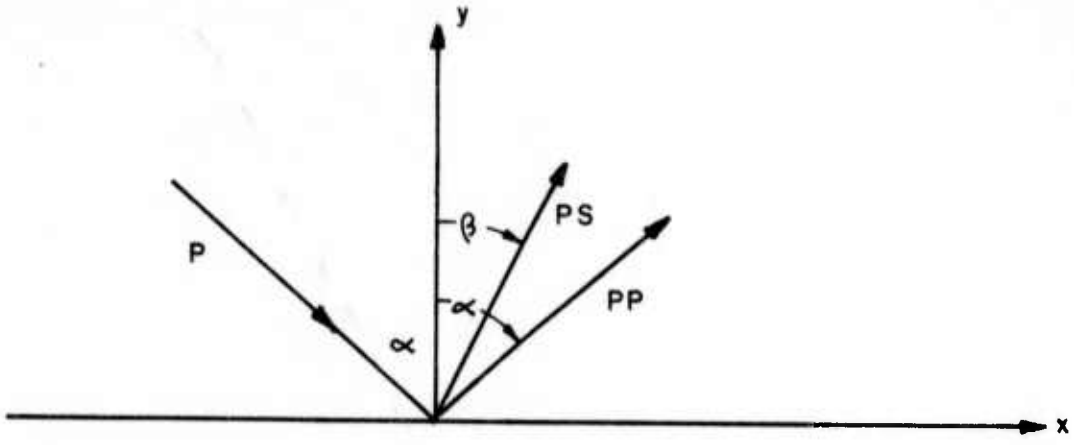

Fig. 3.5.1 Reflection of a Plane Dilatational Wave at a Free Boundary

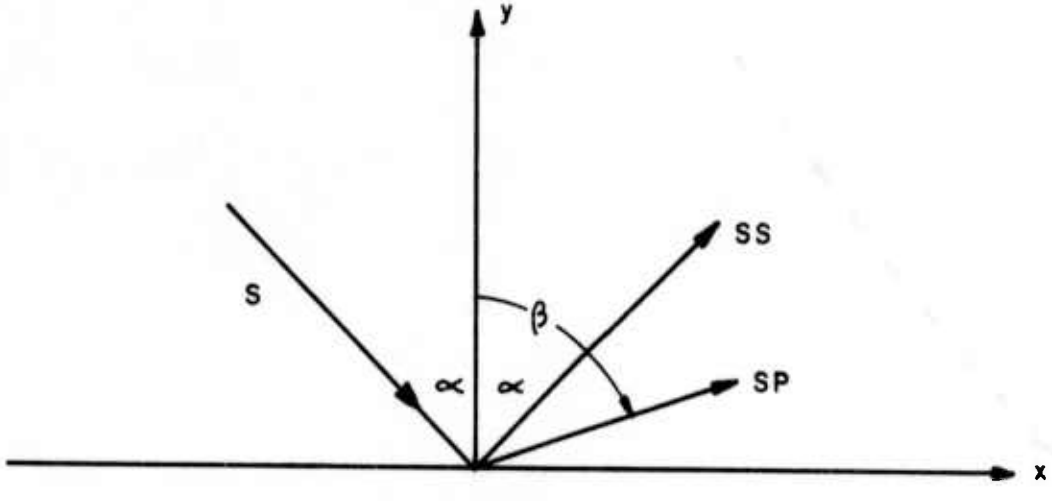

Fig. 3.5.2 Reflection of a Plane Shear Wave at a Free Boundary

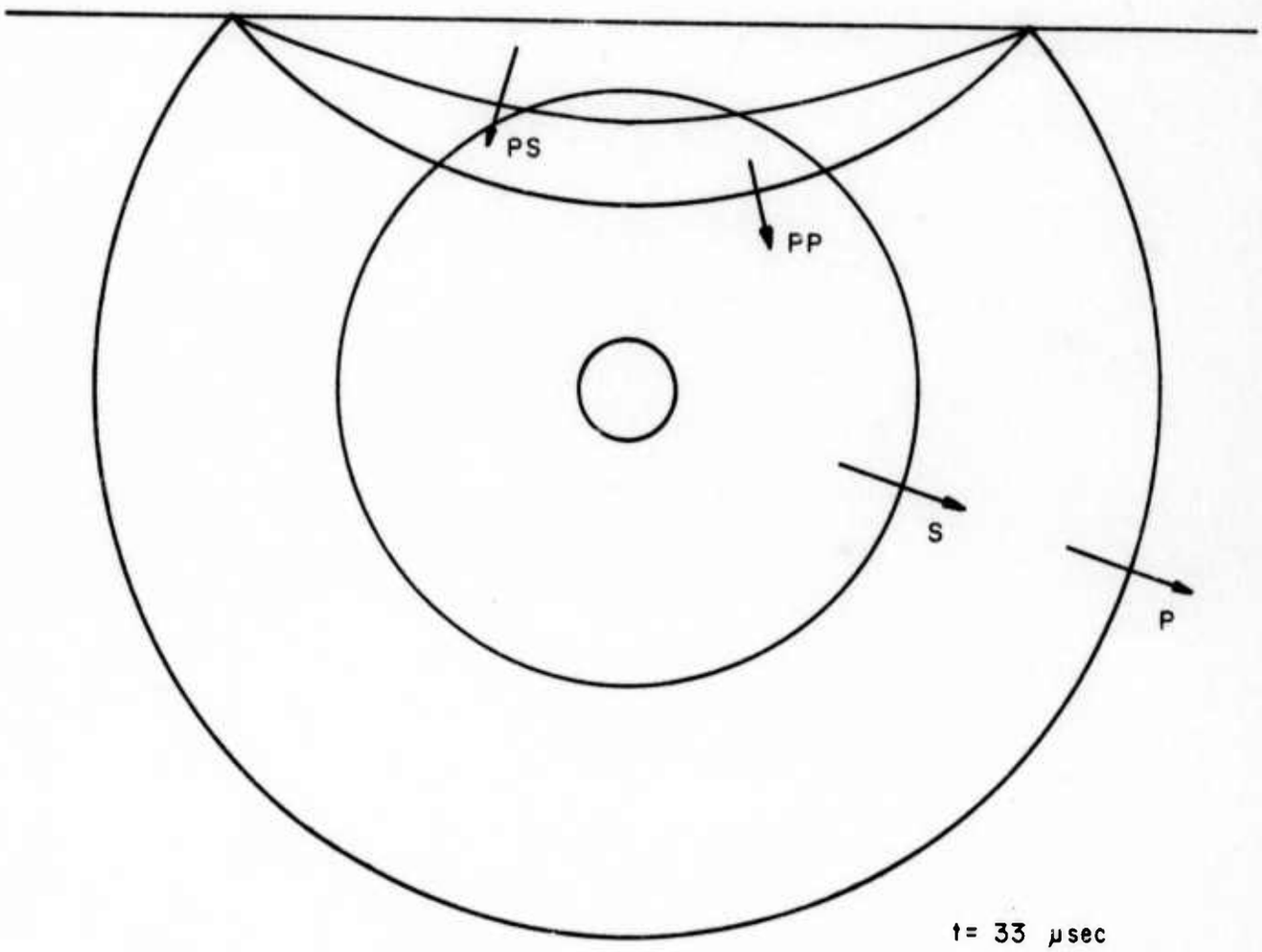

Fig. 3.6 Wave Fronts Associated with the Incident P and S Waves and Reflected PP and PS Waves

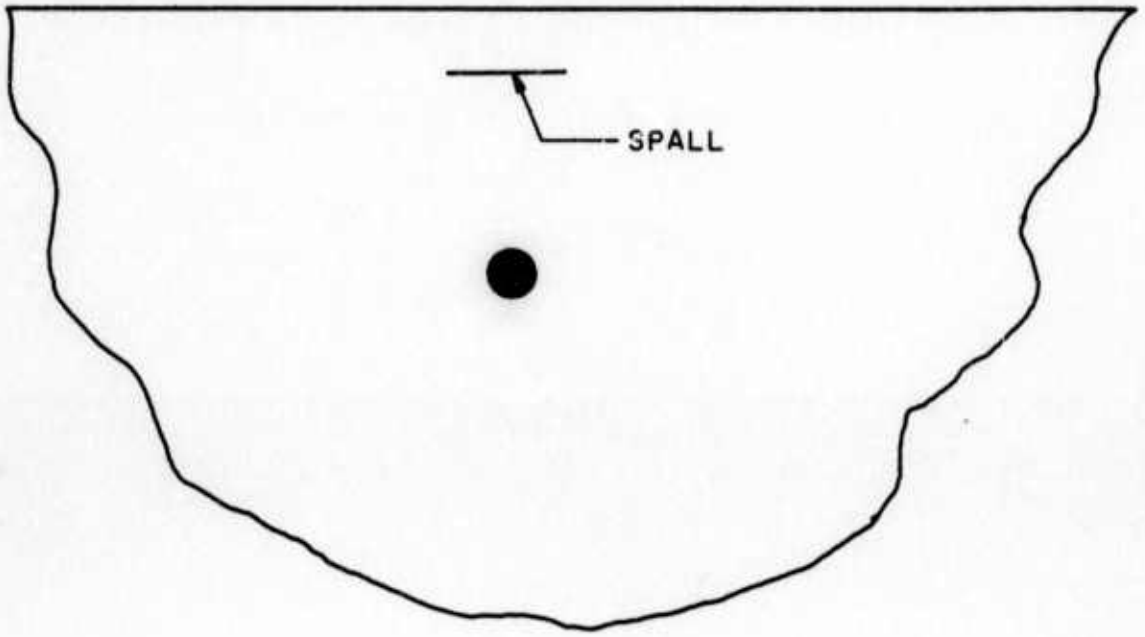

Fig. 3.7 Illustration of a Spall Type Fracture

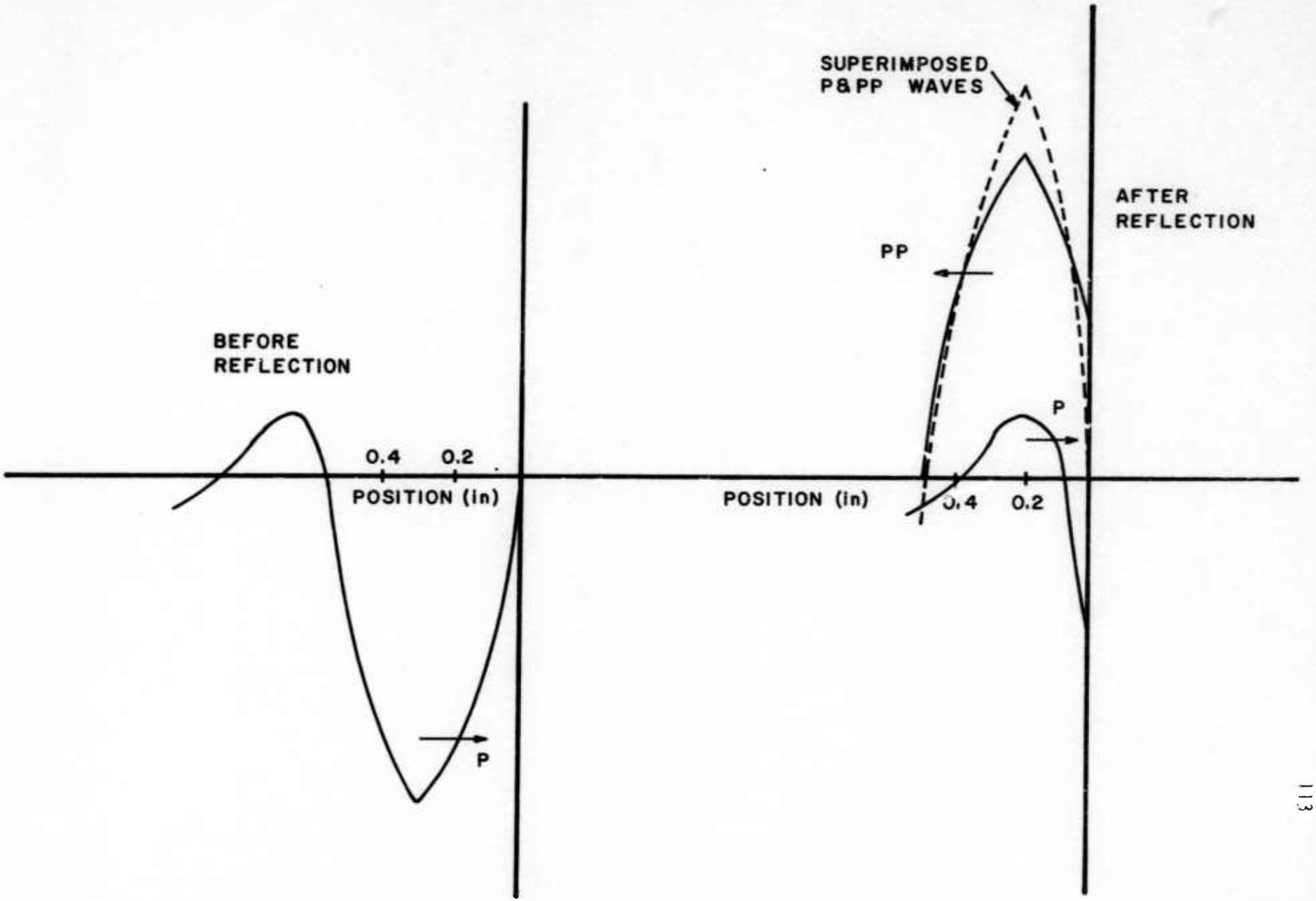

Fig. 3.8 Development of a Tensile Pulse in the Reflection Process

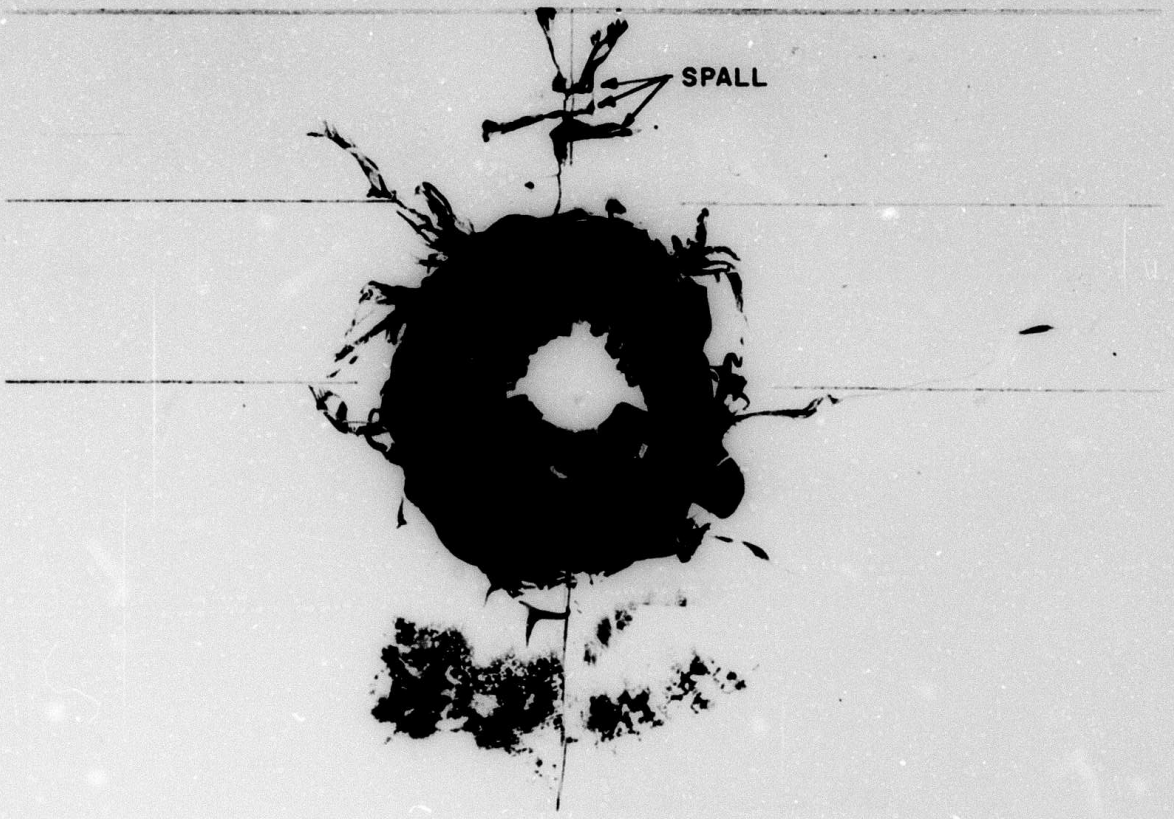

Fig. 3.9 Final Fracture Pattern. Model H-19

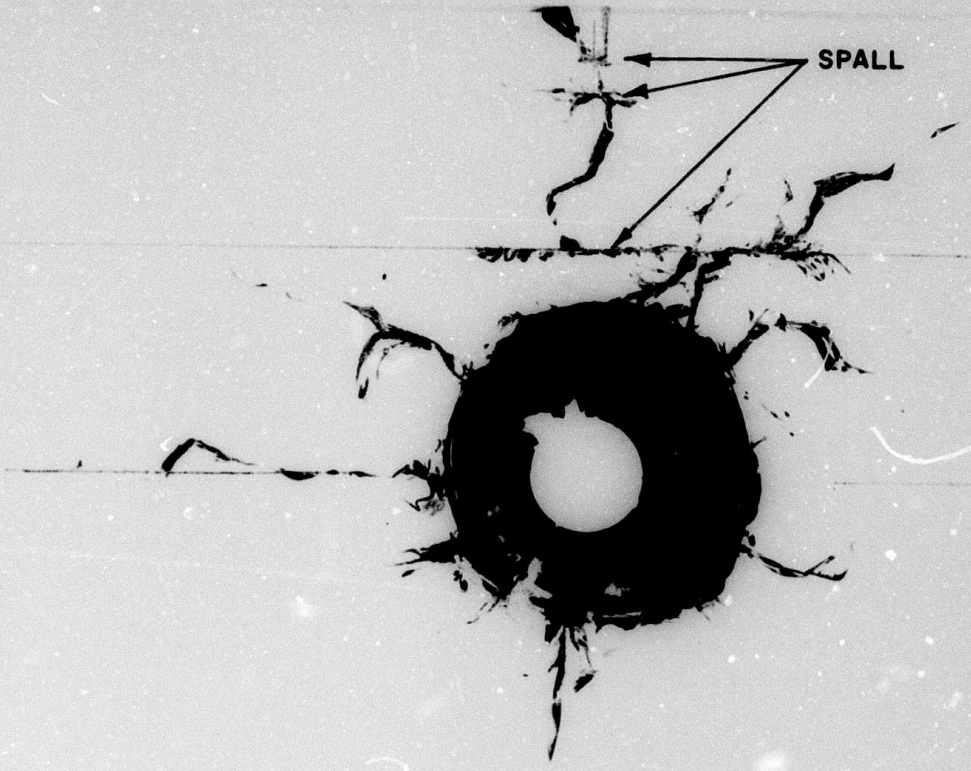

Fig. 3.10 Final Fracture Pattern. Model H-21

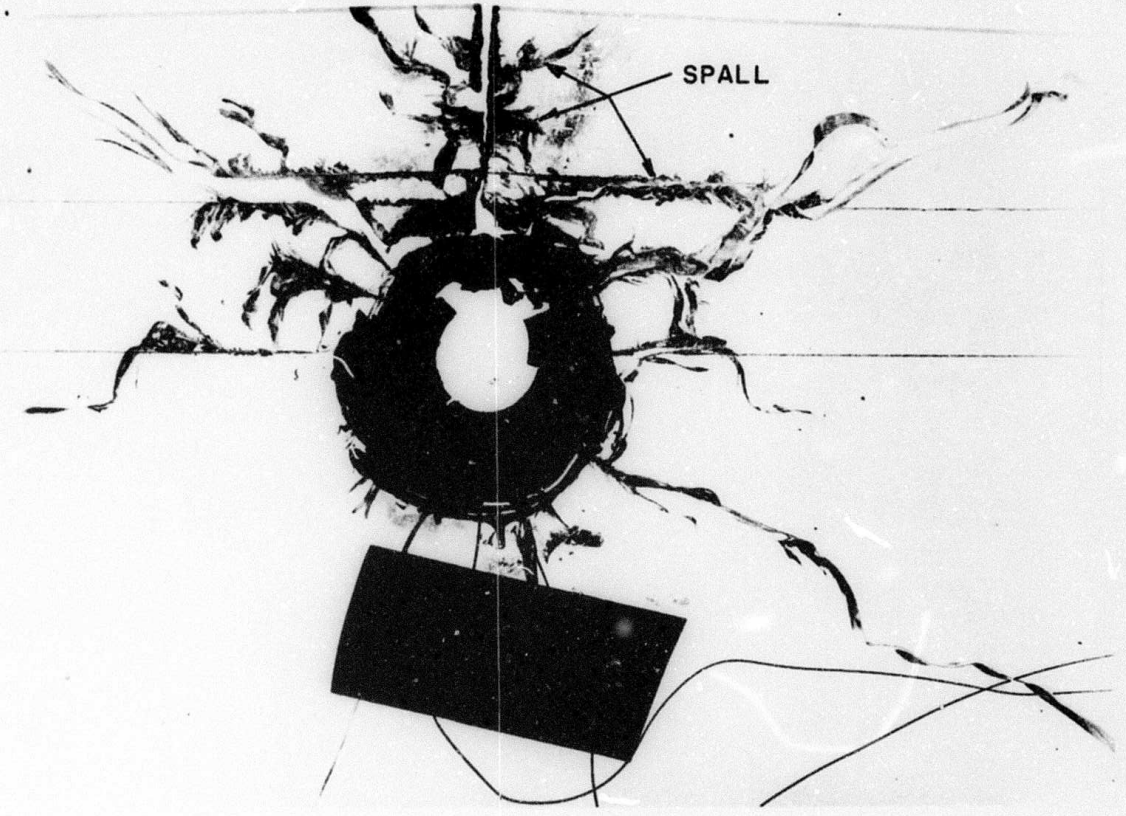

Fig. 3.11 Final Fracture Pattern. Model H-22

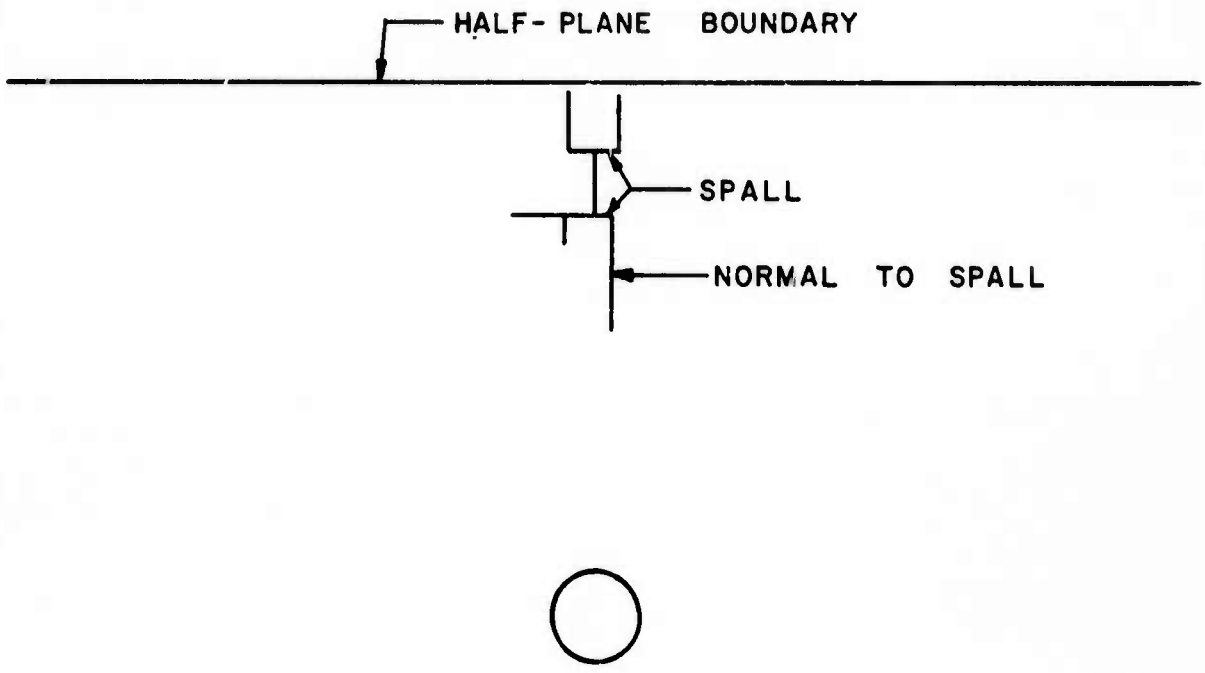

Fig. 3.12 Schematic Drawing Showing Cracking Originating at the Spalls

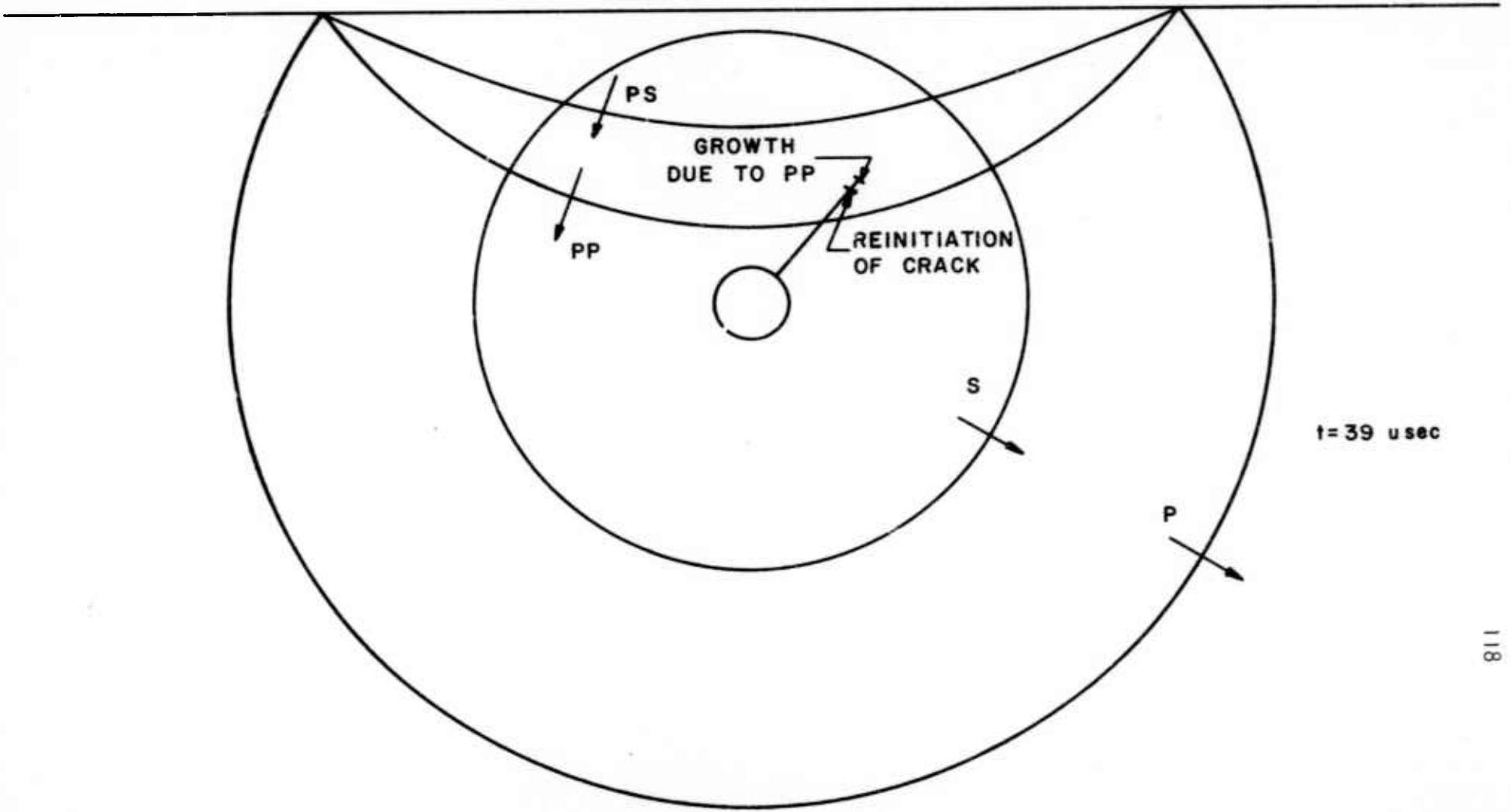

Fig. 3.13 Reinitiation of Crack Due to Action of the PP Wave

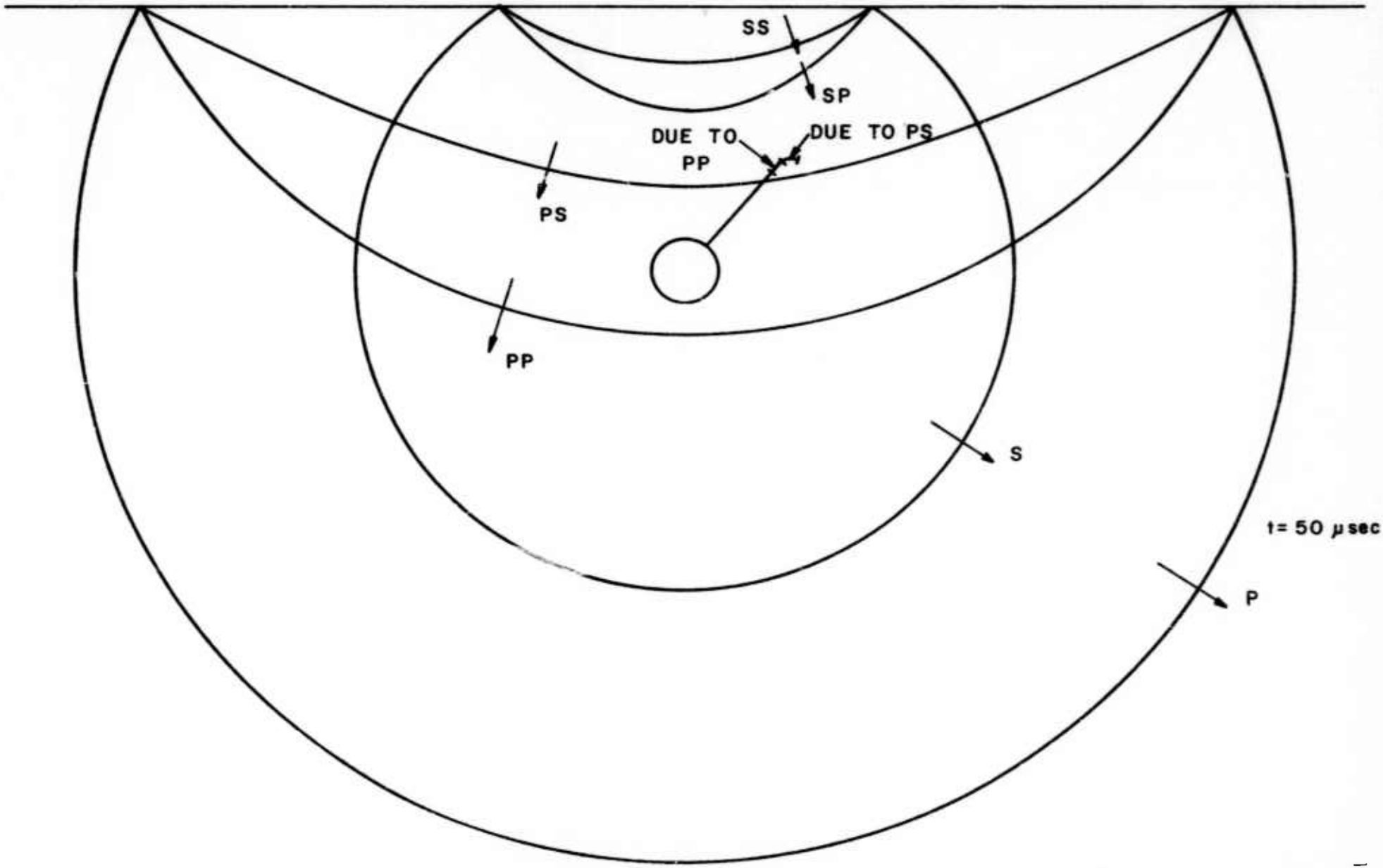

Fig. 3.14 Growth and Turning of Crack Due to Action of the PS Wave

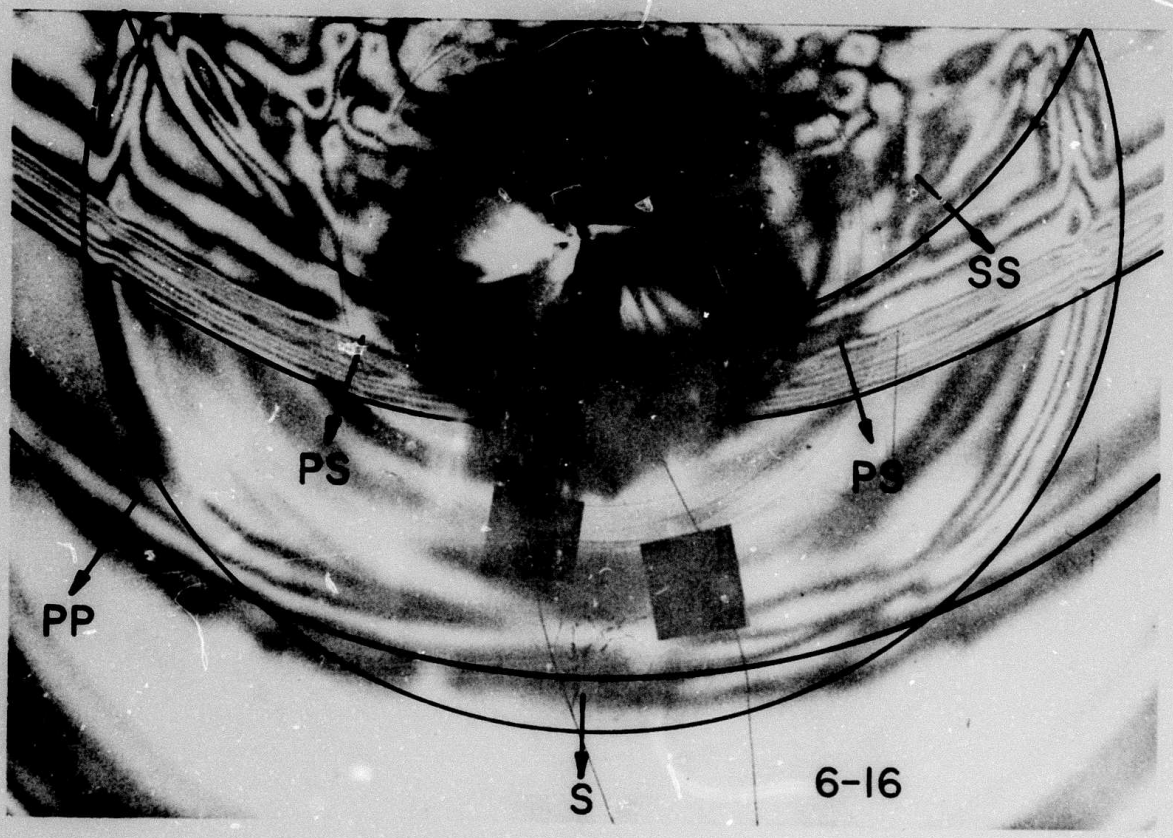

Fig. 3.15 Reflected SS Wave

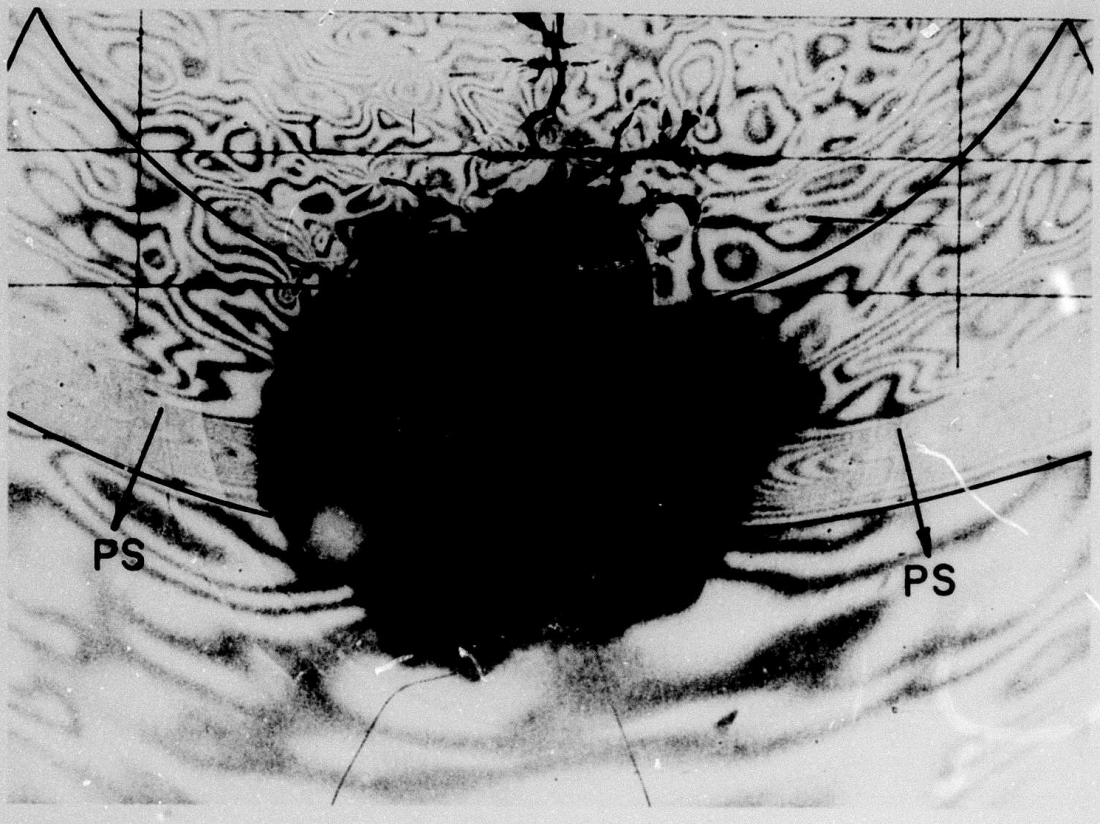

Fig. 3.16 Complex Fringe Pattern in the Fracture Region Late in the Dynamic Event

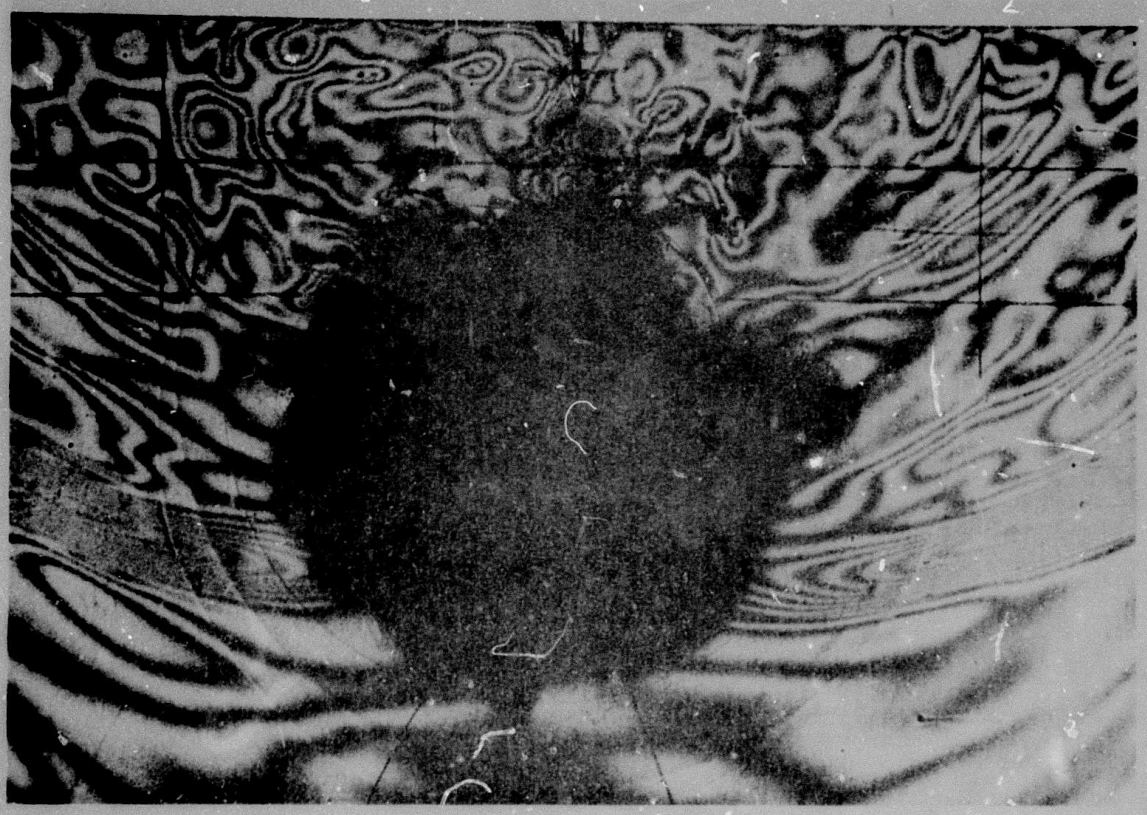

Fig. 3.17 Crack Pattern Producing Break-out

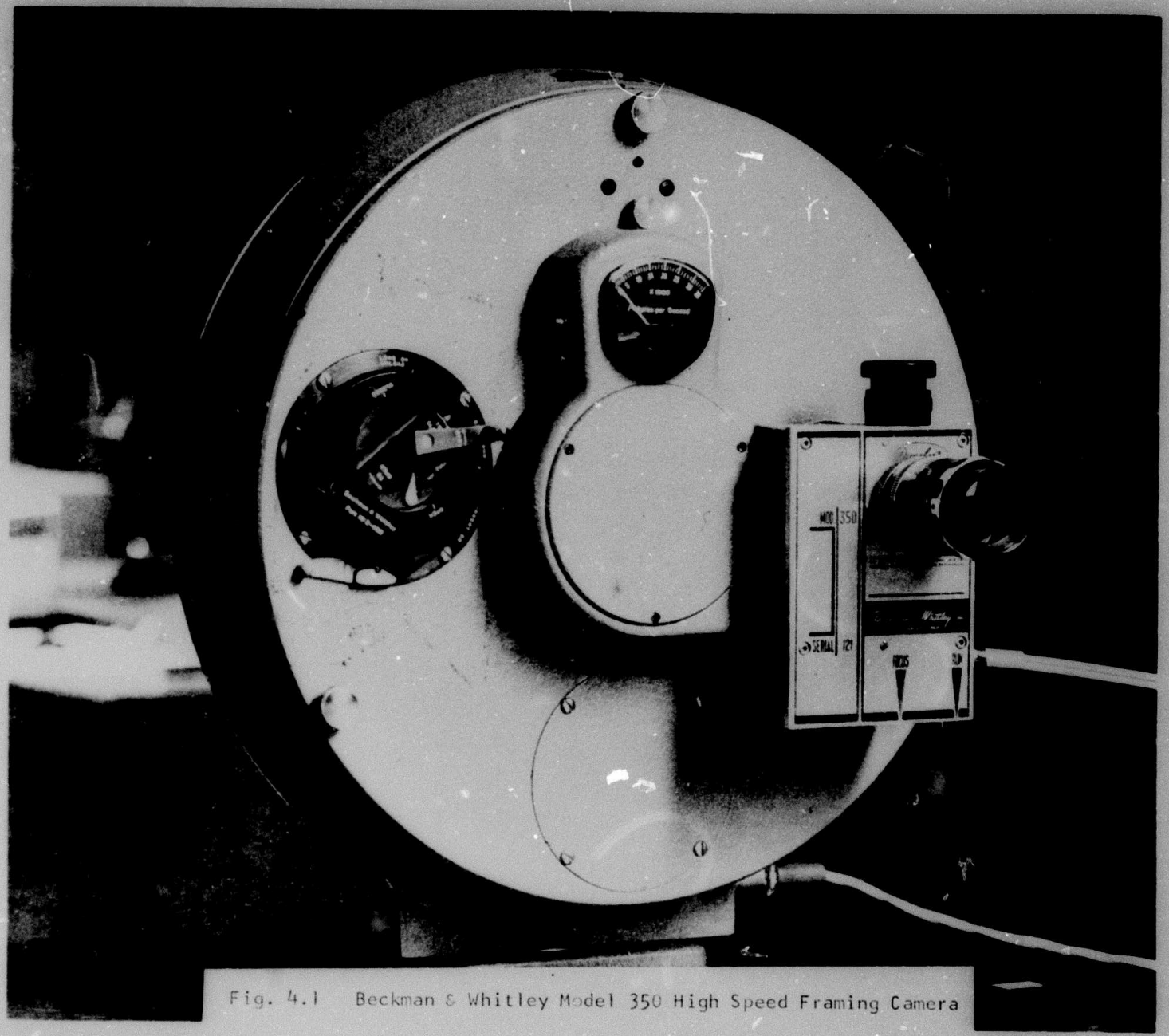

Fig. 4.1 Beckman & Whitley Model 350 High Speed Framing Camera

Fig. 4.2 Charcoal Granite Specimen Located in Protective Box

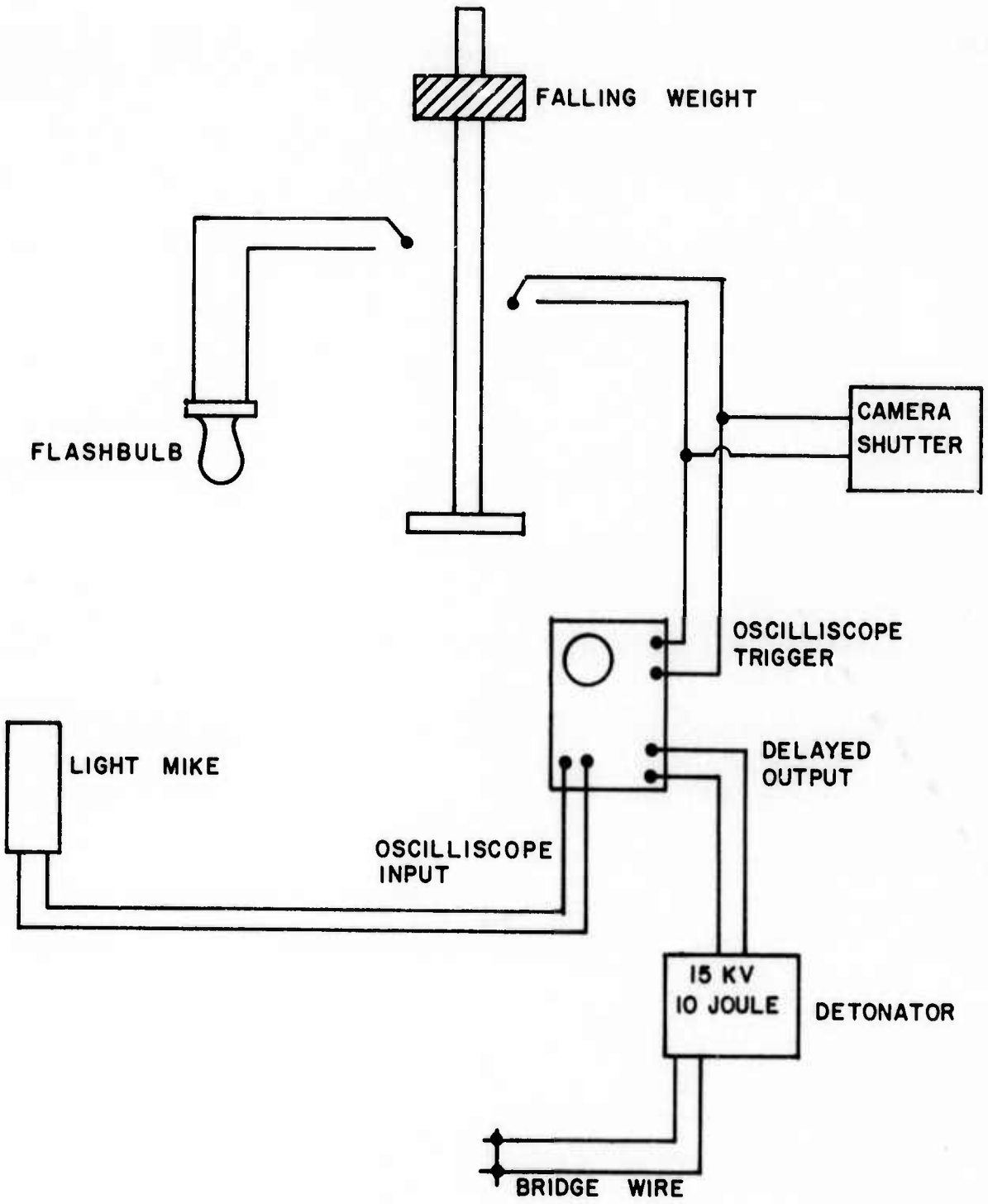

Fig. 4.3 Schematic Diagram of Equipment Utilized in Conducting the Experiment

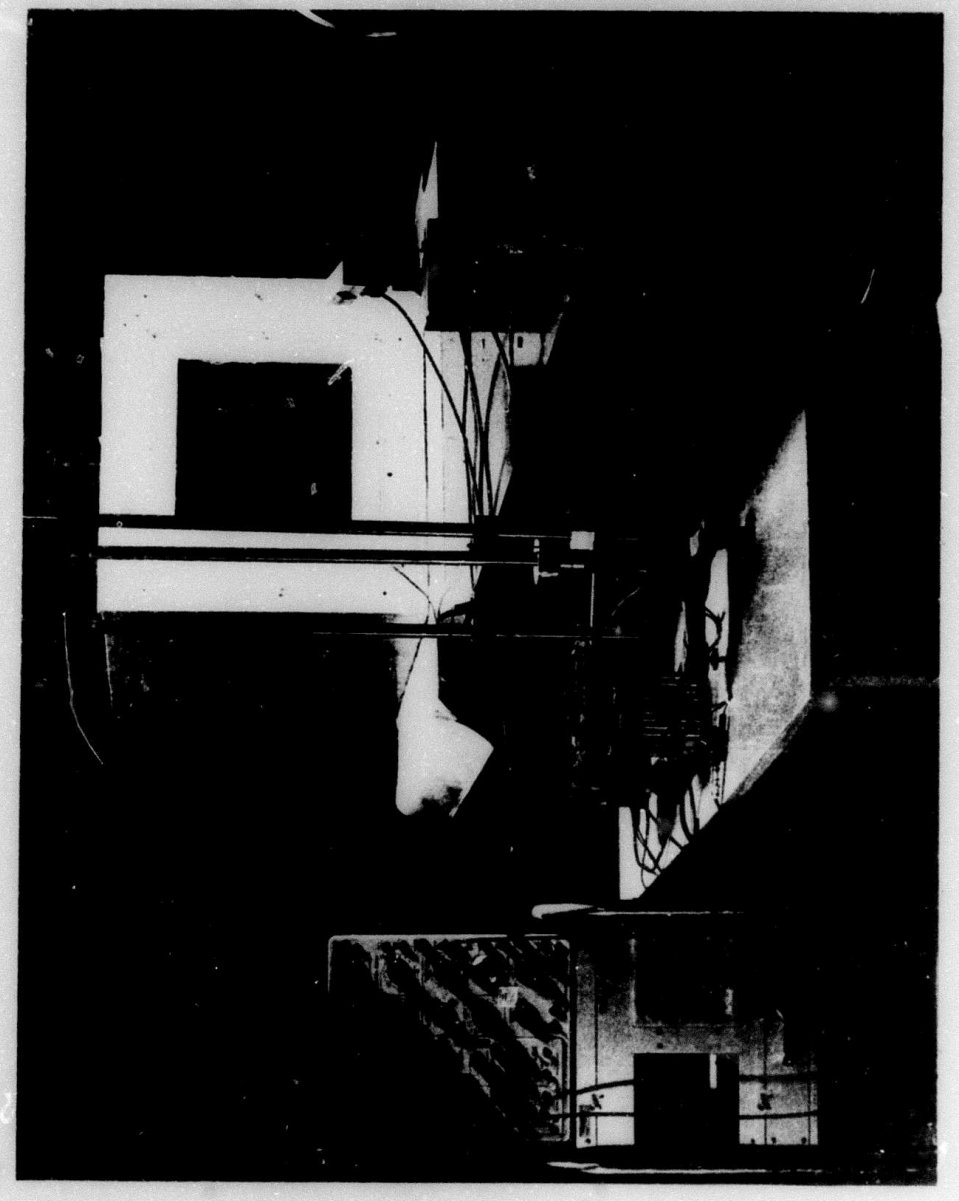

Fig. 4.4 Photograph of Experimental Test Set Up

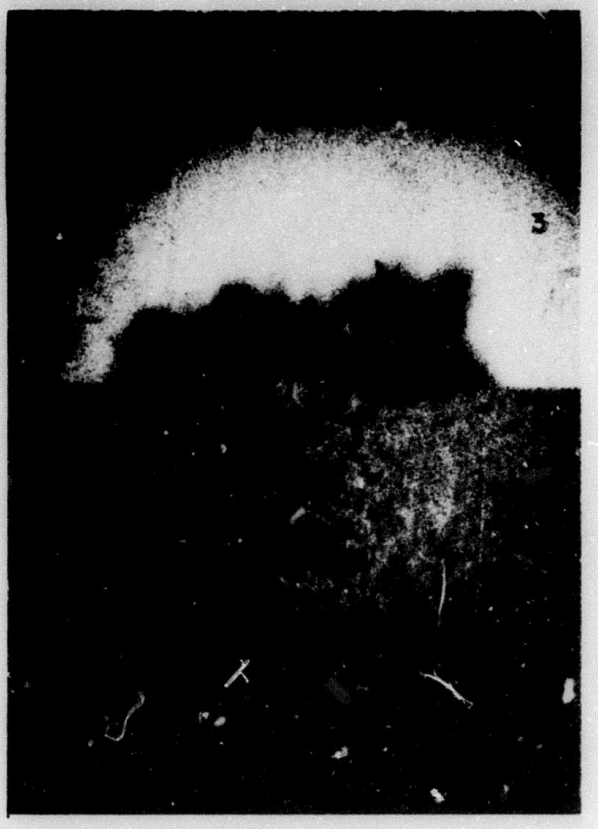

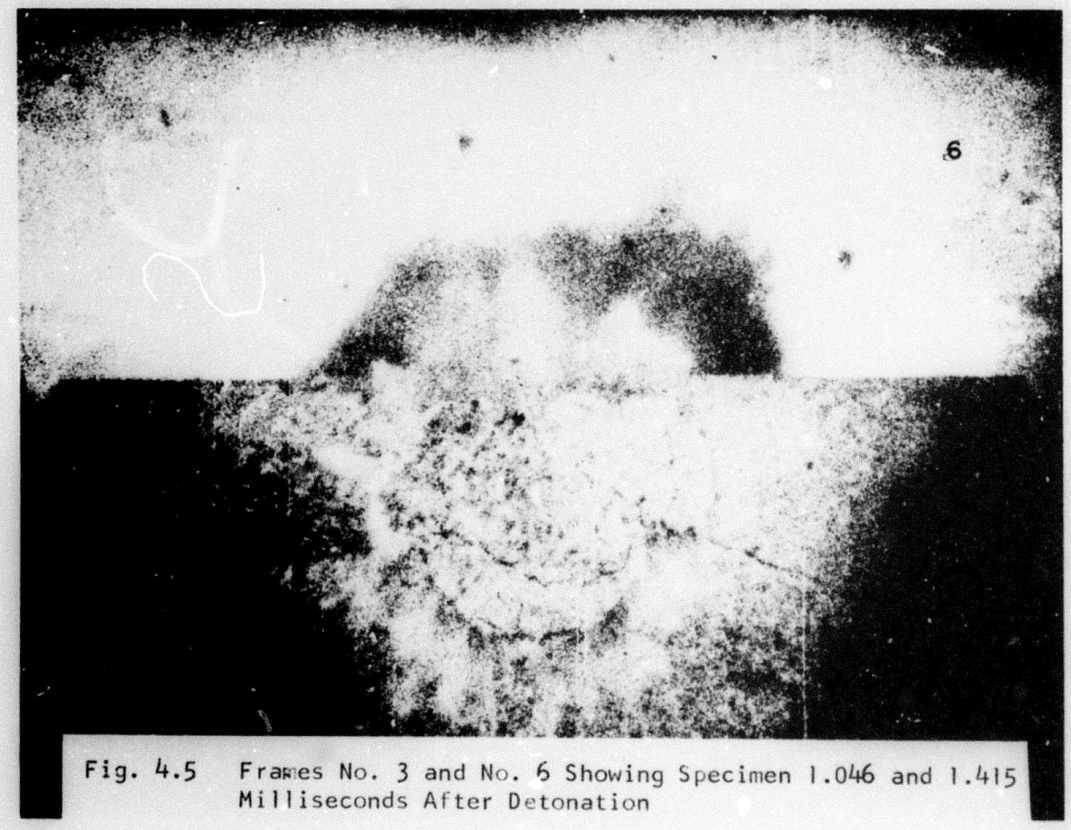

Fig. 4.5 Frames No. 3 and No. 6 Showing Specimen 1.046 and 1.415 Milliseconds After Detonation

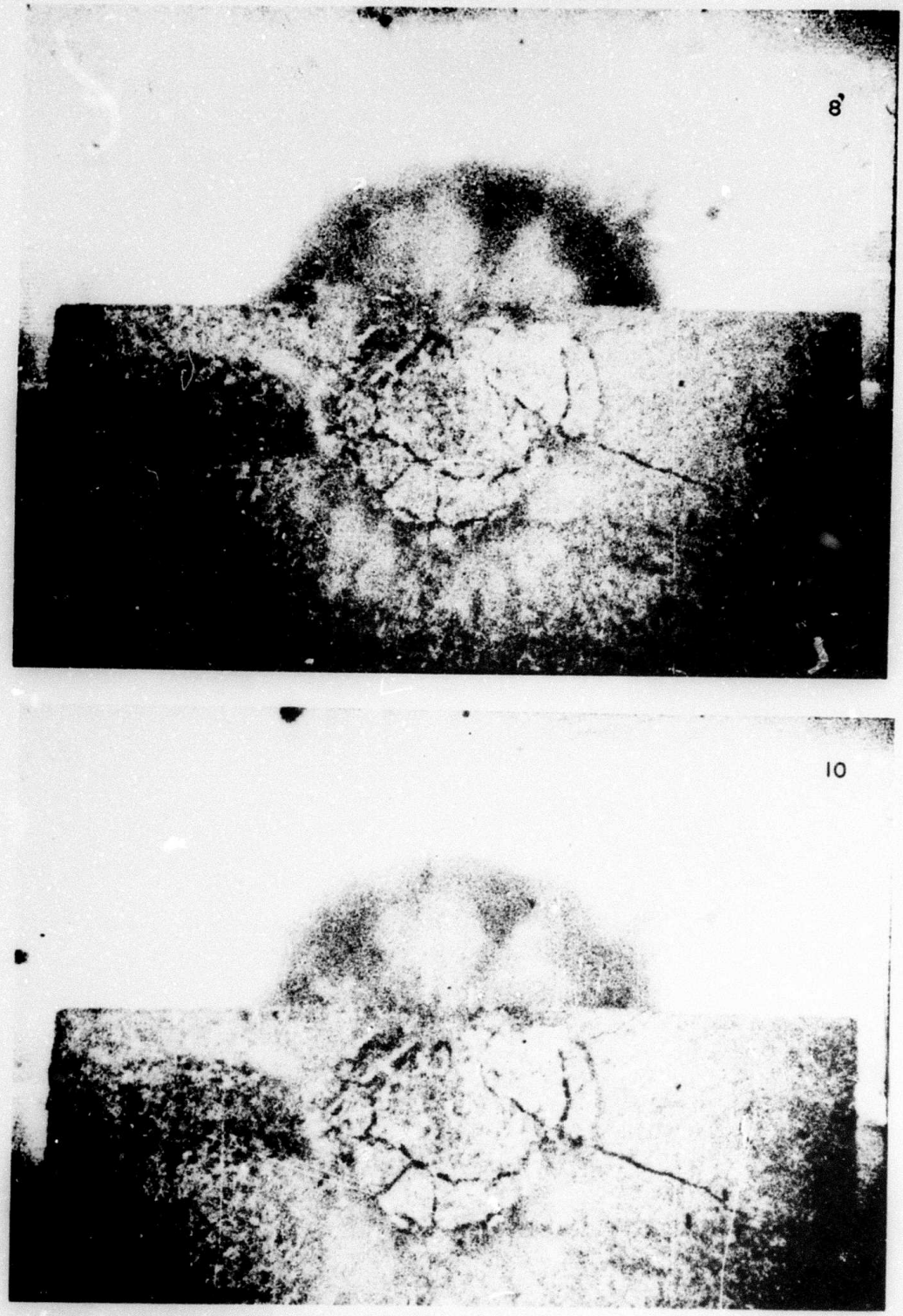

Fig. 4.6 Frames Showing Specimen 1.661 and 1.907 Milliseconds After Detonation

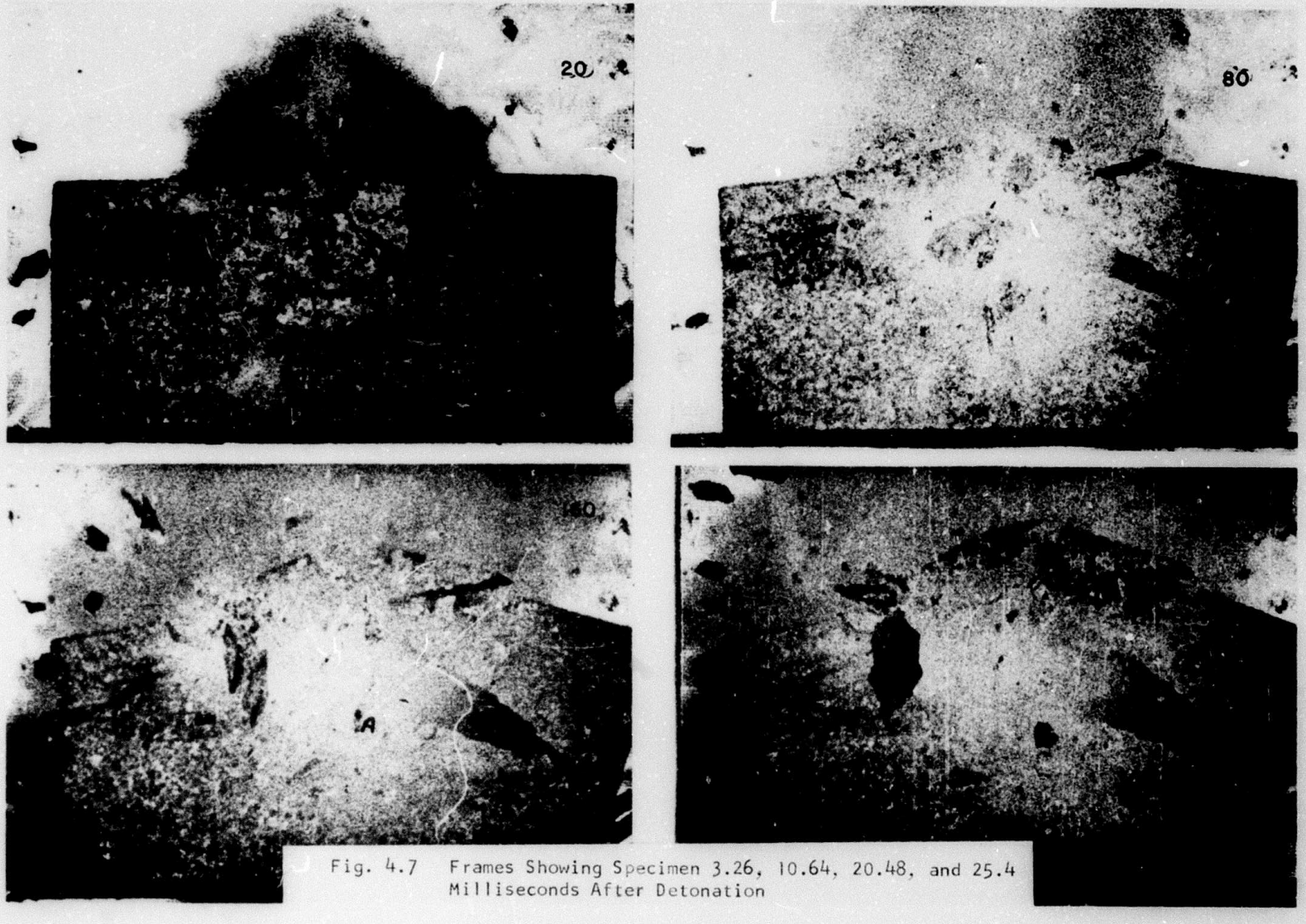

Fig. 4.7 Frames Showing Specimen 3.26, 10.64, 20.48, and 25.4 Milliseconds After Detonation

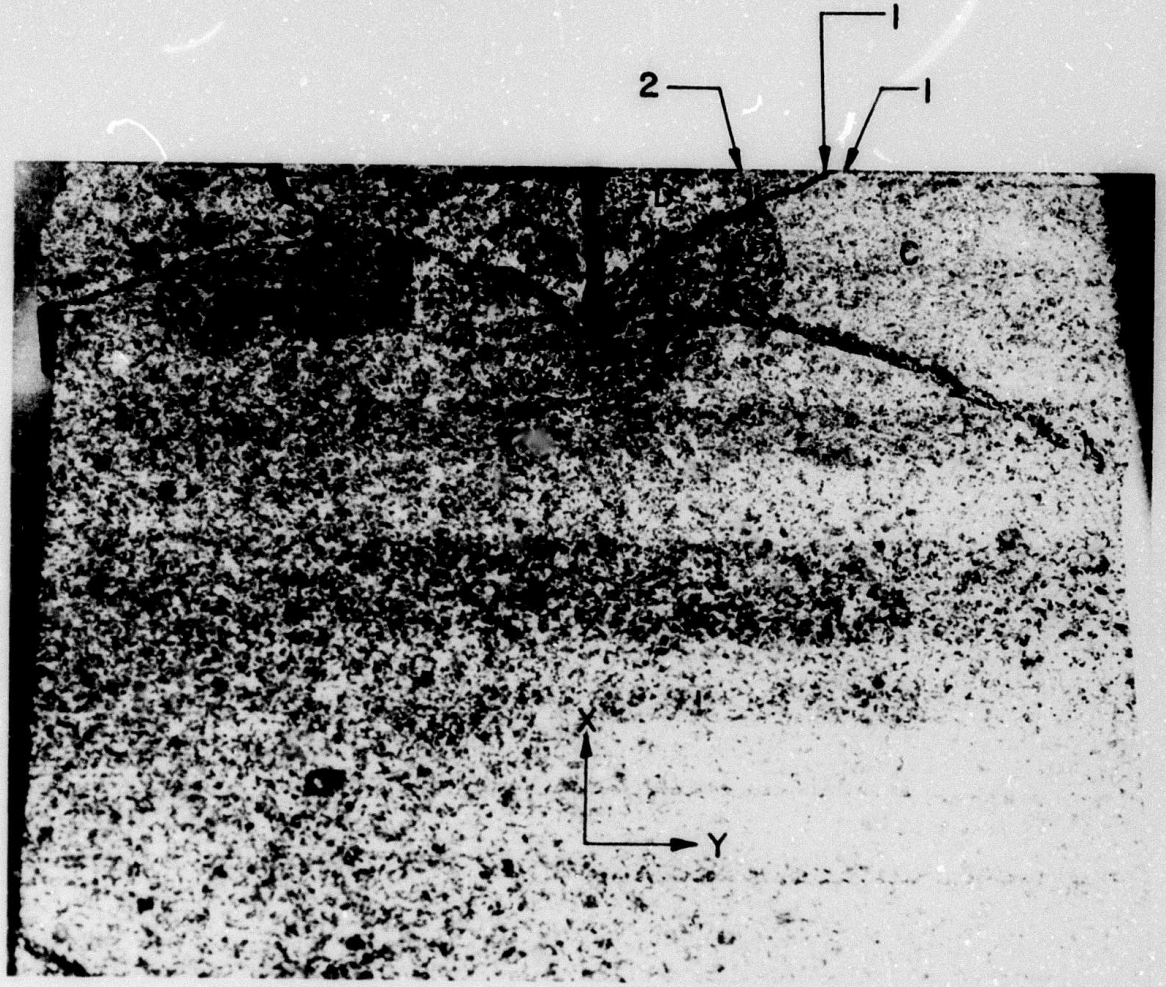

Fig. 4.8 Photograph of Reconstructed Rock After Conclusion of Test

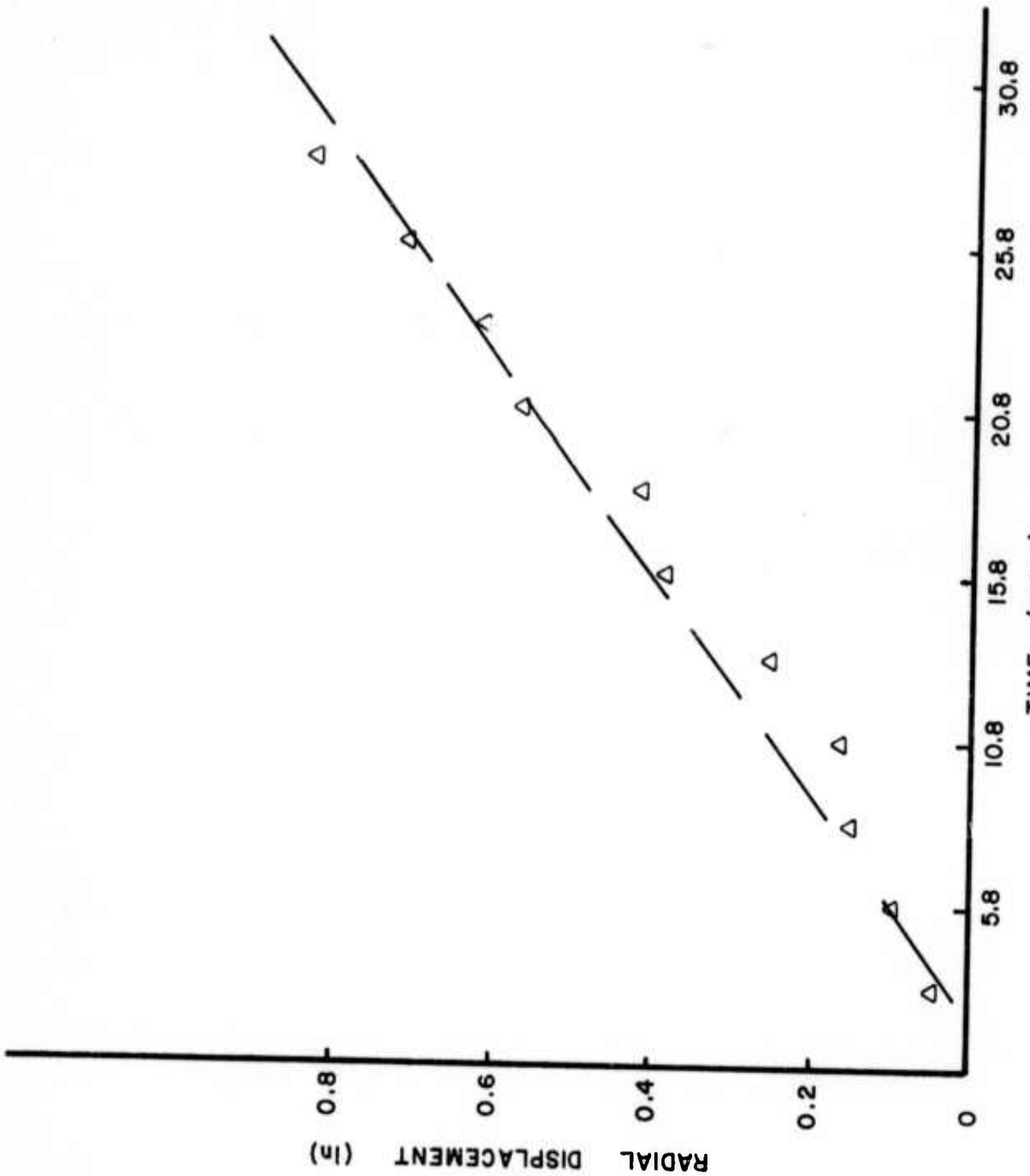

Fig. 4.9 Radial Displacement Versus Time for Particle A

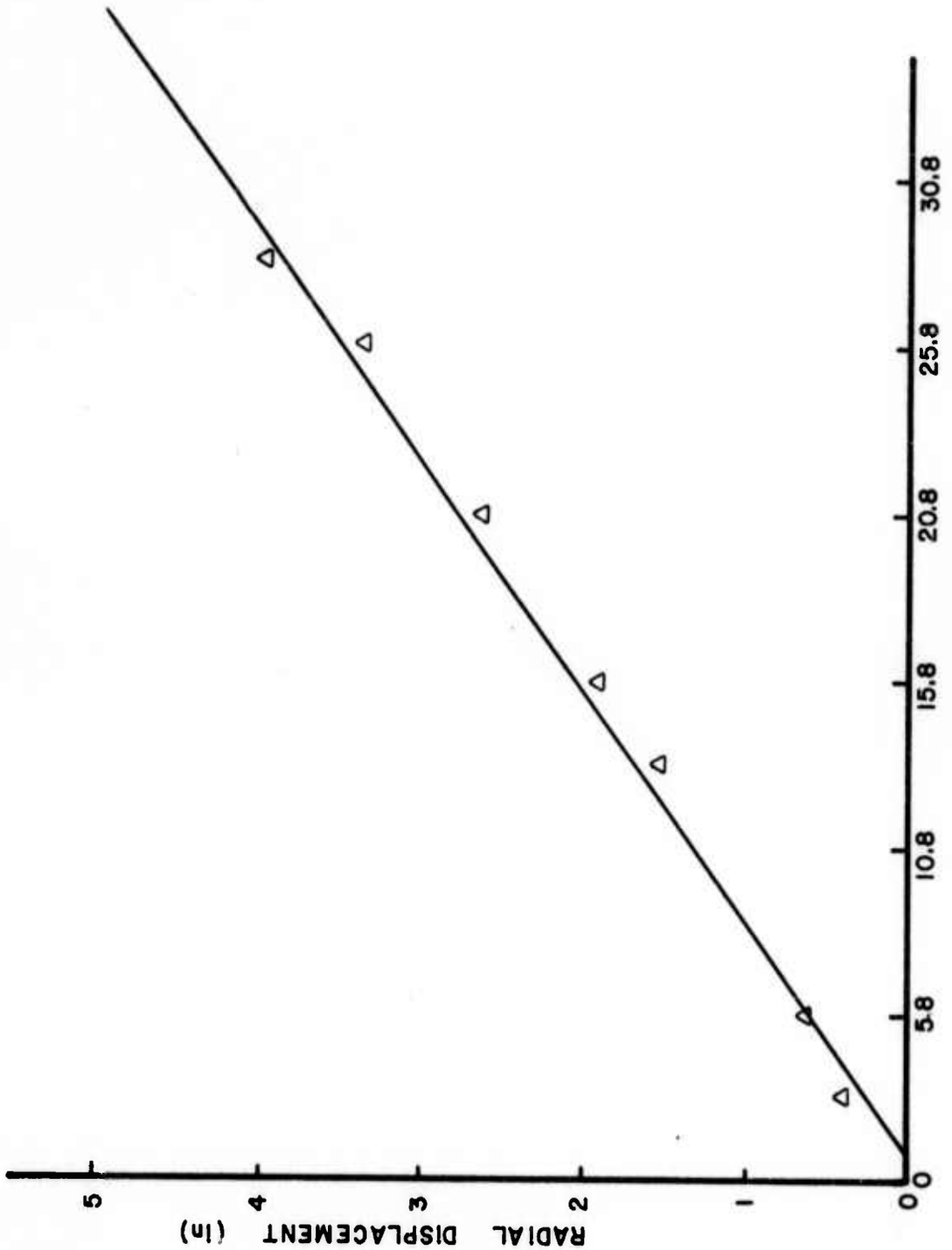

Fig. 4.10 Radial Displacement Versus Time for Particle 8

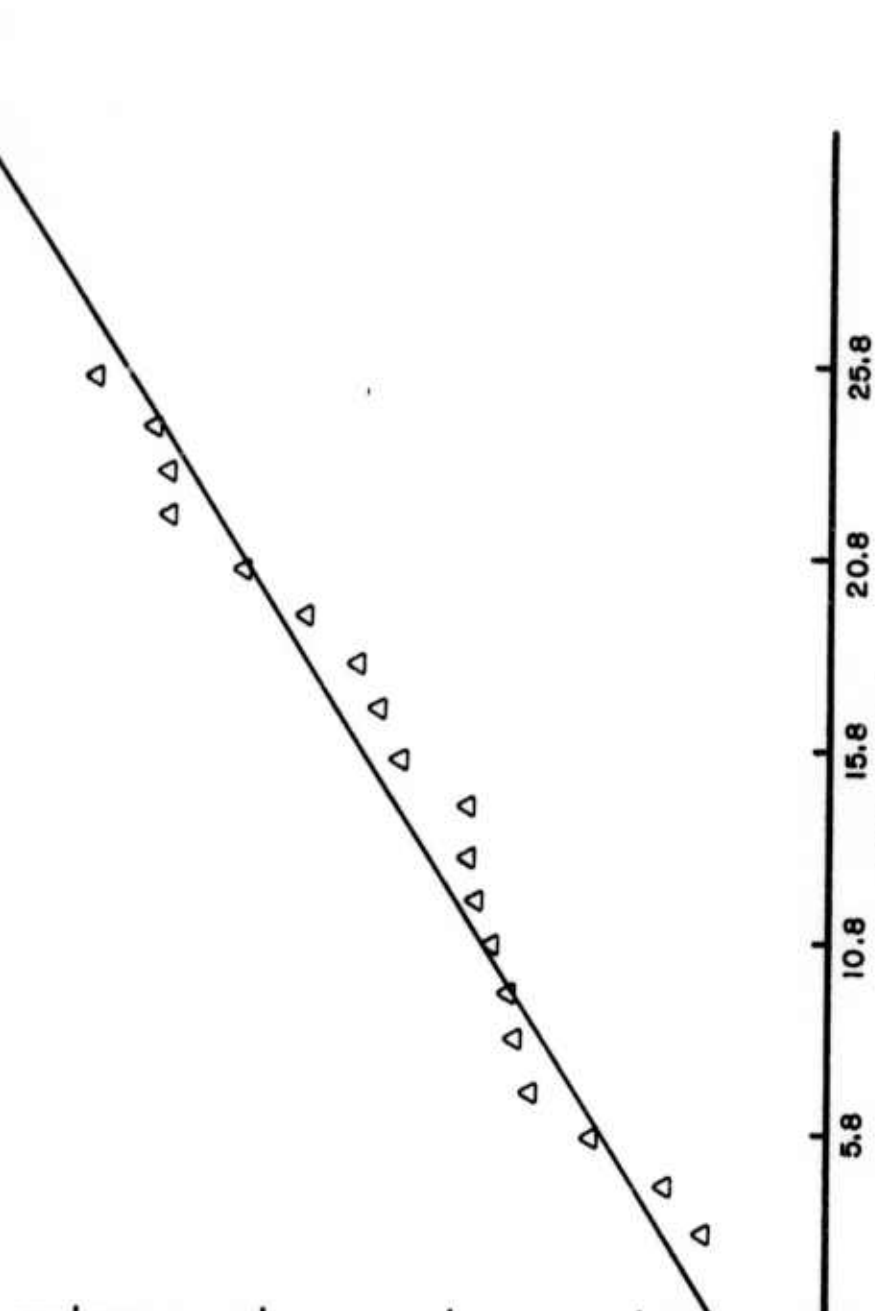

Fig. 4.11 Y Component of Displacement for Point C, as a Function of Time

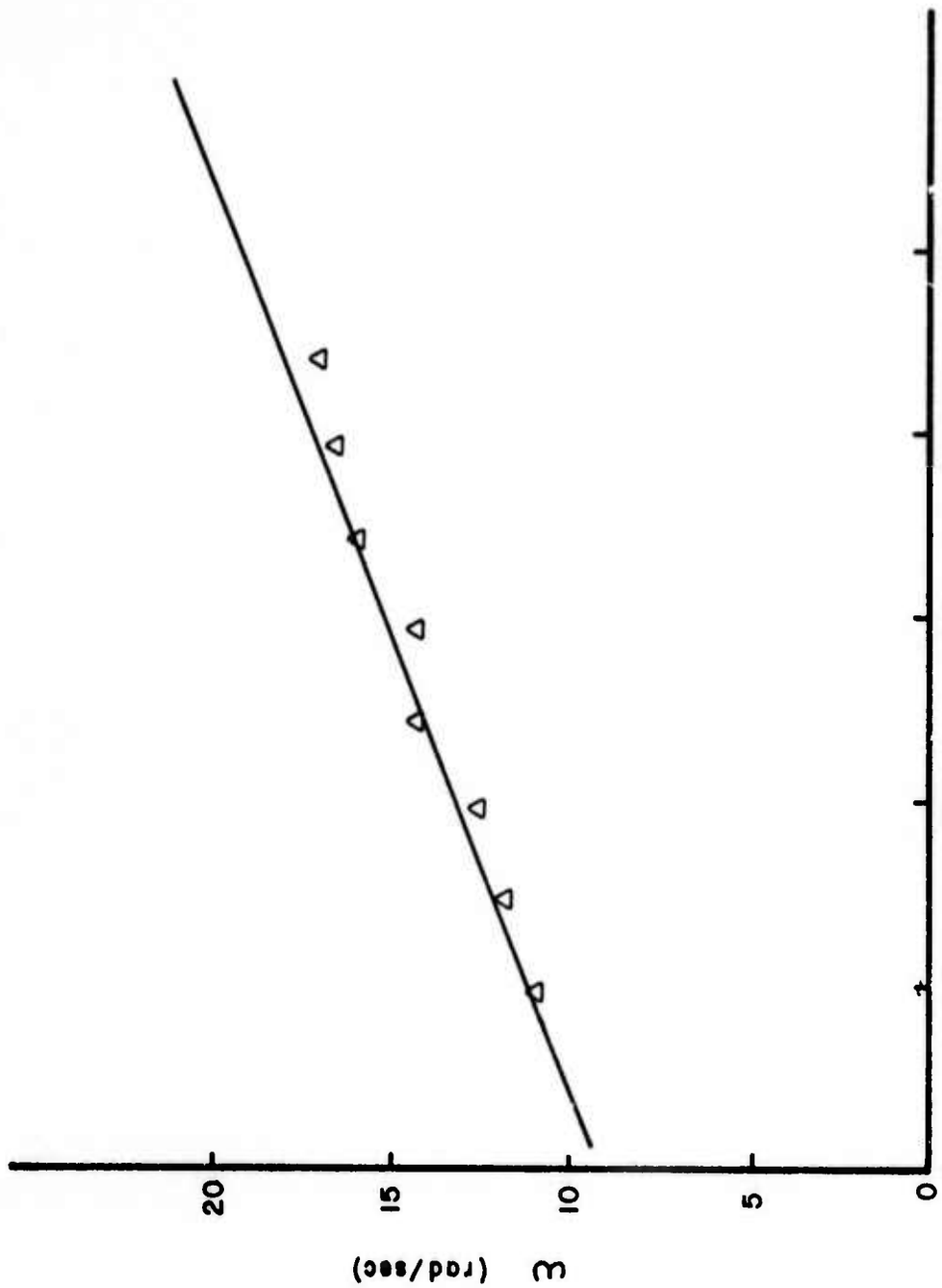

Fig. 4.12 Angular Velocity of Fragment C as a Function of Time

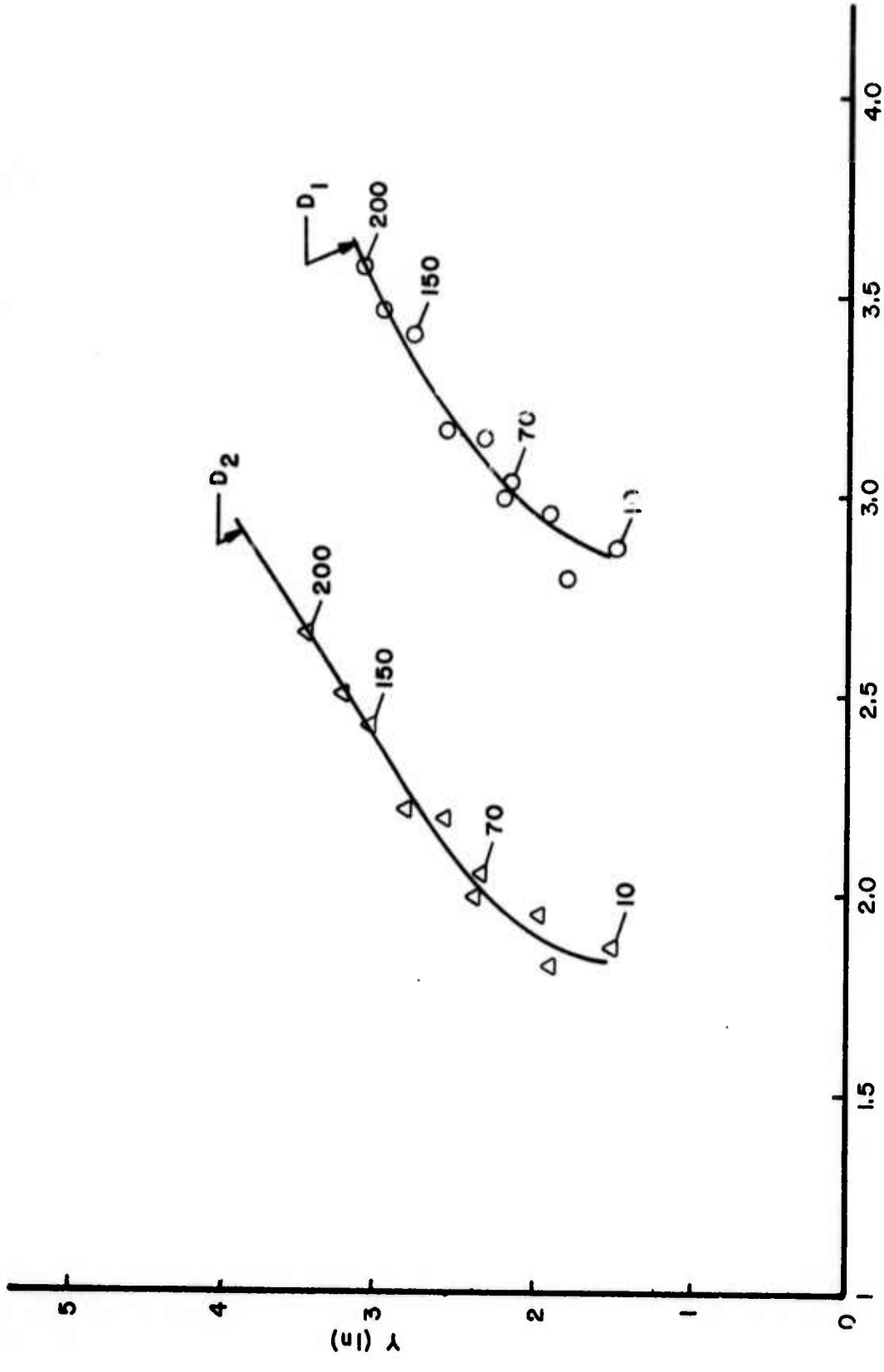

Fig. 4.13 Trajectories of Points D_1 and D_2 Located on Fragment D

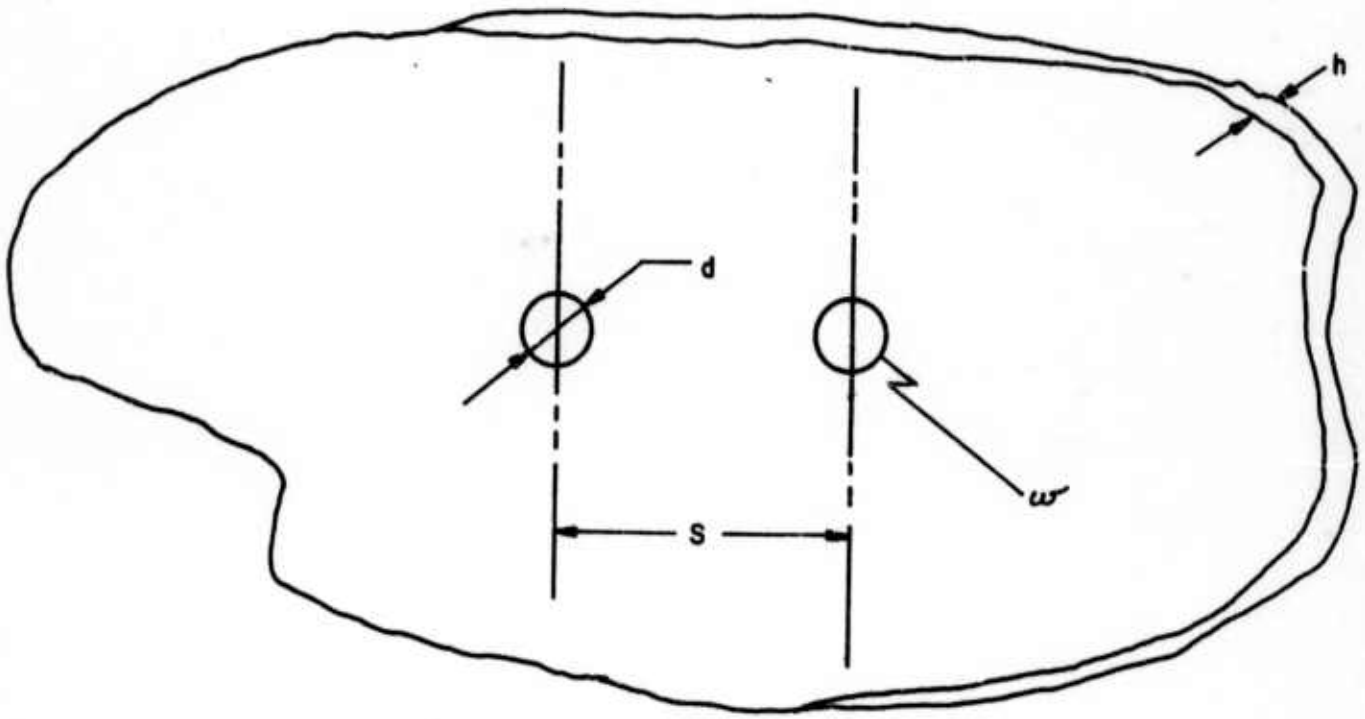

Fig. 5.1 Geometric Parameters of Two Source Model

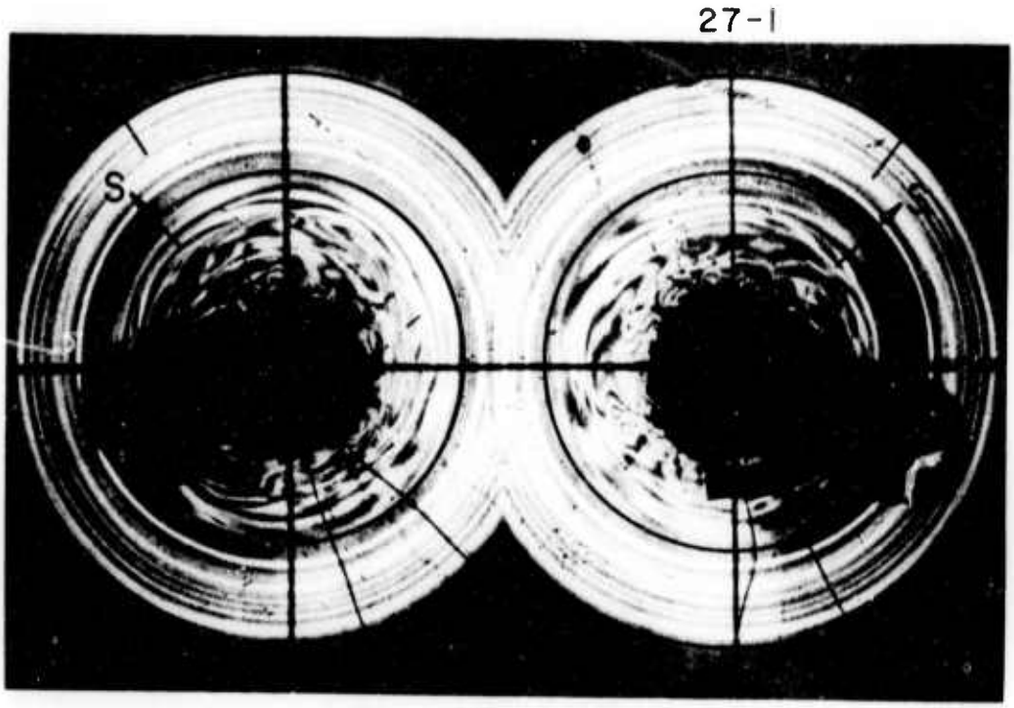

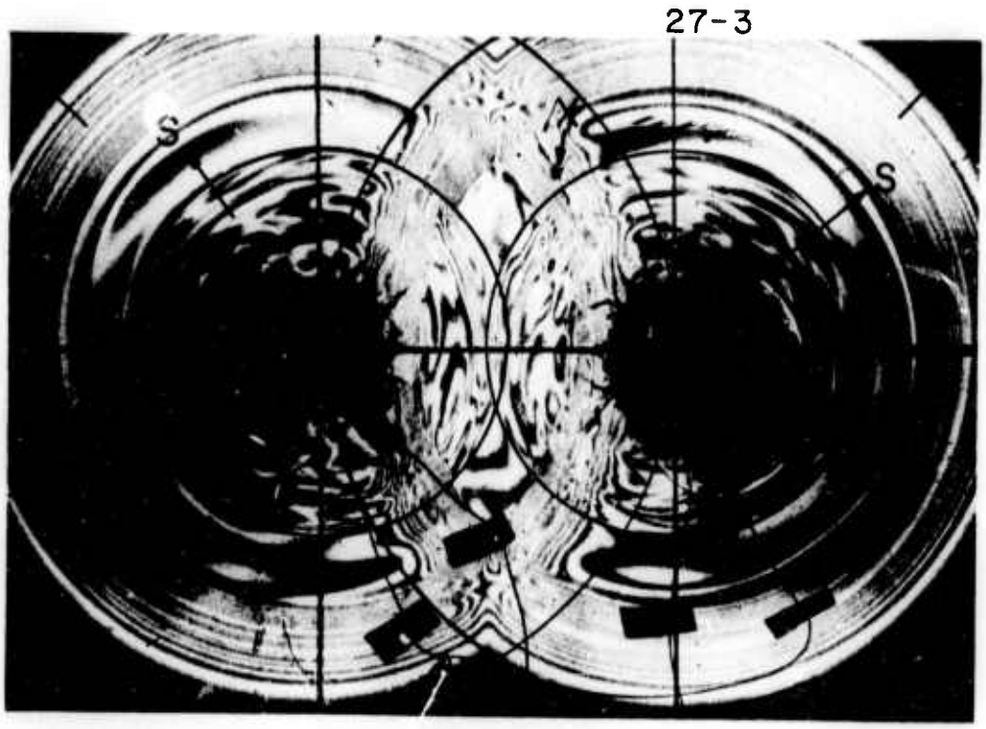

Fig. 5.2.1 Dynamic Fringe and Crack Pattern During the Early Phase of the Event. (Model H-27)

27-4

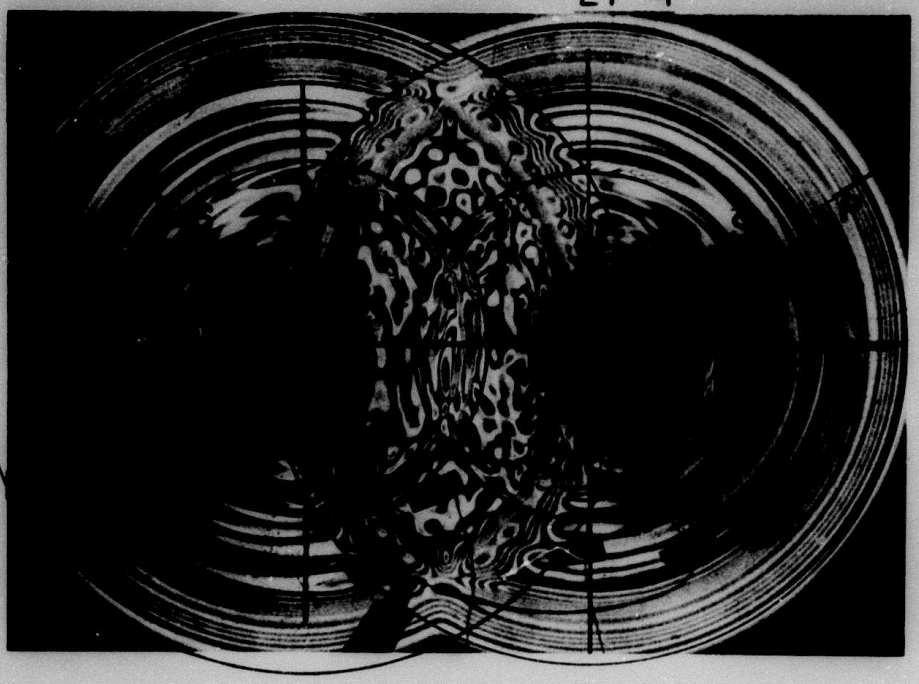

27-5

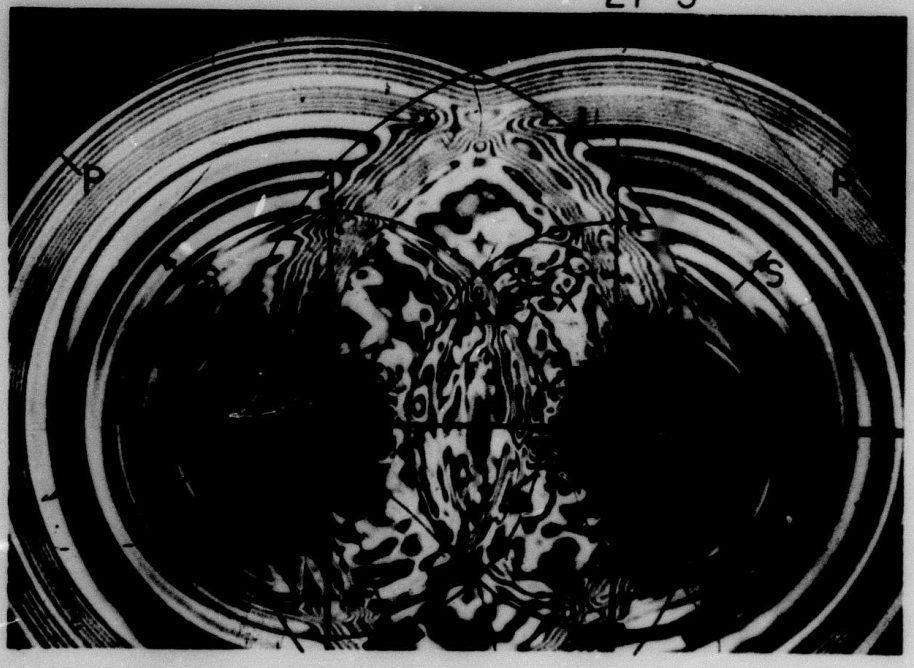

Fig. 5.2.2 Development of Dynamic Fracture Pattern Due to the P Wave. (Model H-27)

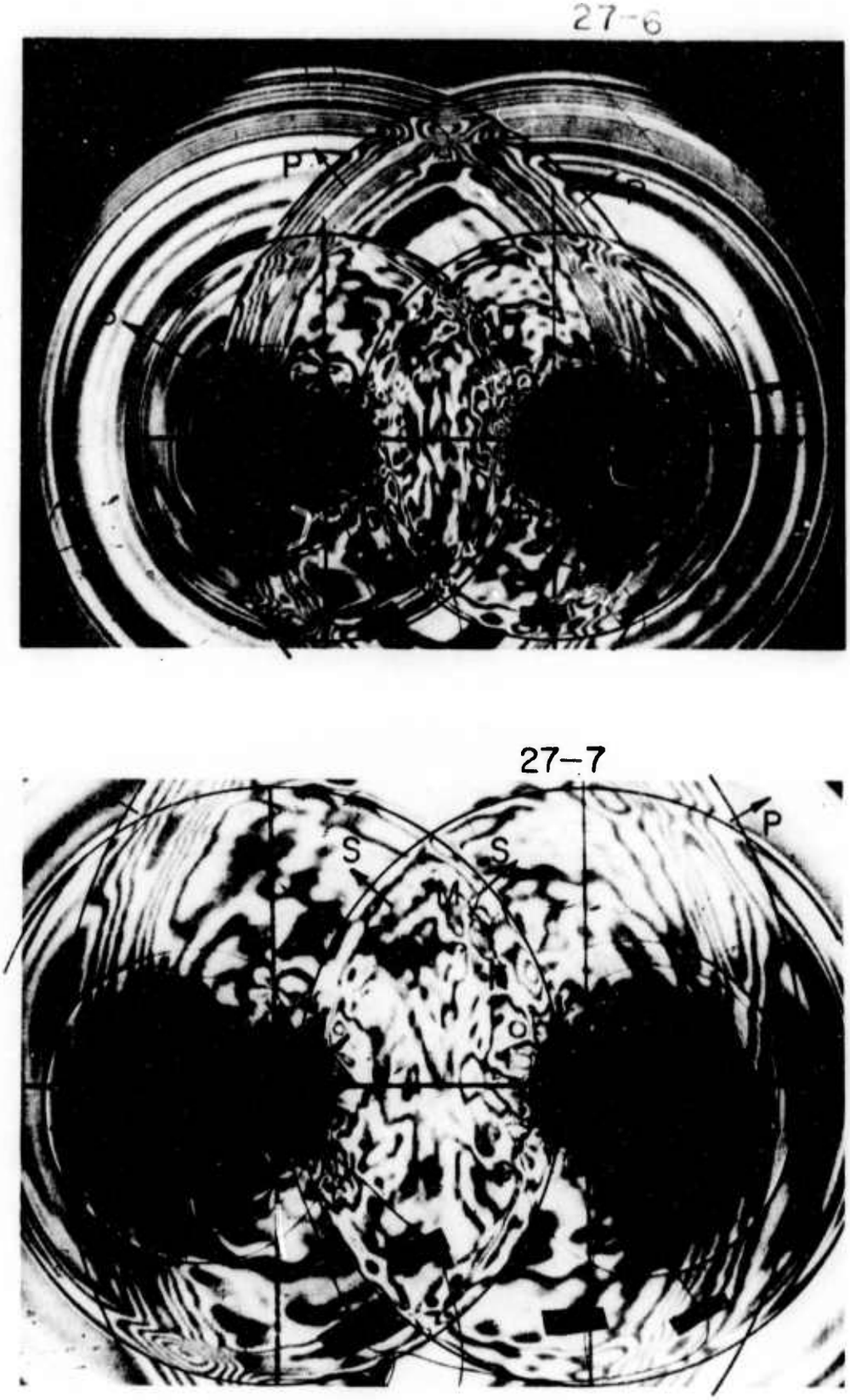

Fig. 5.2.3 Interaction of S Wave With Cracks (Model H-27)

Fig. 5.2.4 Arrest Phase of the Fracture Process (Model H-27)

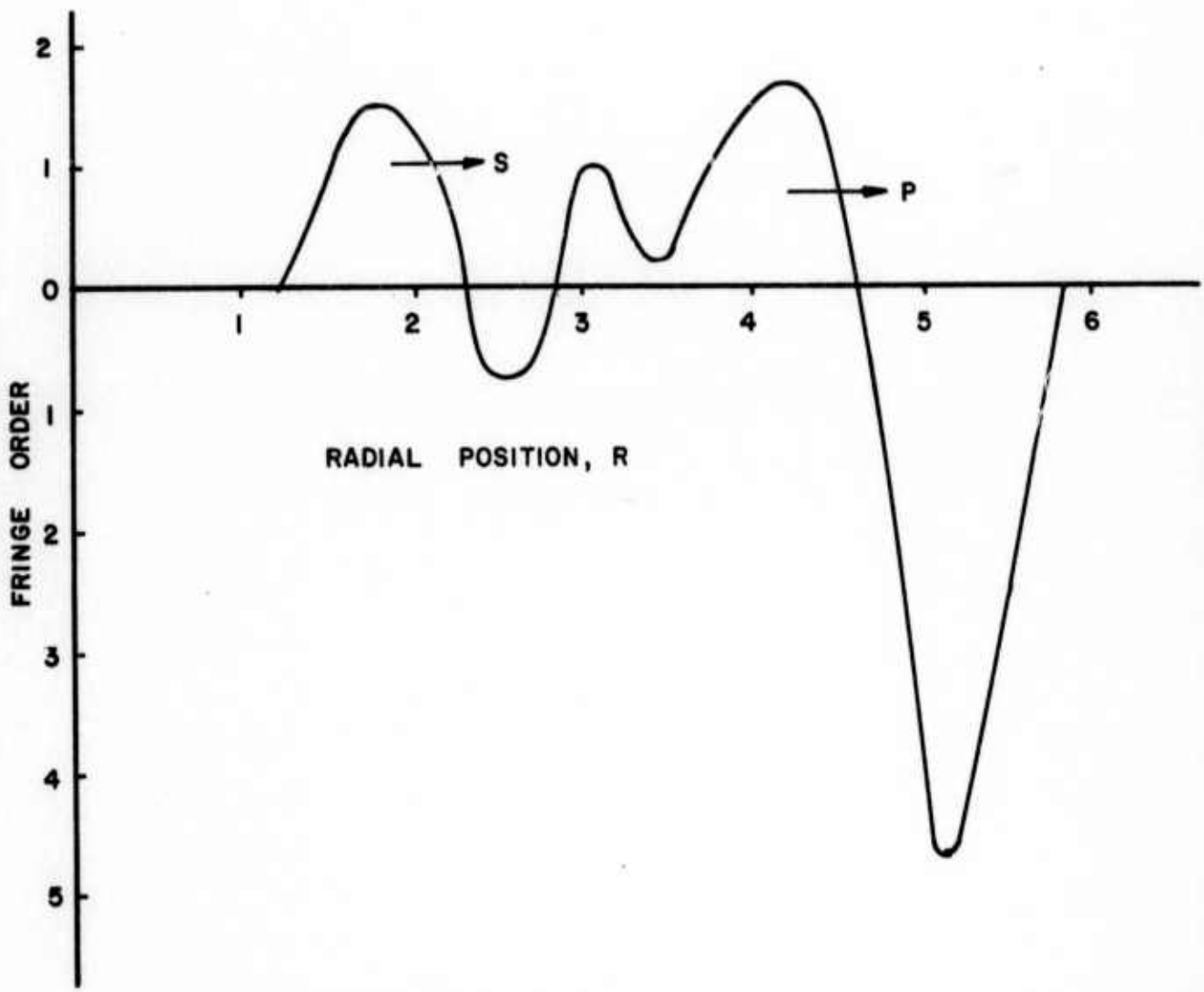

Fig. 5.3 Profile of P and S Waves as a Function of Position r. (Frame 27-5)

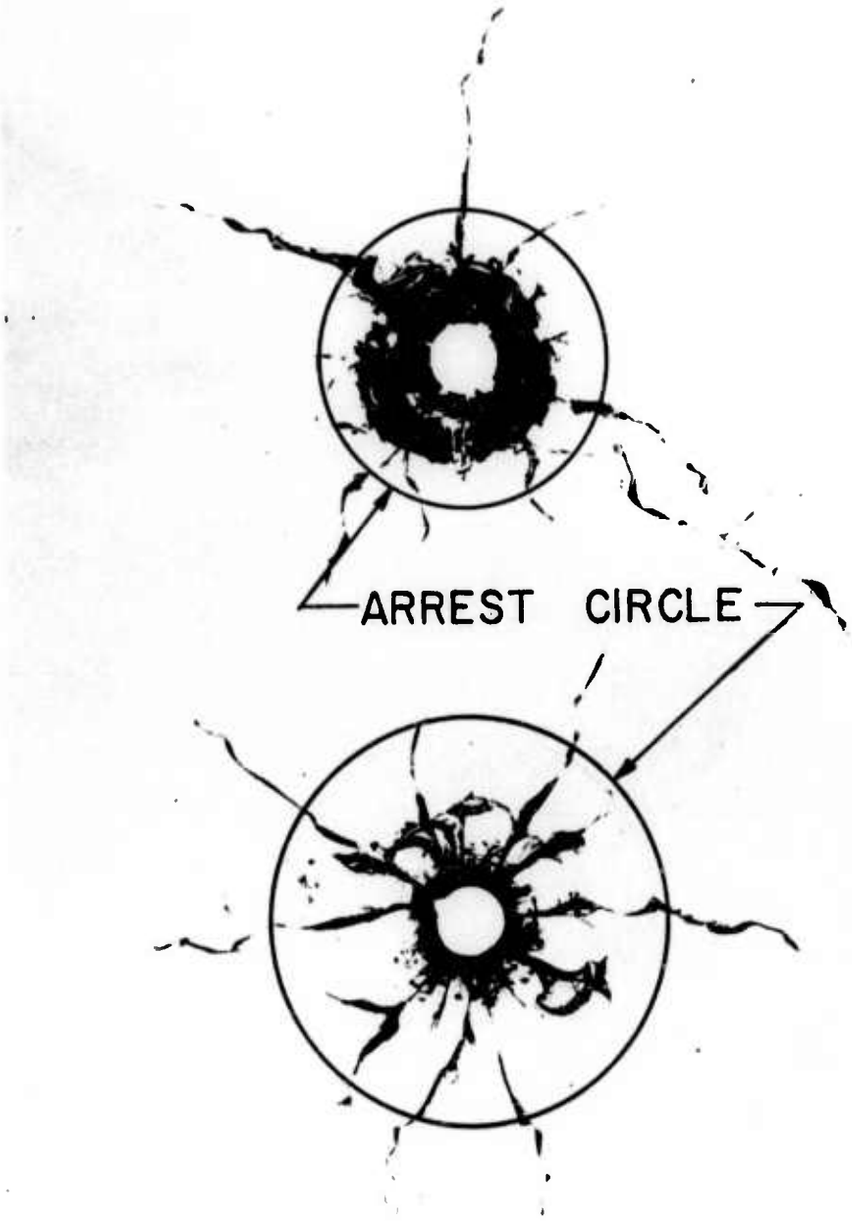

Fig. 5.4 Final Crack Patterns in Model H-27

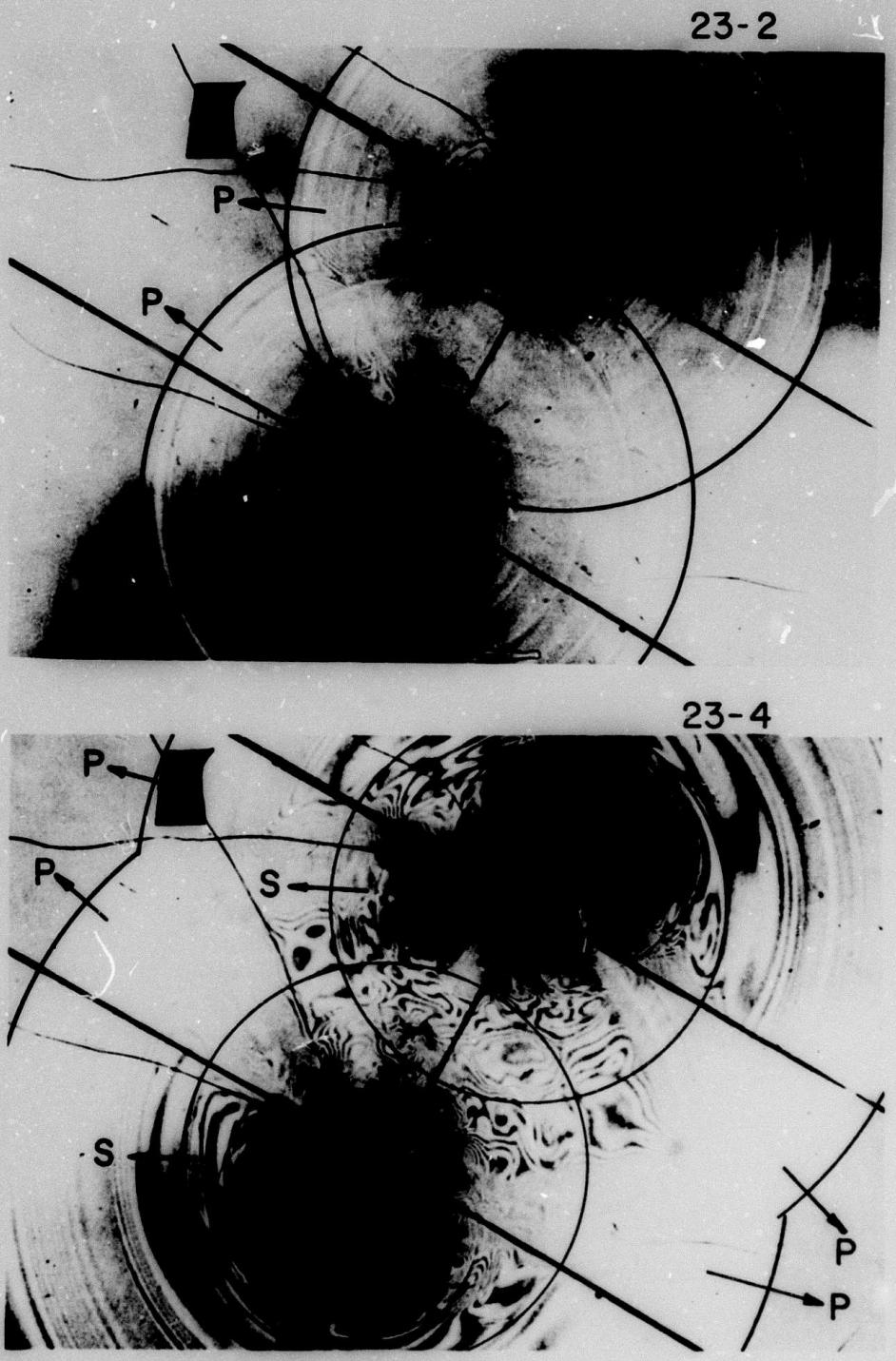

Fig. 5.5.1 Dynamic Fringe and Crack Pattern During the Early Phase of the Event (Model H-23)

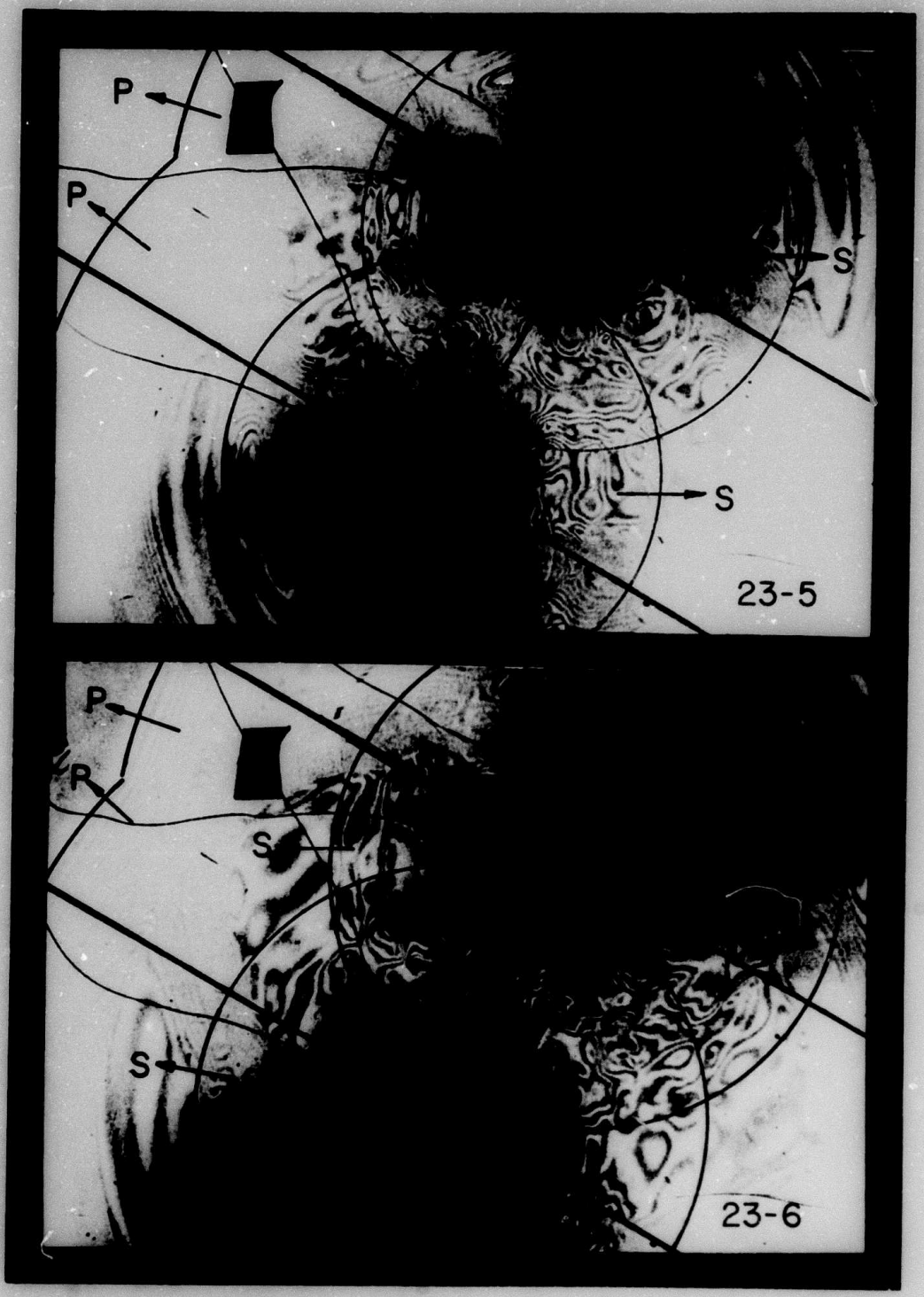

Fig. 5.5.2 Development of Dynamic Fracture Patterns Due to P and S Waves (Model H-23)

Fig. 5.5.3 Final Phase of Crack Propagation (Model H-23)

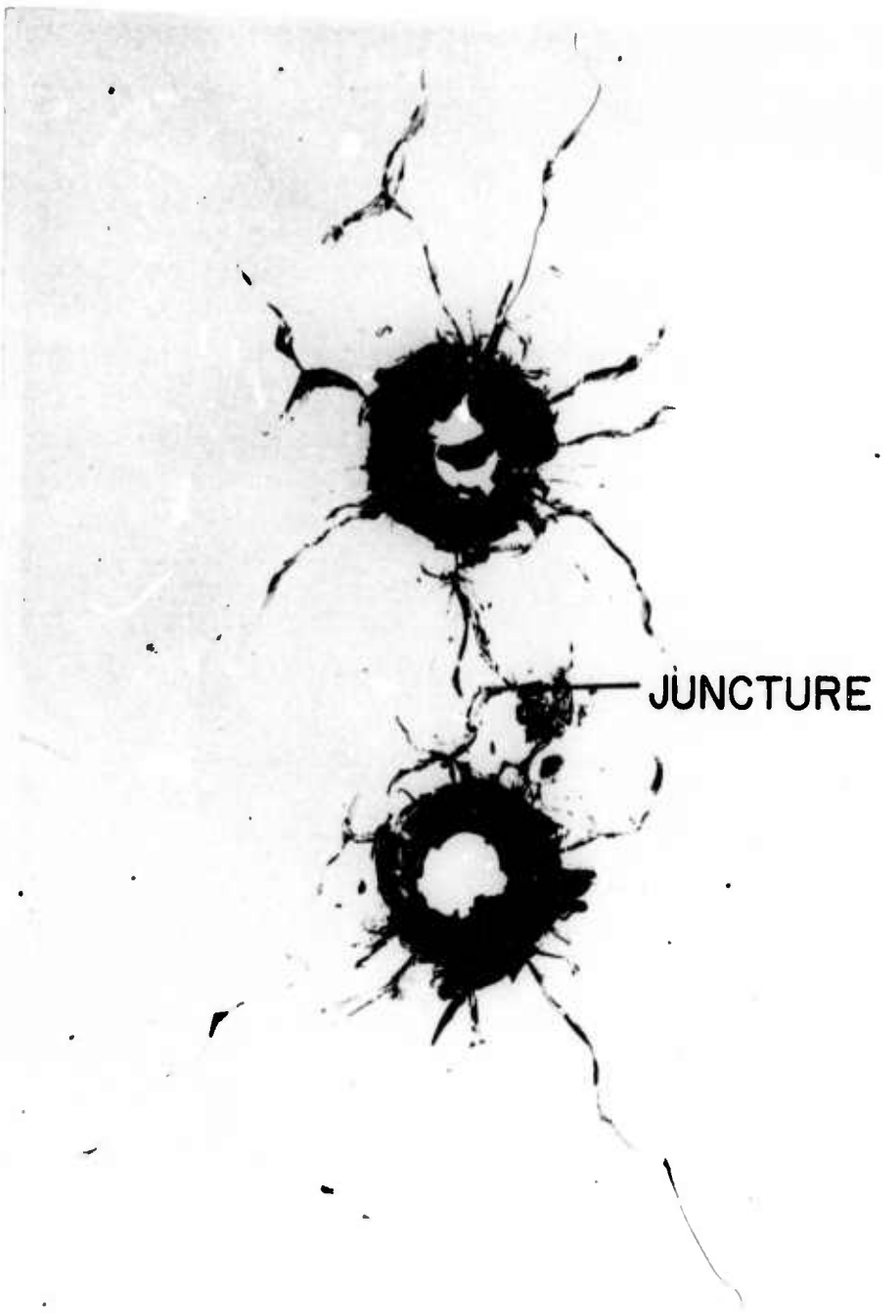

Fig. 5.6 Final Crack Pattern in Model H-23

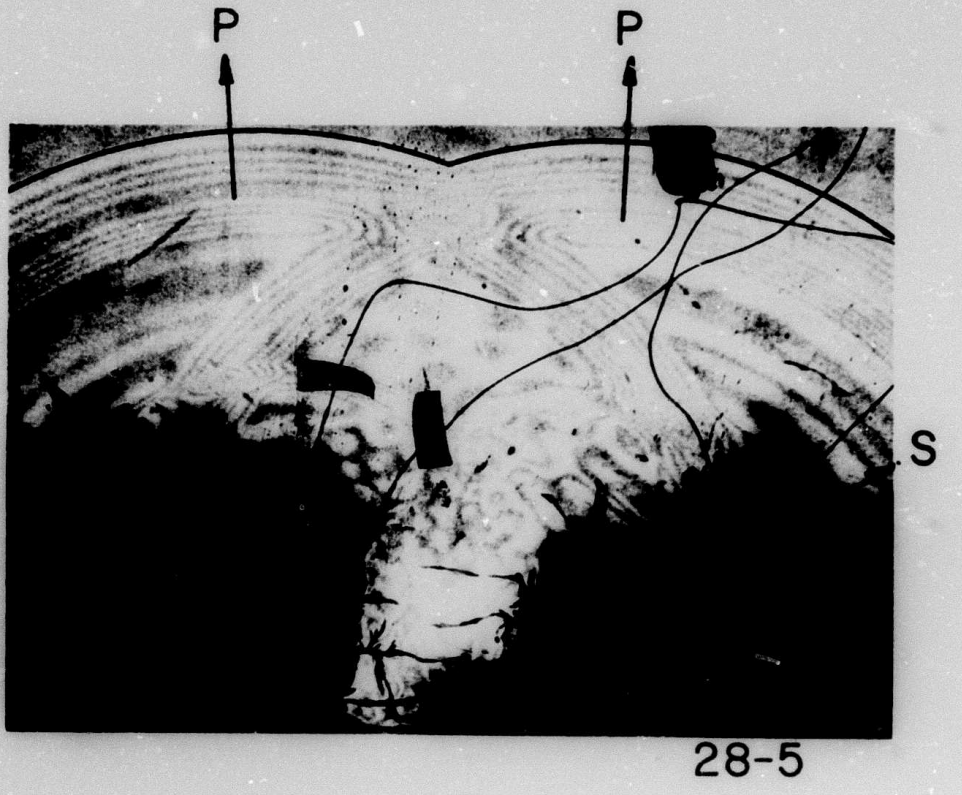

Fig. 5.7.1 Dynamic Fringe and Crack Pattern During the Early Phase of the Event. (Model H-28)

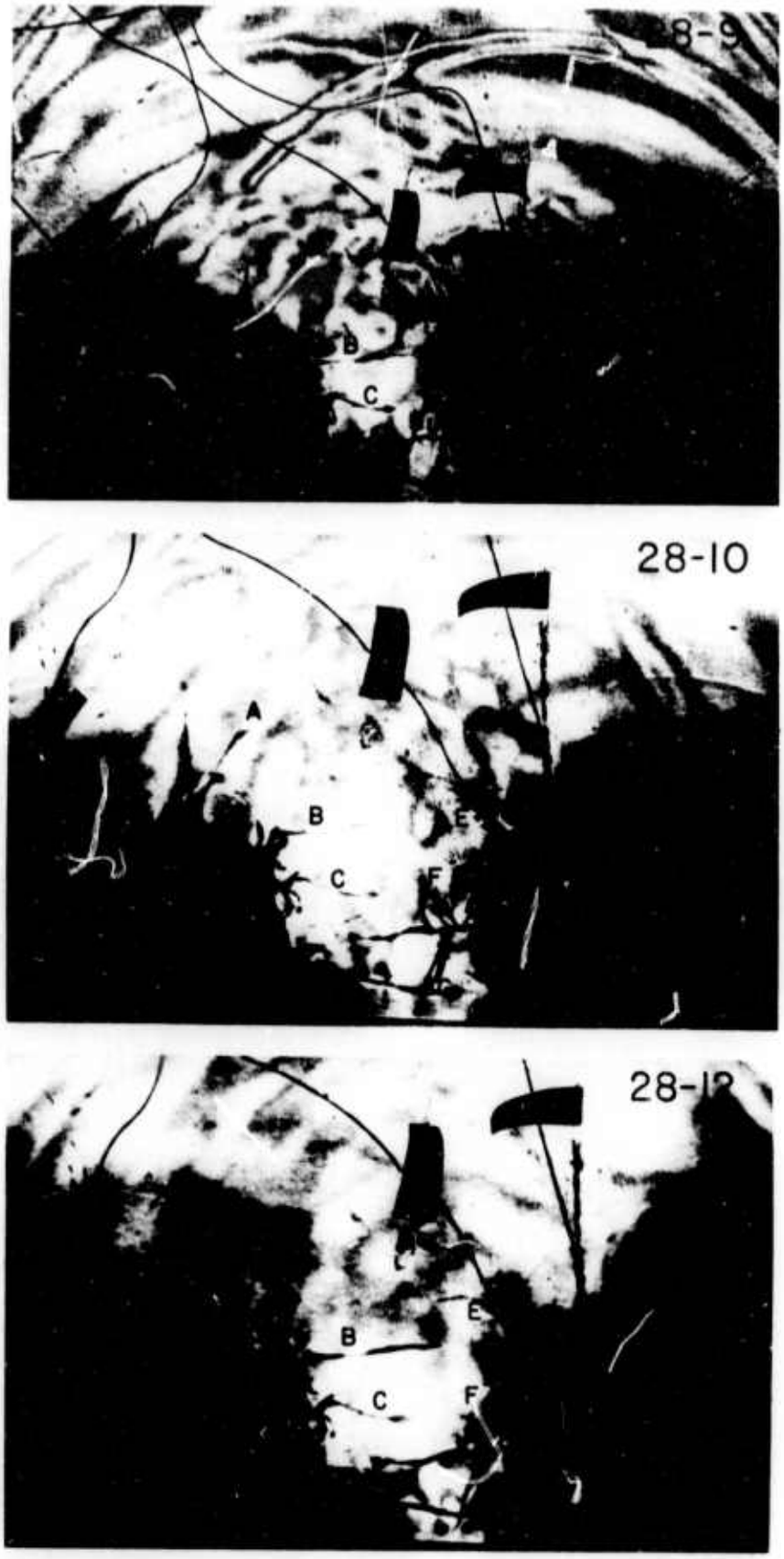

Fig. 5.7.2 Development of Dynamic Fracture Pattern (Model H-28)

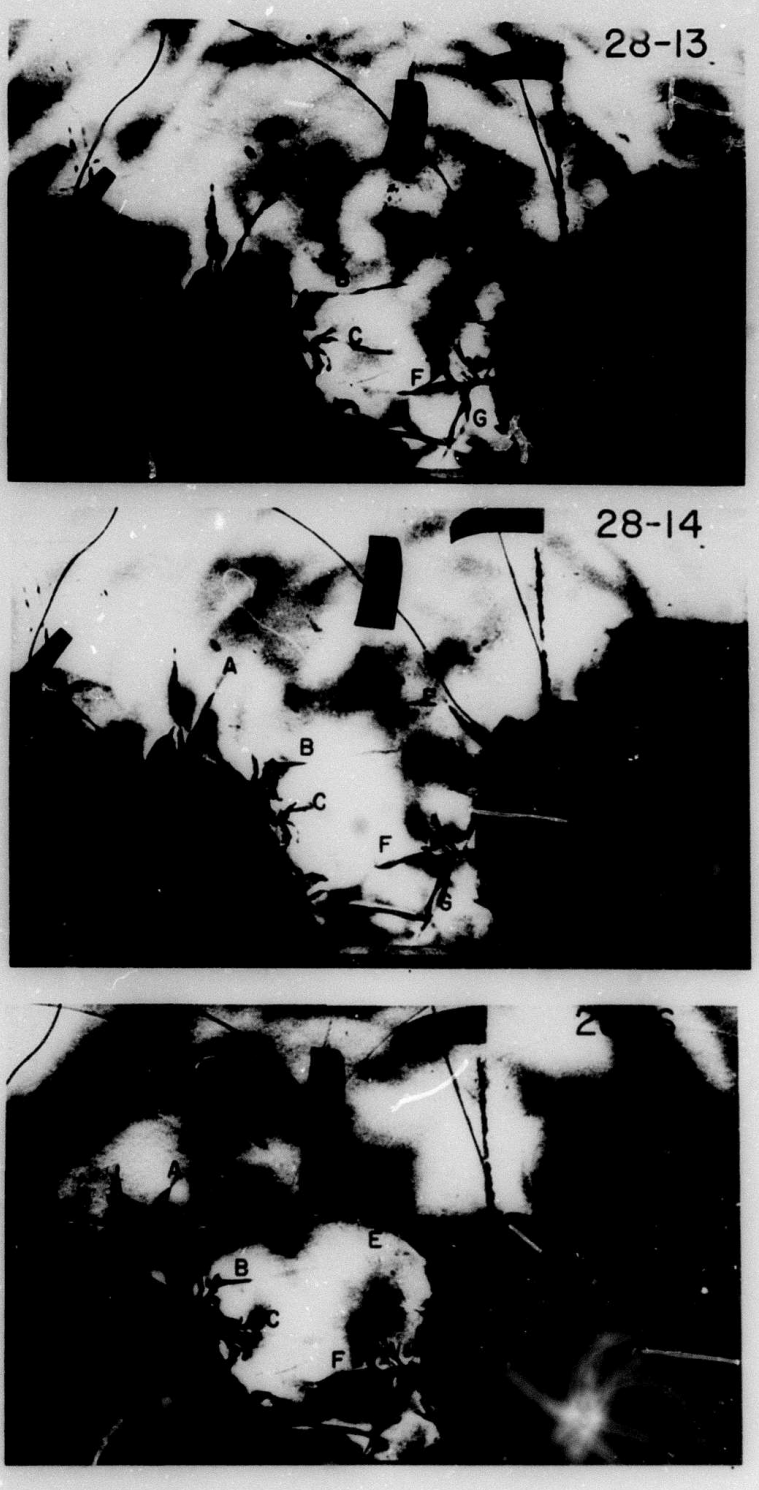

Fig. 5.7.3 Final Phase of Crack Propagation (Model H-28)

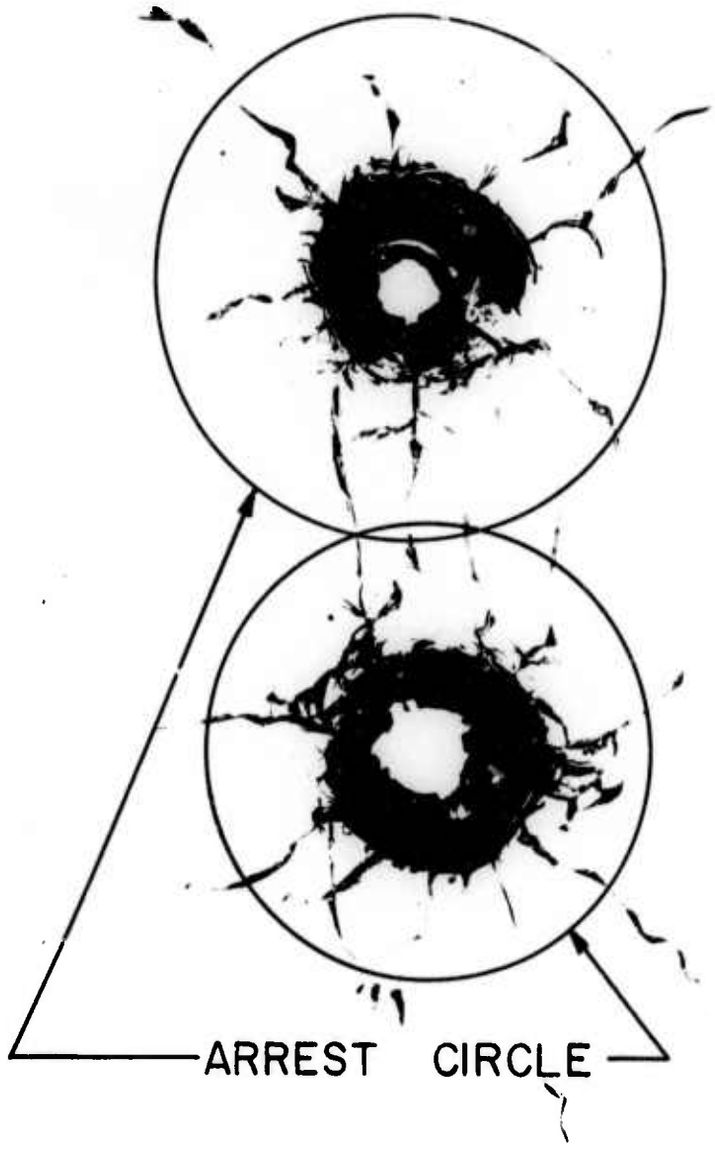

Fig. 5.8 Final Crack Pattern for Model H-28

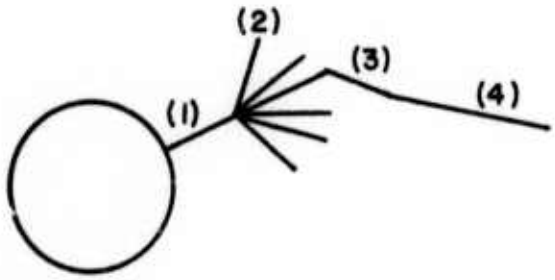

(1) PRIMARY RADIAL CRACK

(2) MULTIPLE BRANCHING AND ARREST DUE TO P

(3) REINITIATION AND GROWTH DUE TO S

(4) FINAL PHASE OF CRACK GROWTH

Fig. 5.9 Growth of a Typical Crack

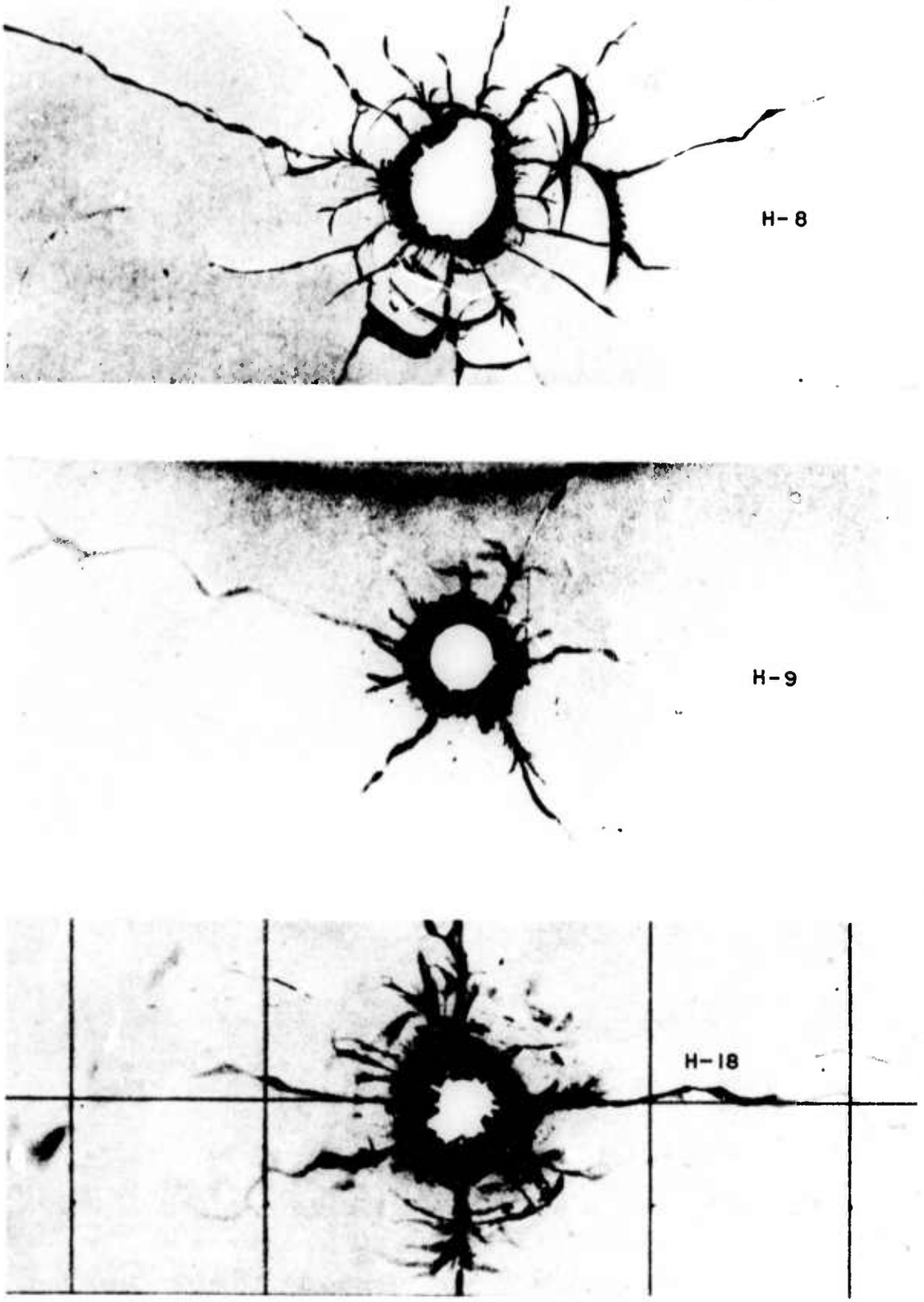

Fig. 6.1 Crack Patterns Existing Before Detonation for Models H-8, H-9 and H-18

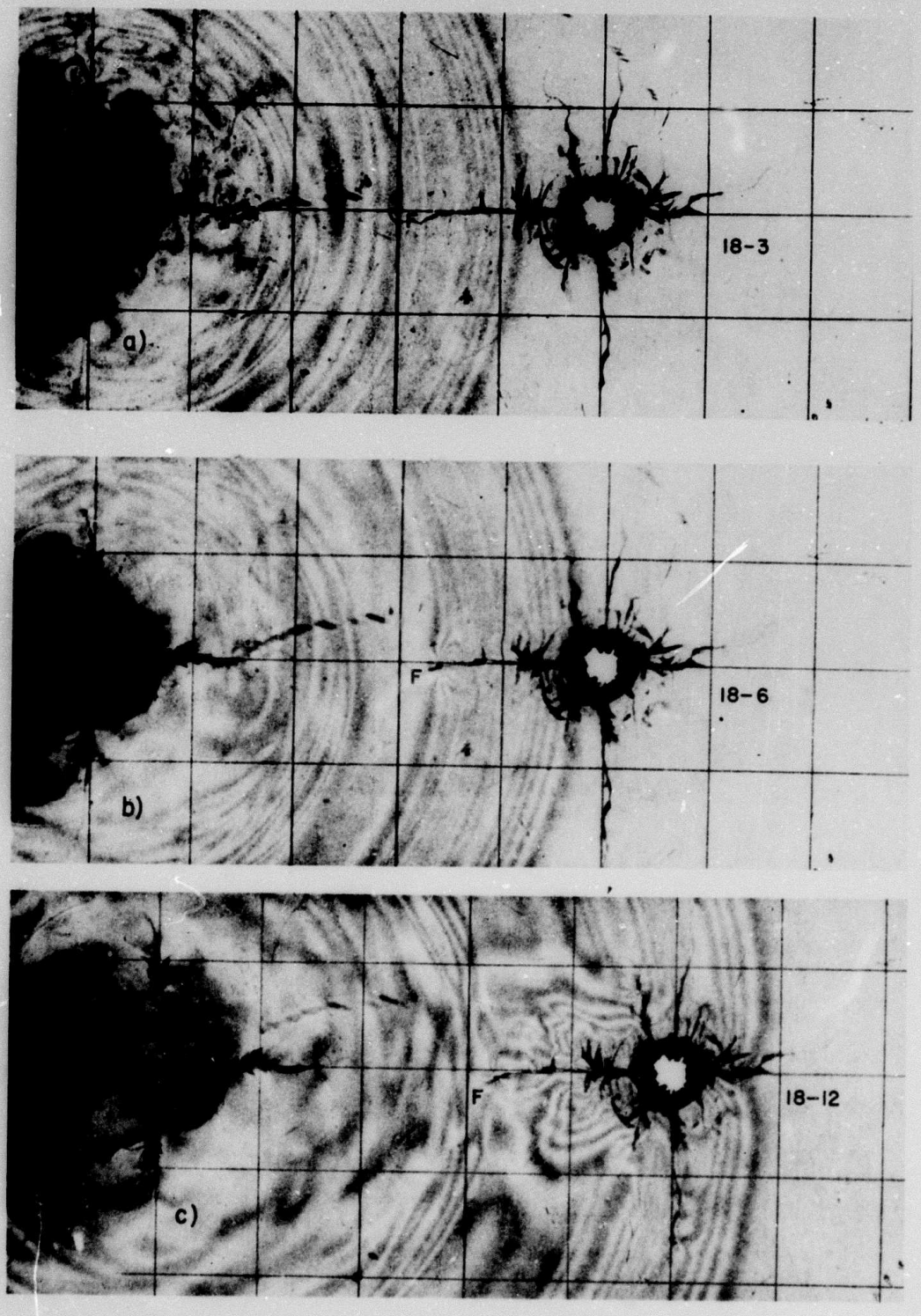

Fig. 6.2 Frames H-18-3, H-18-6 and H-18-12 Depicting the P Wave Interacting With an Arrested Crack

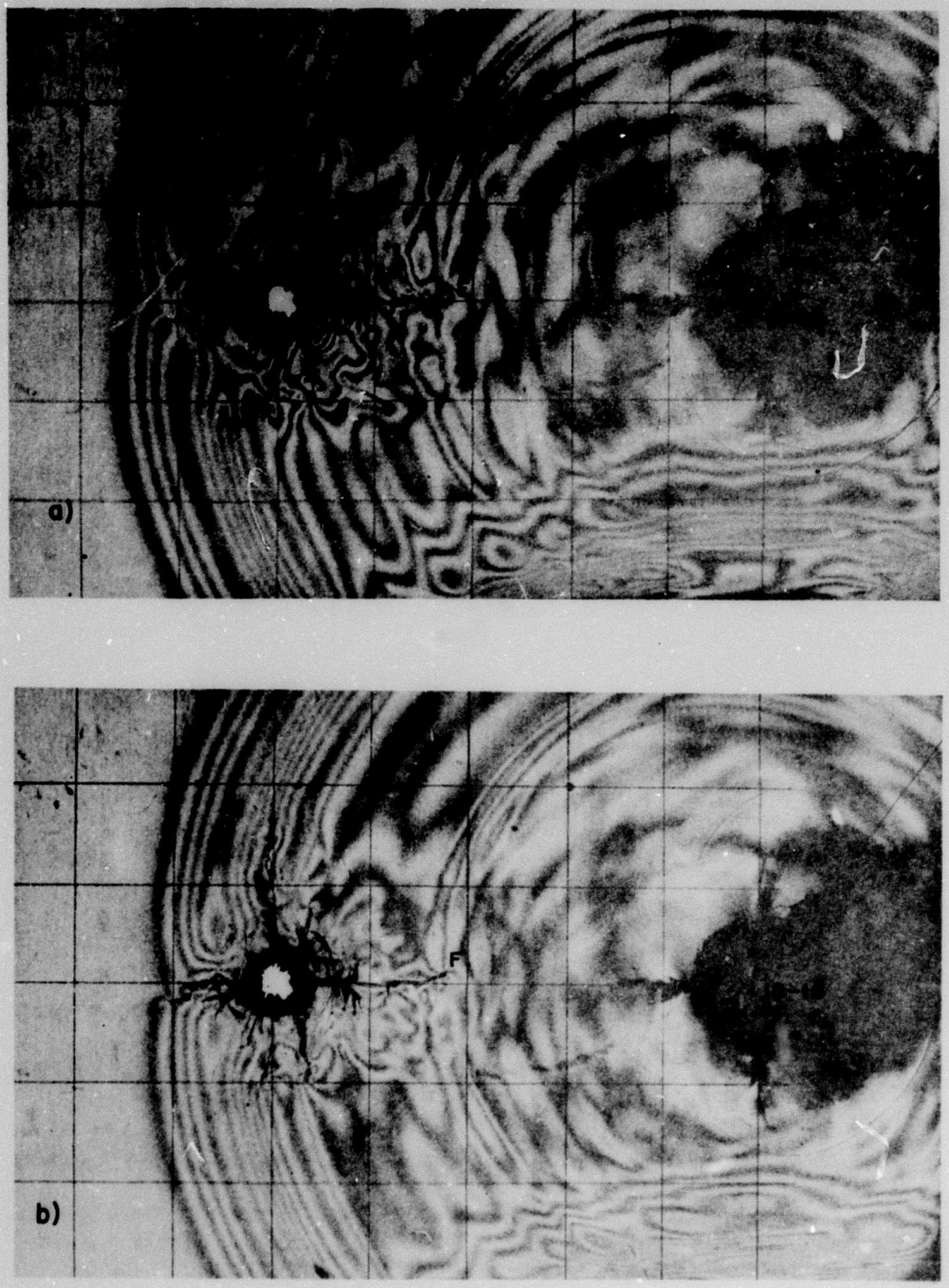

Fig. 6.3 Frames H-18-14 and H-18-16 Depicting the S Wave Interacting With an Arrested Crack

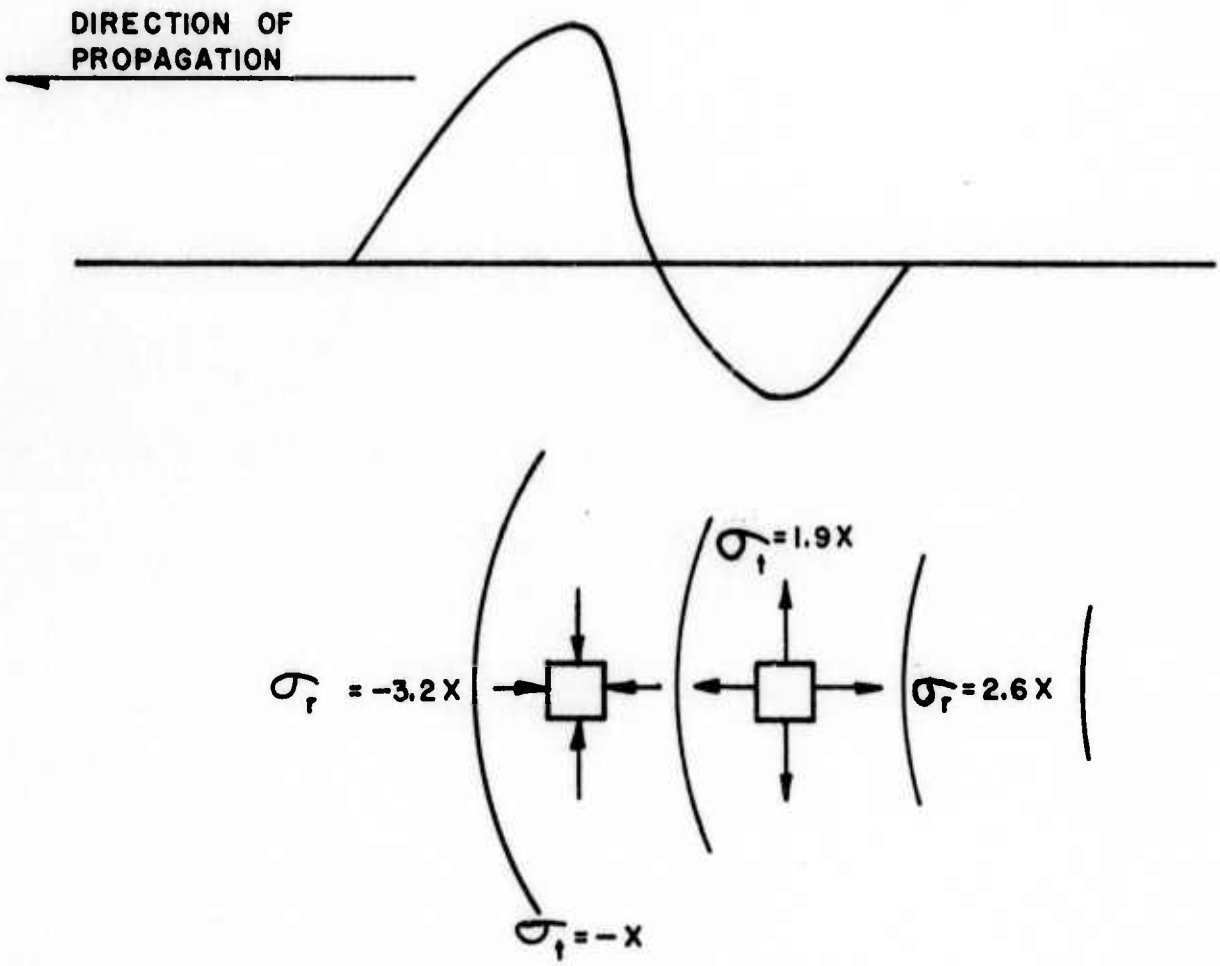

Fig. 6.4 State of Stress Present in a Propagating P Wave

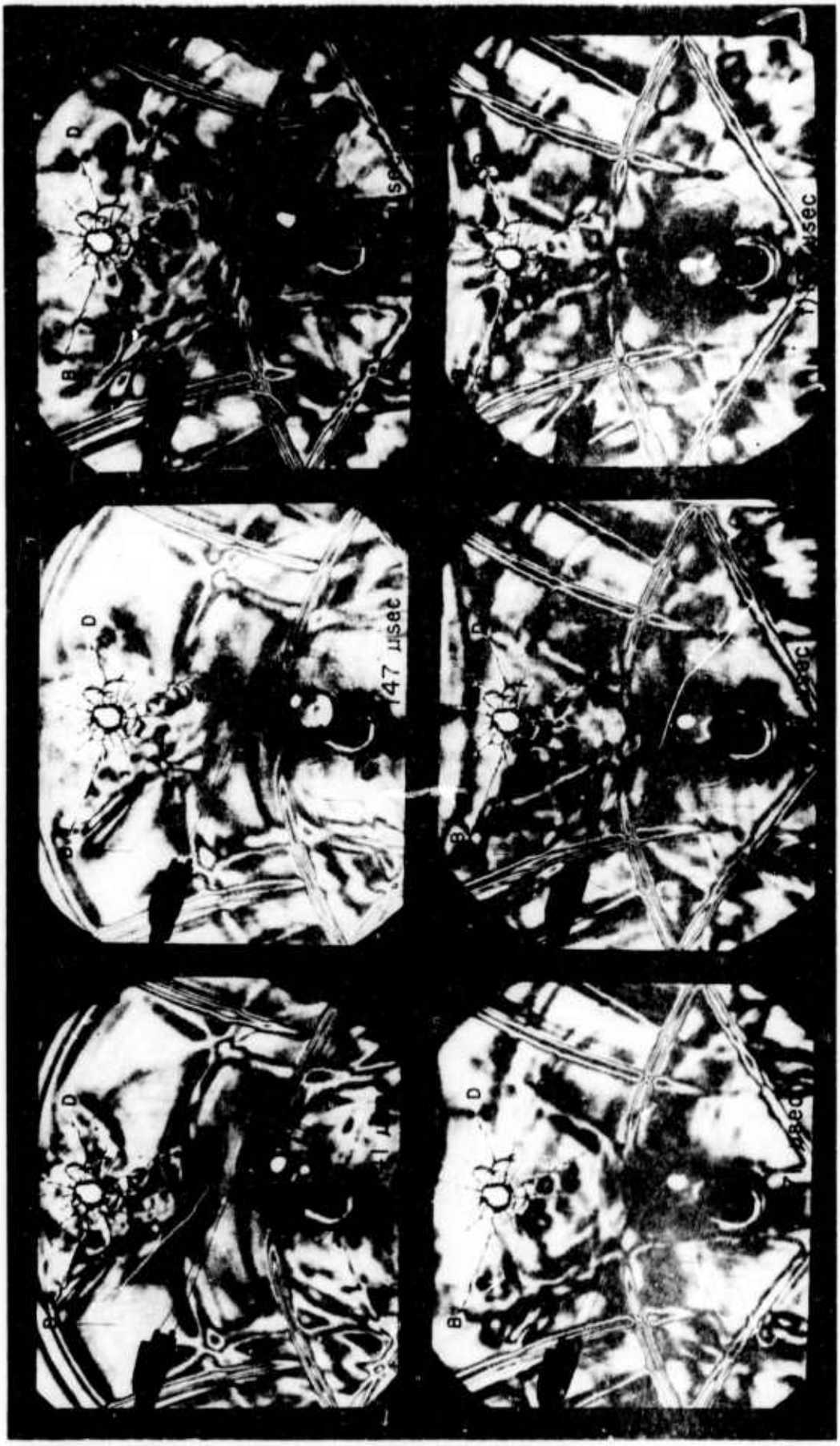

Fig. 6.5 P Wave Interaction With Cracks From Test H-8

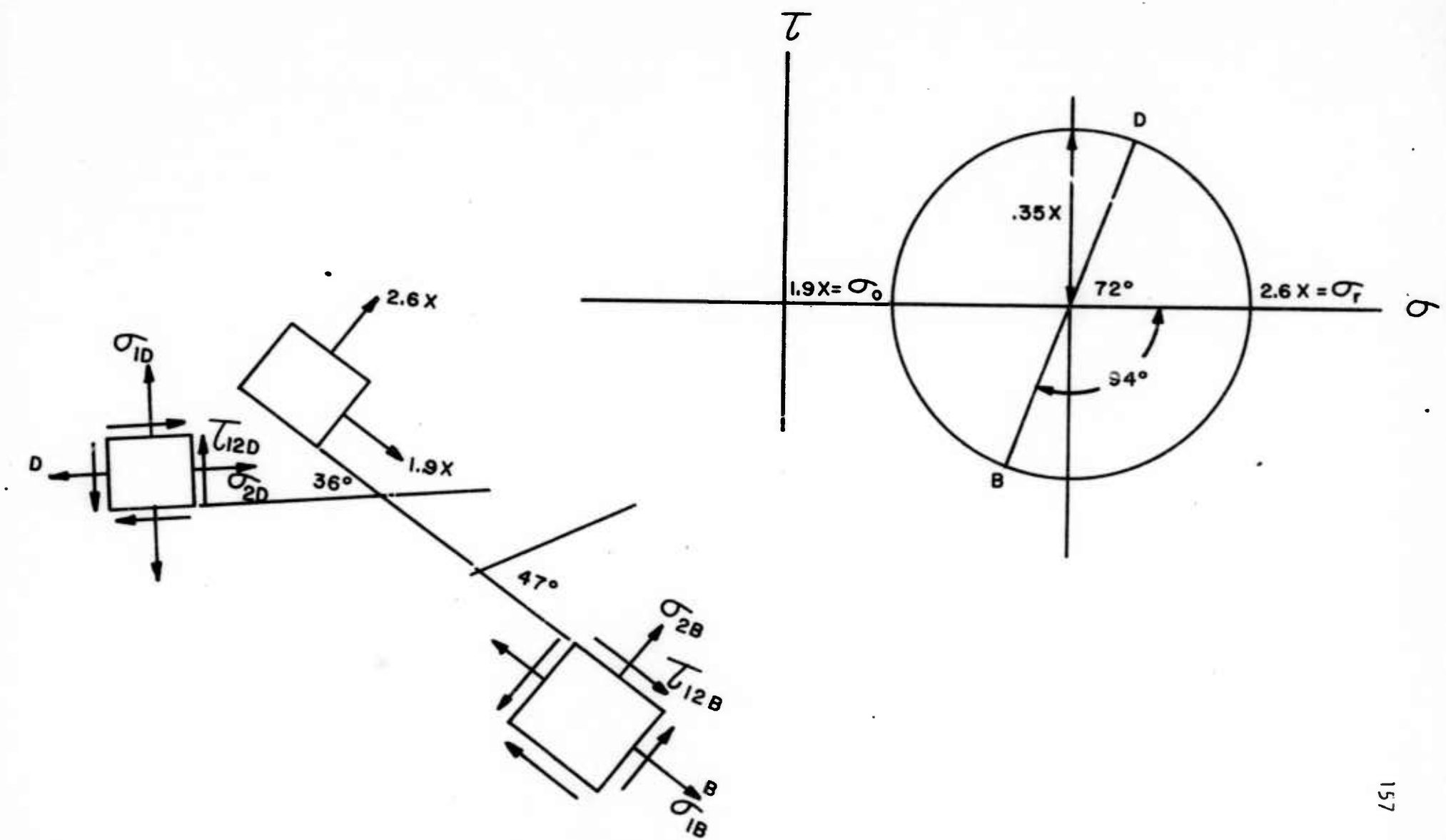

Fig. 6.6 State of Stress Present at Cracks B and D Due to P Wave Tensile Tail

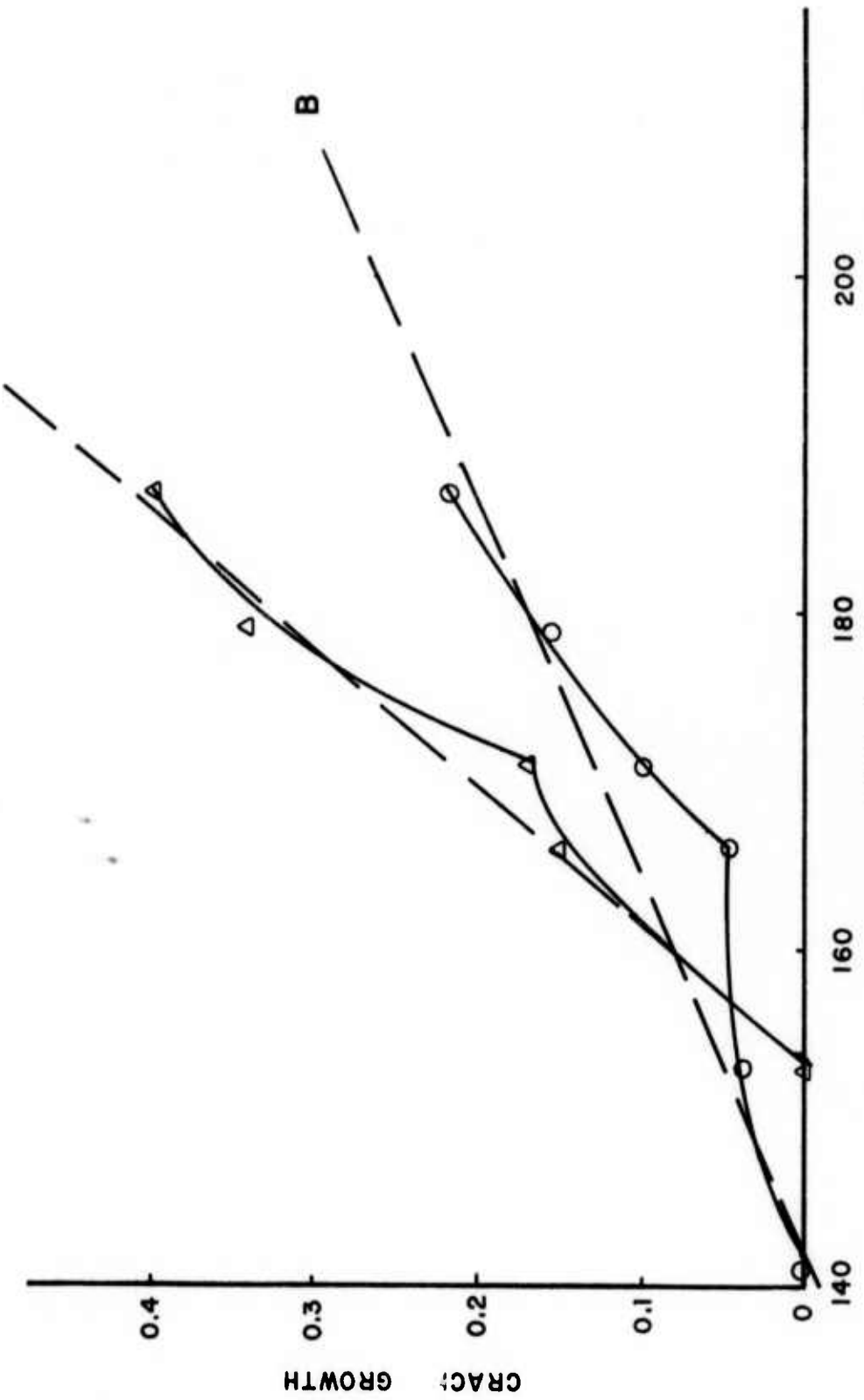

Fig. 6.7 Crack Growth as a Function of Time for Cracks B and D Test H-8

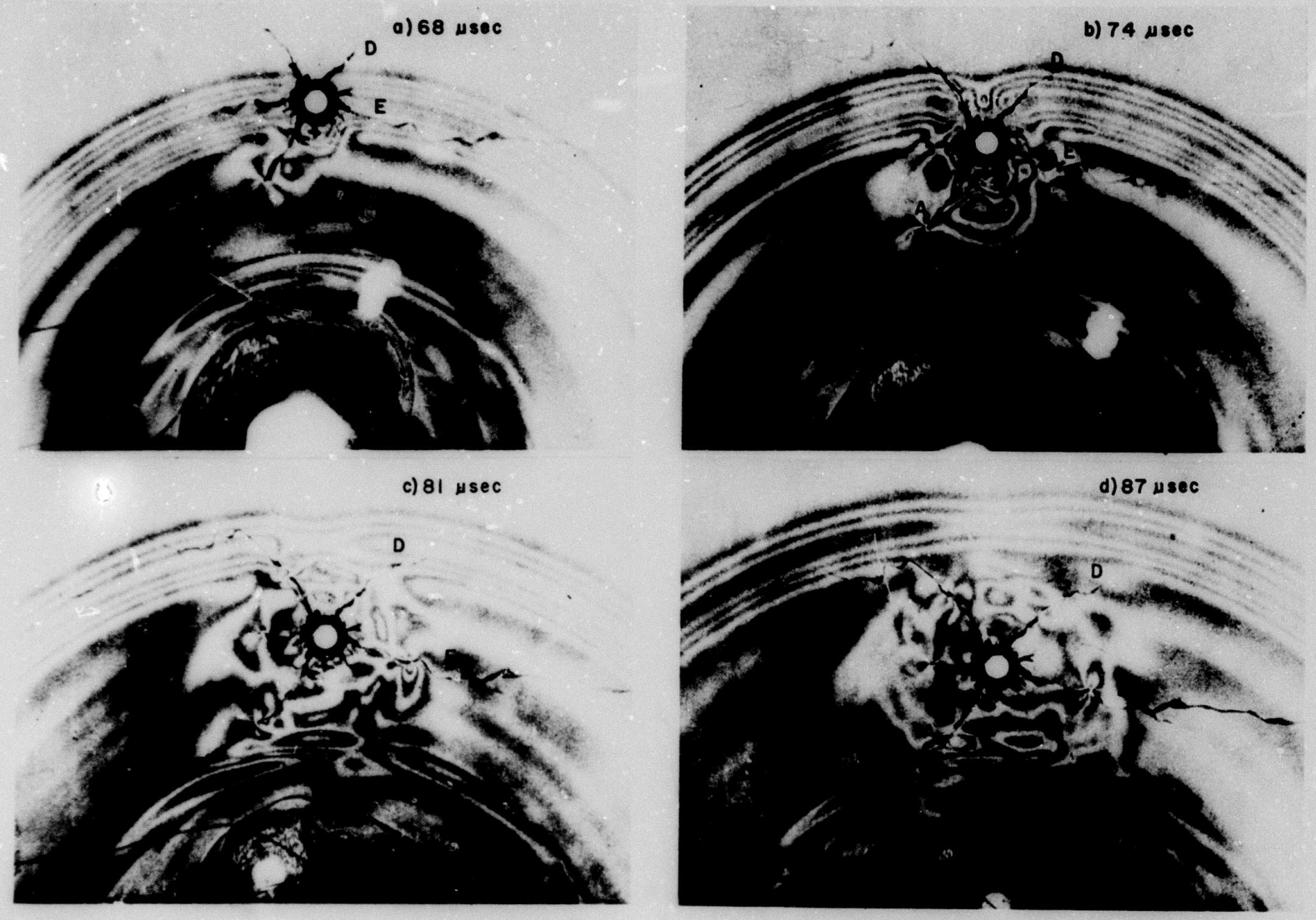

Fig. 6.8 Passage of P Wave Over Cracks A and E From Test H-9

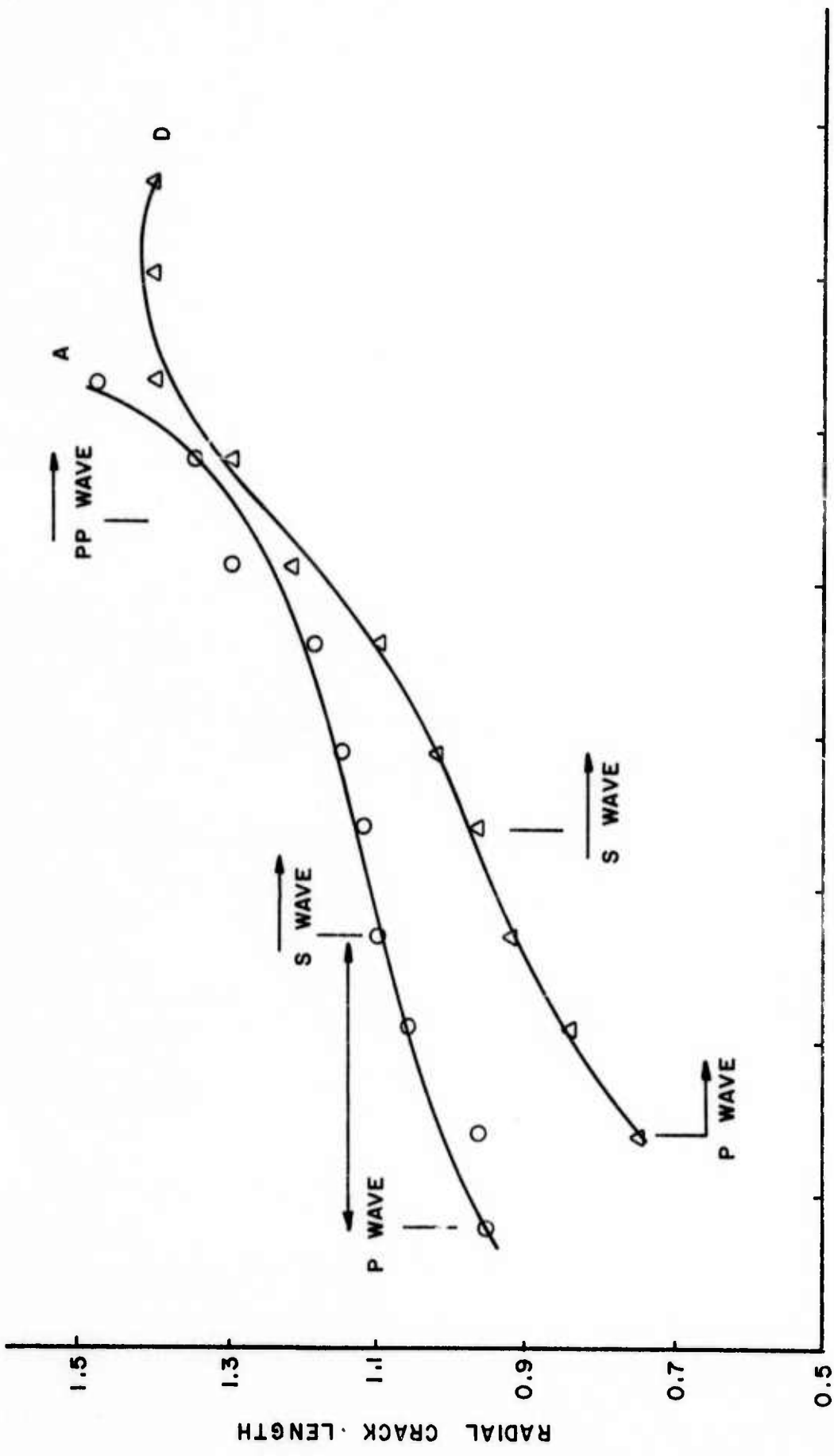

Fig. 6.9 Crack Growth as a Function of Time for Cracks A and E From Test H-9

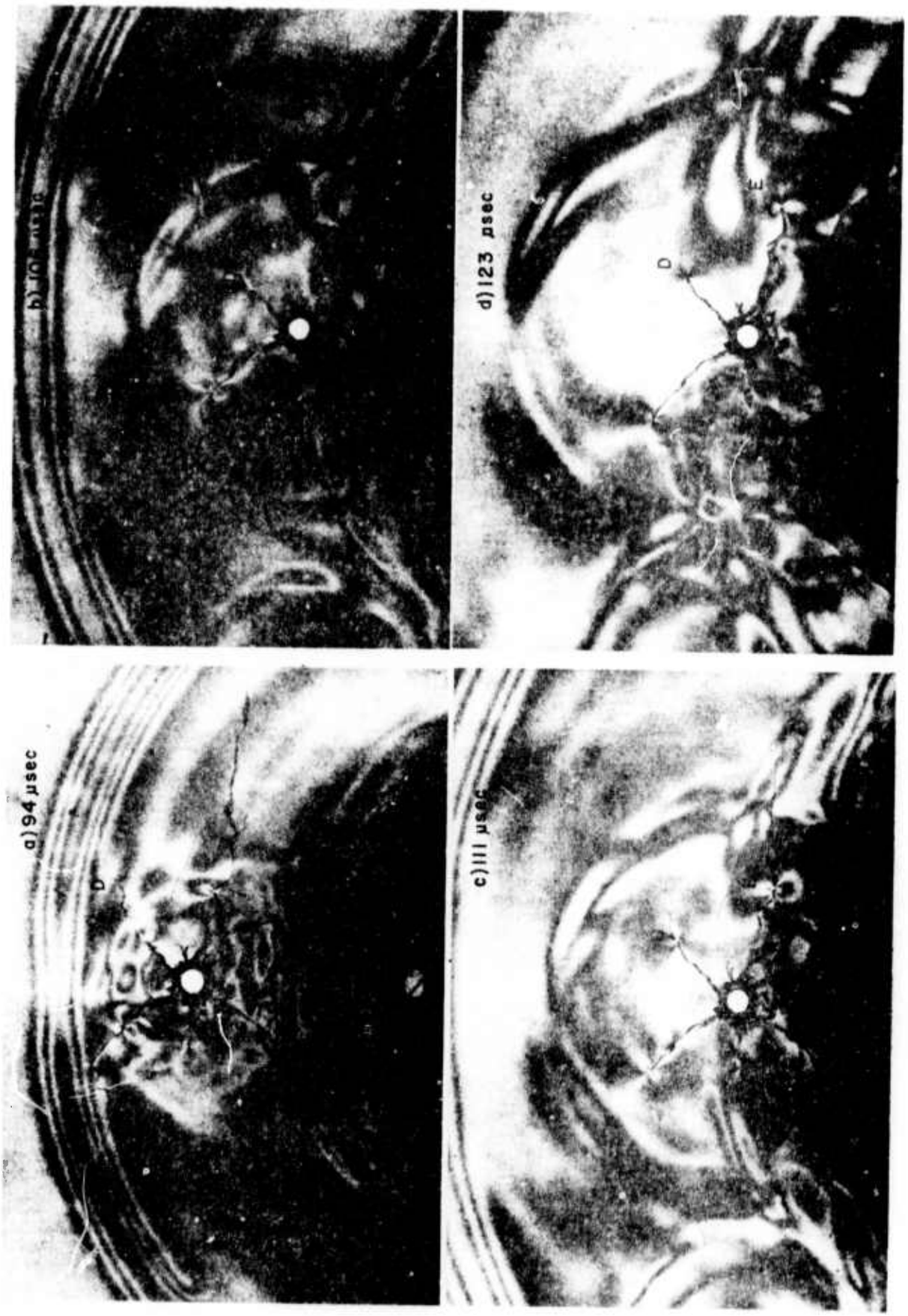

Fig. 6.10 Passage of S Wave Over Cracks A & E From Test H-9

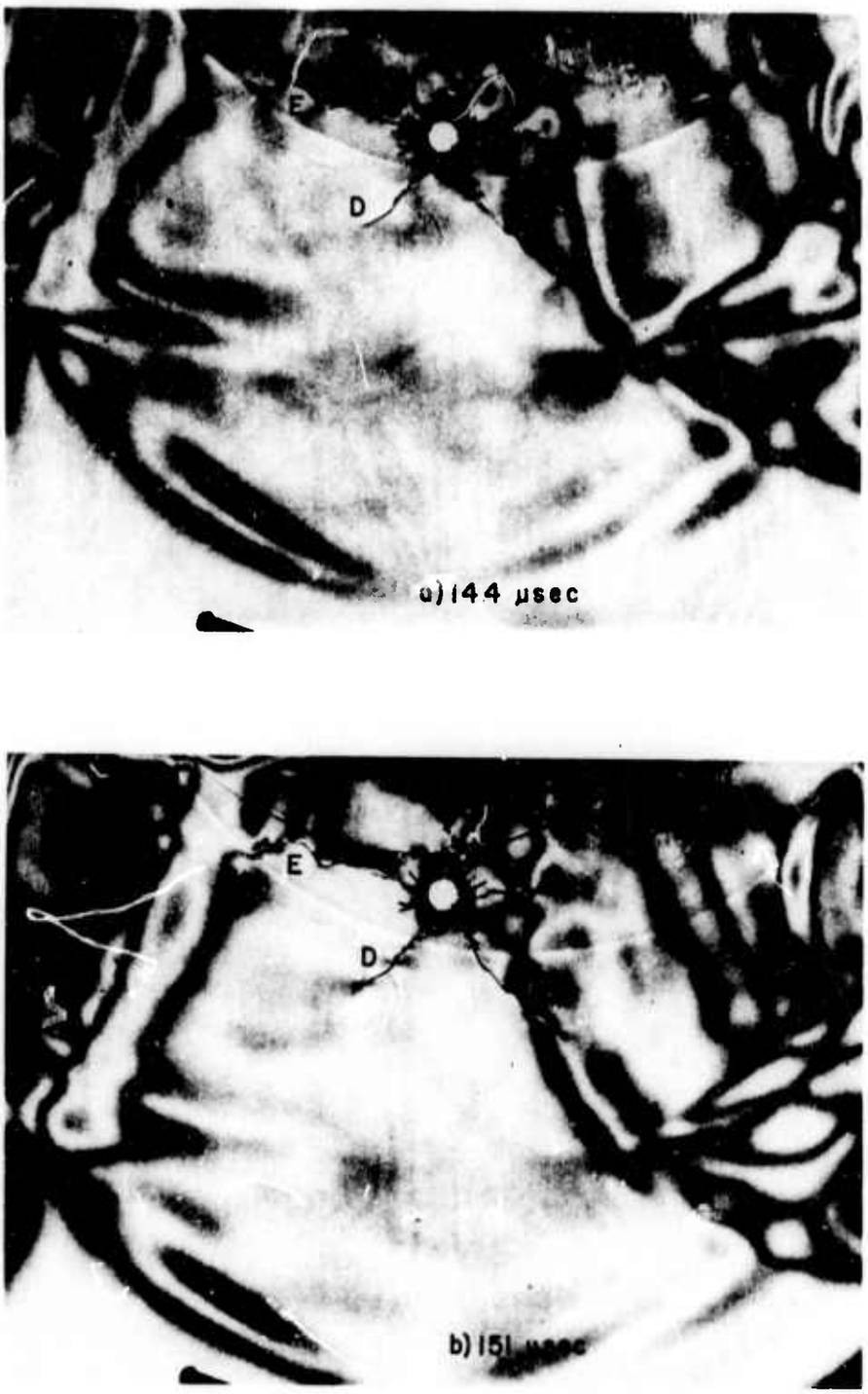

Fig. 6.11 Frames Depicting Passage of Tail of S Waves Over Cracks A and E From Test H-9

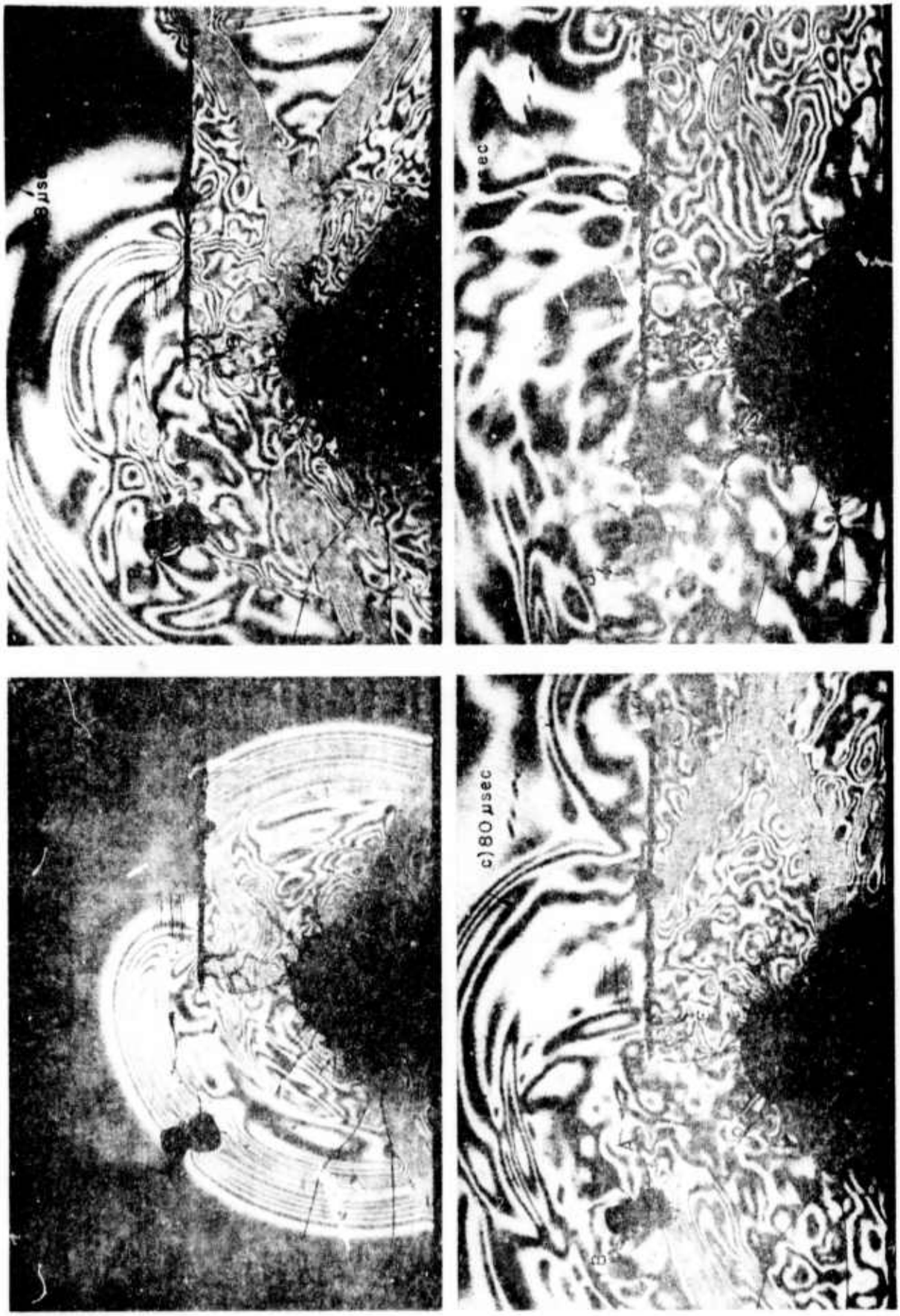

Fig. 6.12 Frames Depicting Stress Wave Crack Interaction 36, 58, 80 and 117 μsec After Detonation for Test H-29

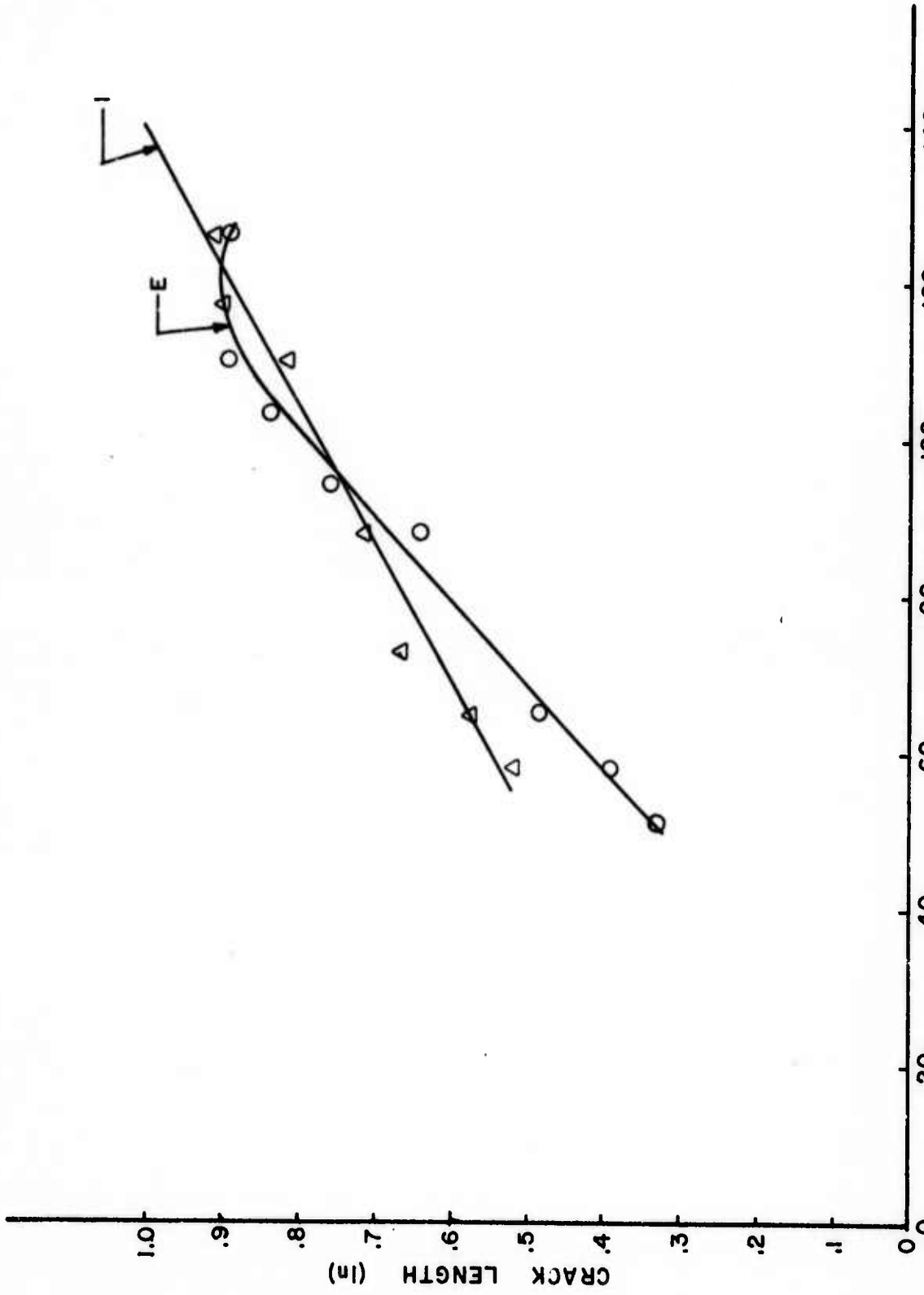

Fig. 6.13 Crack Growth as a Function of Time for Cracks E and I for Test H-29

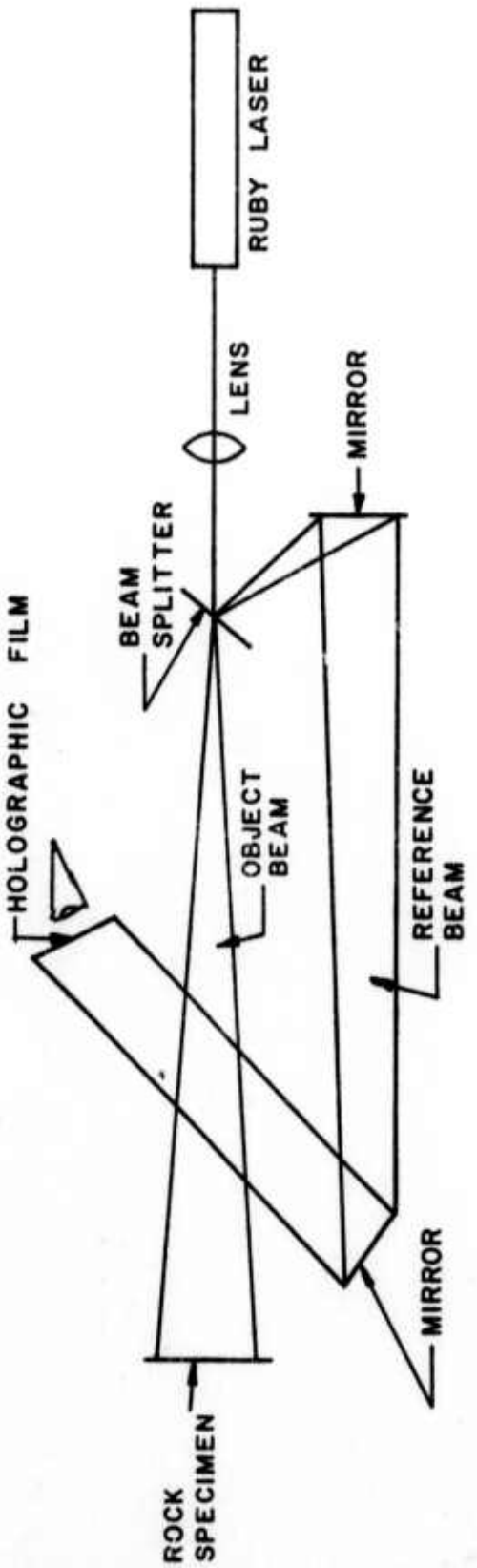

Fig. 7.1 A Holographic Arrangement for Recording Stress Waves in Rocks

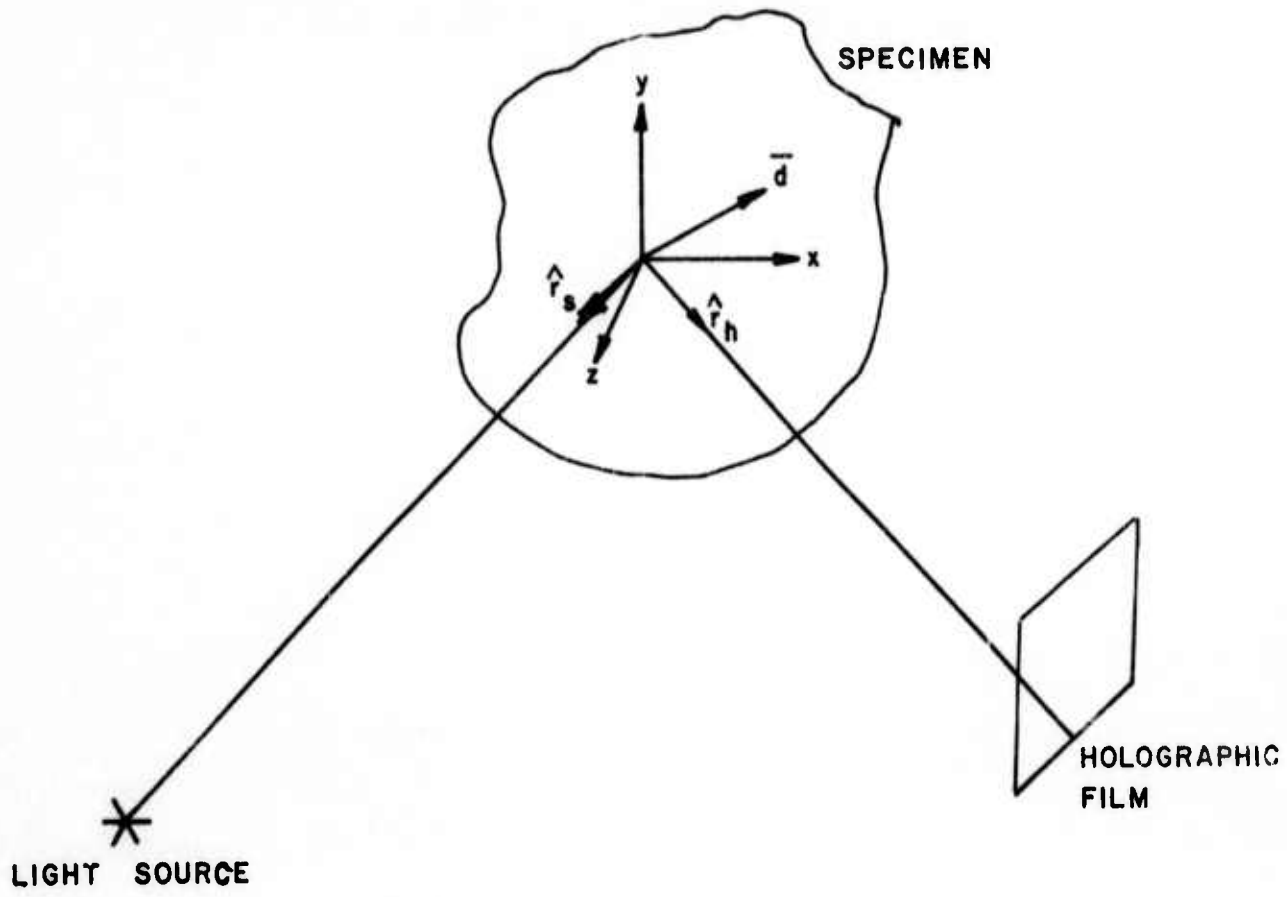

Fig. 7.2 Coordinate Axis and Vector Relationships for Holographic Interferometry

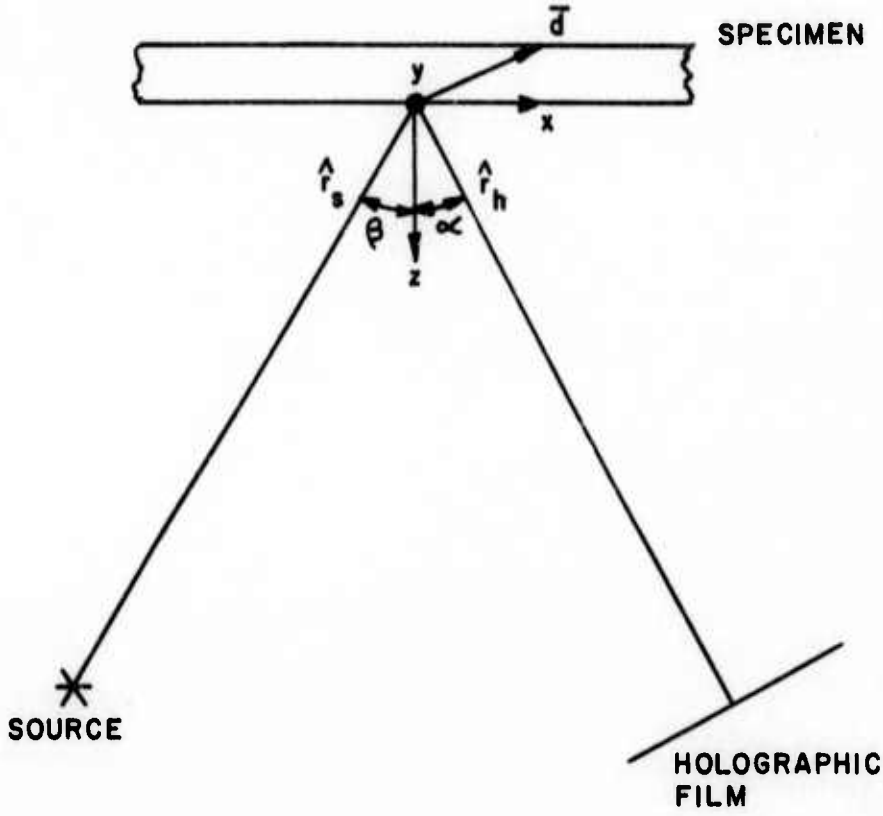

Fig. 7.3 The Condition of Co-planar Object and Viewing Vectors

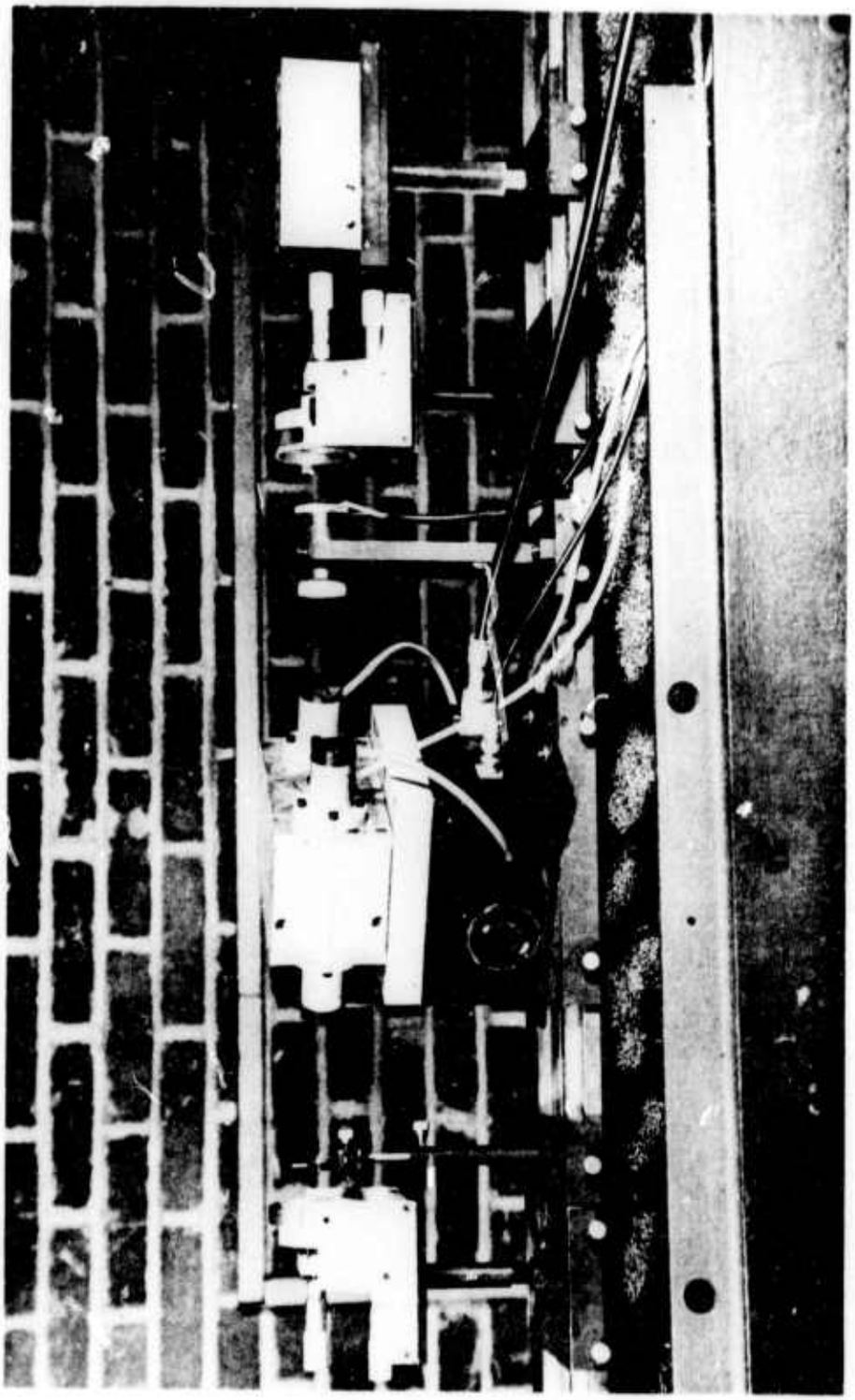

Fig. 7.4 The Pulsed Ruby Laser

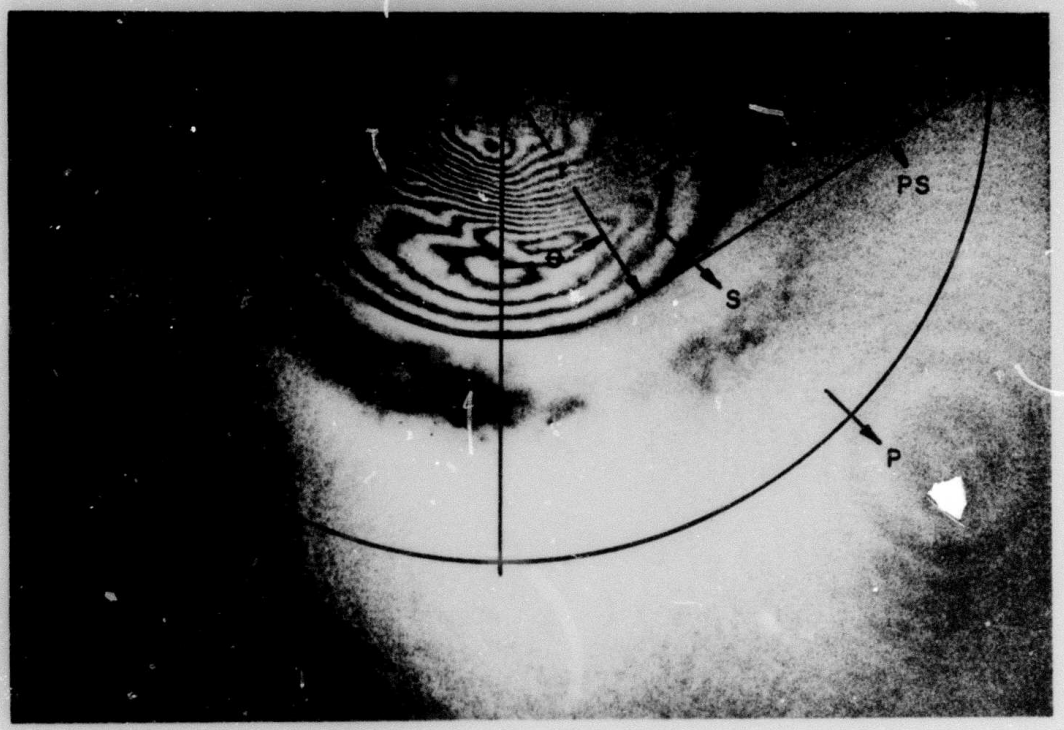

Fig. 7.5 The Holographic Fringe Pattern in Charcoal Granite Taken 24 Microseconds after Explosion

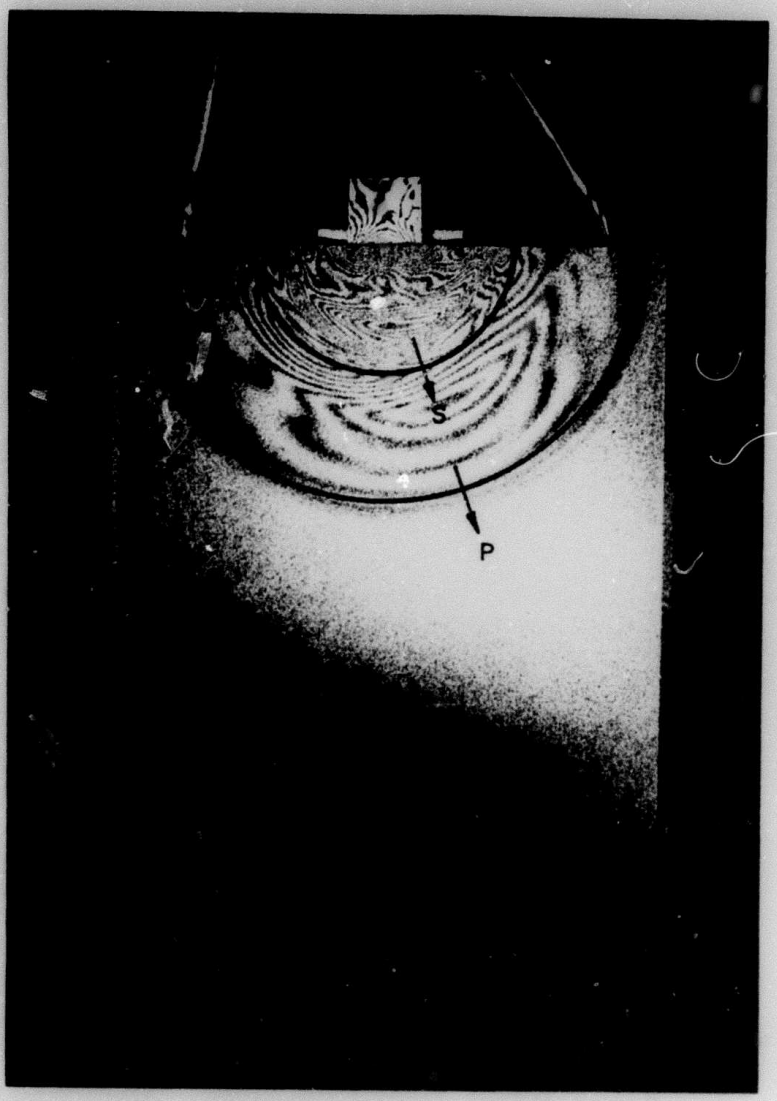

Fig. 7.6 The Holographic Fringe Pattern in Homolite 100 Taken 20 Microseconds After the Explosion

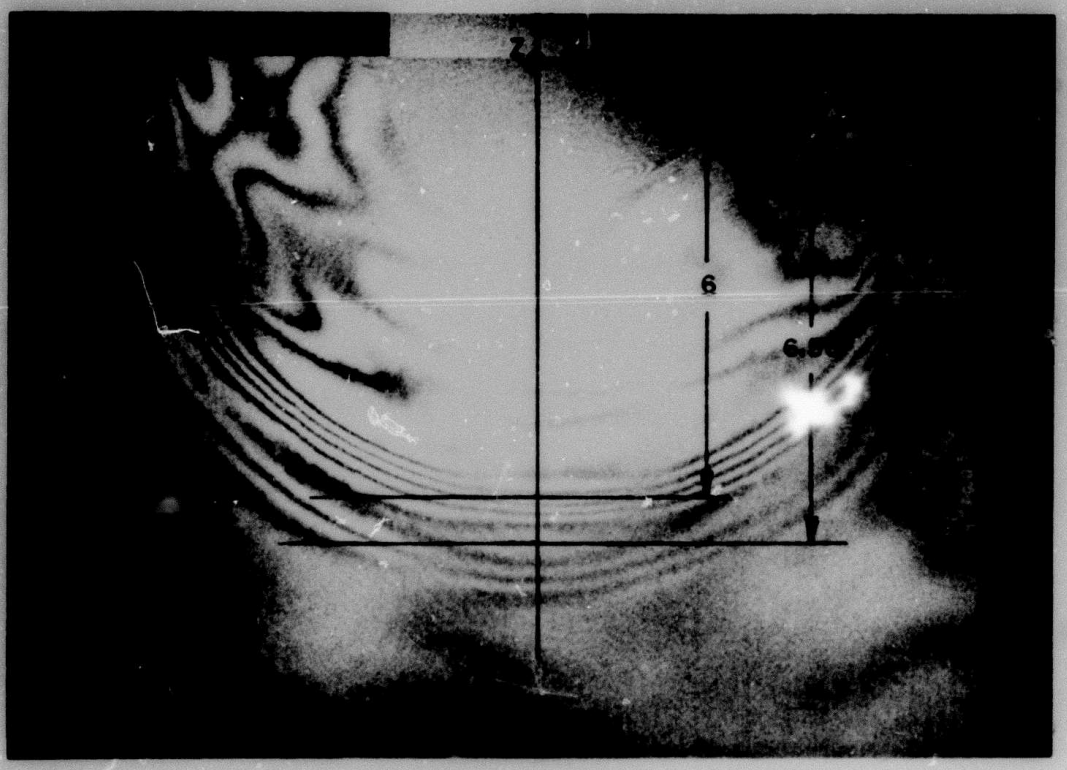

Fig. 7.7 The Holographic Fringe Pattern in Charcoal Granite Taken 60 Microseconds after the Explosion

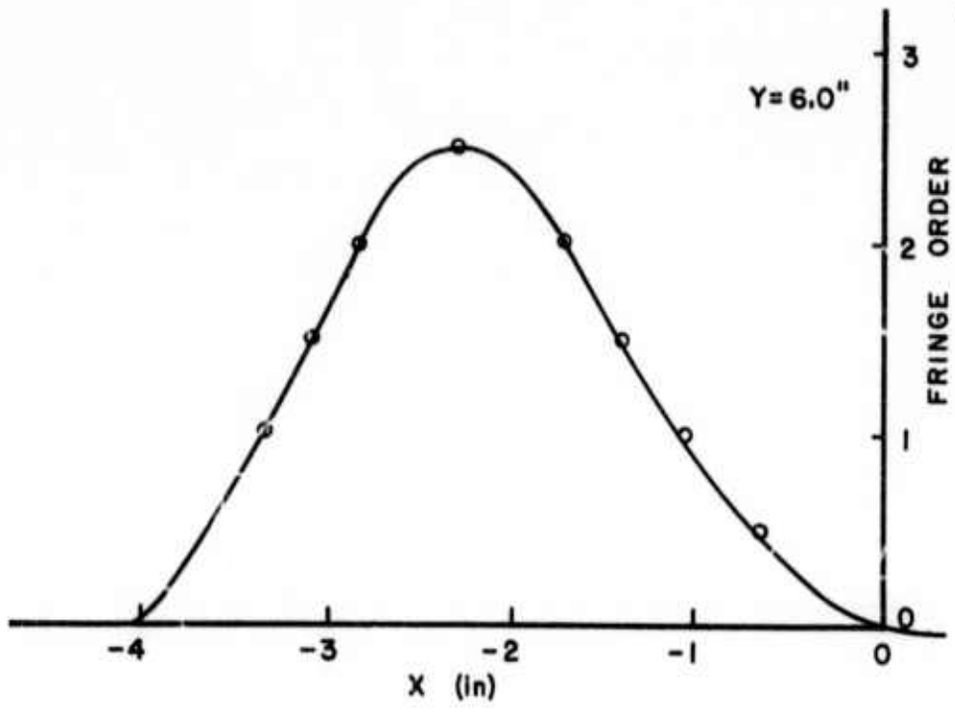

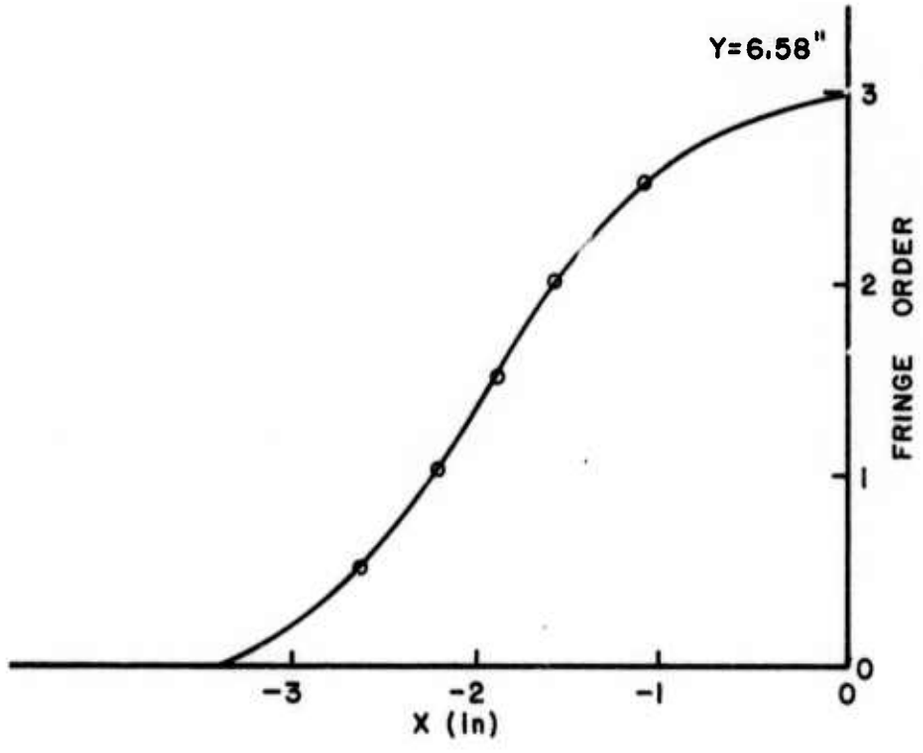

Fig. 7.8 The Holographic Fringe Order N Plotted as a Function of x for a Distance of 6.00" and 6.58" From the Top Surface